

Roger Thoresen

Stability and Control of a Microgrid

Master's thesis in Energy Use and Energy Planning

Supervisor: Kjetil Uhlen

June 2019

Roger Thoresen

Stability and Control of a Microgrid

Master's thesis in Energy Use and Energy Planning
Supervisor: Kjetil Uhlen
June 2019

Norwegian University of Science and Technology
Faculty of Information Technology and Electrical Engineering
Department of Electric Power Engineering

 **NTNU**
Norwegian University of
Science and Technology

Abstract

With a large spread in the settlement of people in Norway, the continuous supply of electrical power can be both challenging and costly for remote areas. In the coming years, the distribution grid faces large reinvestment costs, leading to the consideration of alternative solutions. One of the most promising, and trending, solutions is to establish low voltage microgrids. The combination of various distributed generation and storage solutions implies a need for control and assessment of the microgrid stability.

In this thesis the control and stability of a low voltage microgrid during the transition between grid-connected and islanded operation is in focus. Based on obtained data from a remote area at the west coast of Norway, a microgrid model was developed in the Matlab/Simulink environment. The complete model consists of a 30 kVAr wind turbine, 32 kVAr battery energy storage solution, 30 kVAr photovoltaic system, 15 kVAr diesel generator, variable loads and a connection to the utility grid. The photovoltaic-, wind turbine- and battery energy storage system is connected to the low voltage AC-grid by two-level voltage source converters with individual control systems.

The overall control strategy can be divided into two main categories: Grid-Connected and Islanded operation. In grid-connected operation, the distributed generation units operate with active- and reactive power control, while the grid ensures a stable voltage and frequency. In islanded mode, the battery energy storage system is changed to voltage- and frequency control, hence functioning as a master unit in the system, while the PV- and WT system continues operating under PQ-control. In case of malfunctioning or limited capacity for the storage solution, a diesel generator system with a synchronous generator is implemented to enhance the electrical power supply reliability.

Simulations are performed for both intentional- and unintentional islanding of the microgrid system. For intentional islanding the power exchanged between the microgrid and utility grid is minimized to ensure a seamless transition. With unintentional islanding there is an export or import of power at transition which leads to voltage and frequency deviations. The results suggest that the battery energy storage system can ensure a fast recovery of the nominal frequency and voltage. By implementing a time delay representing the island detection system, the power quality is strongly reduced during the delay. A transition to islanded operation without the battery energy storage system is also presented, where a droop controller utilizing the inertia stored in the rotating mass of the wind turbine is implemented, with positive effects on the frequency deviation. At last, to enhance the electric power supply reliability, the system's feasibility to perform a black start with either the battery energy storage system or diesel generator is verified.

The results show promising performance of the microgrid, though challenging scenarios are present. Results and measures for improvements of the system stability are thoroughly discussed.

Sammendrag

Med en utbredt bosetting av mennesker i Norge kan kontinuerlig forsyning av elektrisk kraft være både utfordrende og kostnadskrevende for de mest avsidesliggende områdene. I de kommende årene er det forventet at distribusjonsnettet står ovenfor store reinvesteringskostnader som medfører at flere ønsker å vurdere alternative løsninger. En av de mest lovende, og omtalte løsningene, er etablering av lavspent mikronett. Med flere ulike distribuerte produksjonsenheter innebærer dette en nødvendighet for kontroll og en vurdering av mikronettets stabilitet.

I denne avhandlingen fokuseres det på kontroll, og vurdering av stabilitet, for et lavspent mikronett i overgangen fra å være tilkoblet overliggende nett til øydrift. Med utgangspunkt i informasjon fra et avsidesliggende område ved vestkysten i Norge, er en modell av mikronettet etablert i Matlab/Simulink. Modellen inkluderer en 30 kVAr vindturbin, et 32 kVAr batterilagringsystem, 30 kVAr solcelleanlegg, 15 kVAr dieselaggregat, laster og tilkobling til overliggende distribusjonsnettet. Solcelleanlegget, batterilagringsystemet og vindturbinen er tilkoblet det lavspente AC-nettet via omformere med individuelle kontrollsystemer.

Den overordnede kontrollstrategien er delt i to hovedkategorier: tilkoblet og frakoblet det overliggende nettet. Når mikronettet er tilkoblet det overliggende nettet opererer de distribuerte produksjonsenheterne og lagringssystemet i PQ-kontroll, mens det overliggende nettet sørger for stabil frekvens og spenning. I øydrift veksler batterilagringsystemet fra PQ-kontroll til spenning og frekvenskontroll, og fungerer dermed som en masterkontroll i mikronettet. Ved funksjonsfeil eller manglende kapasitet i lagringssystemet sørger diesel aggregatet for å øke leveringspåliteligheten.

Simuleringer er gjennomført for både planlagt og ikke-planlagt frakopling av overliggende nett. Ved planlagt frakopling er utvekslingen av effekt mellom mikronettet og overliggende nett minimert for å sørge for en sømløs overgang. Ved en ikke-planlagt frakopling vil det være import eller eksport av kraft ved overgangen til øydrift som kan føre til avvik fra nominell spenning og frekvens. Resultatene antyder at batterilagringsystemet kan sørge for en rask gjenopprettelse av nominell frekvens og spenning. Dersom en tidsforsinkelse implementeres for å representere detektering av øydrift, vil dette påvirke leveringskvaliteten betraktelig. En overgang til øydrift uten batterilagringsystemet er også vurdert. I dette scenarioet er en droop-kontroll som utnytter treghetsmomentet lagret i vindturbinens roterende masse implementert med positive resultater for leveringskvaliteten. For å øke leveringspåliteligheten er også systemets mulighet til å gjennomføre en såkalt «black start» med batterilagringsystemet eller dieselaggregatet verifisert.

Resultatene viser at mikronettet kan operere velfungerende, men at det også finnes krevende situasjoner for overgangen mellom å være tilkoblet overliggende nett og øydrift. Både resultatene, og tiltak for forbedring av systemets stabilitet og kontroll er diskutert.

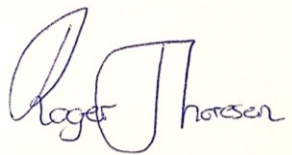
Preface

This thesis concludes the final semester as a M.Sc. student at the Department of Electric Power Engineering at the Norwegian University of Science and Technology. I am grateful for the opportunity to conduct the degree at NTNU and proud of the accomplishments I have achieved.

A gratitude is given to my supervisor, Professor Kjetil Uhlen for providing his competence and ideas through this semester. Further, I would like to thank my co-supervisors, Sindre Solberg and Vebjørn Haukaas at Siemens PTI for your warm welcoming and support with this thesis. A gratitude is also in order for Bendik Fossen at Sunnfjord Energi Nett for providing the necessary data and enthusiasm for the microgrid project.

Finally, my sincerest gratitude goes to my partner, family and friends for their support and motivation. Without them, this degree would not have been possible.

Trondheim, 01.06.2019

A handwritten signature in blue ink on a light yellow background. The signature reads "Roger Thoresen" in a cursive style.

Roger Thoresen

Table of Contents

1	Introduction.....	1
1.1	Background and Motivation	1
1.2	Objective	2
1.3	Scope of Work	2
1.4	Thesis Outline.....	2
2	The Proposed Microgrid	4
2.1	Description of the Microgrid.....	4
2.2	Microgrid Site Conditions	5
2.3	Economics and Suggested Component Ratings	7
3	Microgrid Control and Modelling.....	9
3.1	System Description	9
3.2	Control Strategy	10
3.3	Voltage Sourced Converters	12
3.4	Existing Grid.....	16
3.5	Photovoltaic system	18
3.6	Battery Energy Storage System	23
3.7	Wind Turbine System	29
3.8	Diesel Generator System	41
4	Validation of Subsystem Models	46
4.1	Existing Grid.....	46
4.2	PV System	47
4.3	Battery Energy Storage System	50
4.4	Wind Turbine.....	54
4.5	Diesel Generator	59
5	Cases and Results	62
5.1	Case Study Introduction	62
5.2	Transient Response to Islanding	62

5.3	Black Start Capability	74
6	Discussion	82
6.1	General	82
6.2	Intentional Islanding	83
6.3	Unintentional Islanding	84
6.4	Black Start Capability	86
7	Conclusion	89
8	Further Work	91
9	Bibliografi	92
10	Appendices	101
A.	System Parameters	102
B.	Load Distribution for Scenarios	112
C.	Per Unit Systems	114
D.	The Park Transformation	119
E.	Tuning Techniques	120
F.	Tuning of Microgrid Controllers	122
G.	Simulink Model	140

Abbreviations

AC	Alternating Current
BESS	Battery Energy Storage System
DC	Direct Current
DG	Distributed Generation
DGR	Diesel Generator
DSO	Distribution System Operator
dq	Two-Axis dq-Reference Frame
GSC	Grid Side Converter
IGBT	Insulated Gate Bipolar Transistor
KCL	Kirchhoff's Current Law
MMF	Magnetomotive Force
MPPT	Maximum Power Point Tracker
MSC	Machine Side Converter
PCC	Point of Common Coupling
PLL	Phase Locked Loop
PQ	Active- and Reactive Power Control
PQ-Code	Power Quality Code
pu	Per Unit
PV	Photovoltaic
PWM	Pulse Width Modulation
SOC	State of Charge
TSR	Tip Speed Ratio

THD	Total Harmonic Distortion
V/f	Voltage- and Frequency Control
VSC	Voltage Sourced Converter
WT	Wind Turbine

1 Introduction

1.1 Background and Motivation

Ever since the first electric production was established in 1877, the Norwegian objective to expand and connect the population has been a priority. Already before the second world war around 80 % of the Norwegian population was had access to electric energy [1]. Today, remote areas and islands across the widespread country is connected to the electricity grid. The energy consumption on these places are often low and the connection constitutes of long radials of overhead lines and cables, resulting in high cost for operation and maintenance for the grid owner.

Many of the remote areas connected to the grid today needs an upgrade or replacement of the current connection. For the grid companies, and hence the customers, the reinvestment costs are high compared to the consumption. This provides an incentive for alternative solutions. One of the alternative solutions is to implement a microgrid with local production and storage. Introducing local production, such as wind and solar, in combination with storage solutions, such as batteries and hydrogen, could increase the self-consumption and reduce the dependency of the connection to the distribution grid. Or even remove the need of a connection at all.

By including a diesel or gas generator the technical possibilities of a microgrid, even operating isolated from the distribution grid, is possible. The challenge arises as the objective to have a certain renewable share is included. With the Paris Agreement, the target is a 40 % reduction in greenhouse gas emissions from 1990-2030 [2]. The Norwegian government has expressed their full commitment to comply to these targets [2], which implies that a strict focus on low emission resources must be considered for any technical solution.

An initiative actuated by the Norwegian energy company Sunnfjord Energi, in cooperation with Siemens PTI, aims to facilitate a microgrid solution in their concession area. This provides a possibility to consider an actual case area with grid- and consumer data. Furthermore, it implies that the solution must provide an acceptable customer reliability and follow the present jurisdictions of the area.

The microgrid system, consisting of a large share of fluctuating renewable production must provide feasible results, both from a technical and economical viewpoint. Preliminary studies on the economic and technical possibilities in long term has been evaluated in [3]. Despite that the economic results of [3] suggests that substantial alternative costs are required, the price of renewable production units and storage is decreasing, and hence the possibilities of realization increasing.

1.2 Objective

The main objective of this thesis is to further study the technical aspects of a microgrid system harvesting energy from the wind and sun, integrated with a storage solution. Considering the preliminary work in [3], the aim is to further develop a comprehensive model suitable for analysis of transient events and the impact on power quality, with a focus on the transition from grid-connected operation to islanded operation. The model is to be developed and analyzed in the Matlab/Simulink® environment.

1.3 Scope of Work

The scope of work in this thesis is limited to providing a dynamic model and control of the components included in the microgrid. With the developed Simulink model, a series of scenarios are performed and analyzed with respect to power quality. A special focus is set on the transition between grid-connected and islanded operation.

Throughout the thesis the aim has been to outline the assumptions and limitations as they are encountered, with the most central being:

- Wiring from the production- and storage solutions are not implemented. Thus, the units are directly coupled to the point of common coupling (PCC).
- An overall control strategy is presented, but the strategy has not been fully implemented to operate autonomously in the model due to time restrictions.
- To limit the scope of work, economic analysis is omitted. Preliminary economic analysis in [3], are briefly revisited.

Further assumptions and limitations are discussed in 6, *Discussion*, while suggestions to improve and inspire for further work is presented in 8, *Further Work*.

1.4 Thesis Outline

Throughout the thesis the aim is to present the content in a structured way to provide a clear understanding of the work without repeating fundamental theory in detail. The start of the thesis picks up the thread from the specialization project, before the individual components and control of the microgrid is presented. This leads to a complete microgrid used for simulation of cases.

Chapter 2 – *The Proposed Microgrid* – introduces the proposed area for establishment of a microgrid, and a brief consideration of the obtained information and results from the specialization project.

Chapter 3 – *Microgrid Control and Modelling* – presents the overall control strategy and a mathematical representation of the system components and control.

Chapter 4 – *Model Validation* – validates the operation of the modelled components and control systems, individually.

Chapter 5 – *Cases and Results* – introduces and presents the main findings from the case studies. Scenarios includes intentional- and unintentional islanding, and black start capability.

Chapter 6 – *Discussion* – discusses the findings from the results, where the validity of the results and suggestions for improvements are highlighted.

Chapter 7 – *Conclusion* – summarizes the main findings of the thesis.

Chapter 8 – *Further Work* – proposes the possibilities for further work with control and stability of microgrids and presents the main shortcomings.

2 The Proposed Microgrid

In this chapter, the proposed microgrid along with the properties of the area is presented. The chapter also includes a summarized section of recommendations based on long term economic considerations from the work performed in the specialization project.

2.1 Description of the Microgrid

The proposed microgrid area is located on the island Sula, in Sogn and Fjordane county. Today, the area is located at the end of a radial connected to the distribution grid. But in a rough environment, the delivery of continuously electricity according to the Norwegian PQ-code can be challenging and costly [3]. In this thesis the low voltage grid is considered to remain as is, with the *point of common coupling* (PCC) located at the busbar shown in Figure 2.1, with the six connected customers. These are defined as *House 1-3* and *Cabin 1-3* to anonymize sensitive customer data¹.

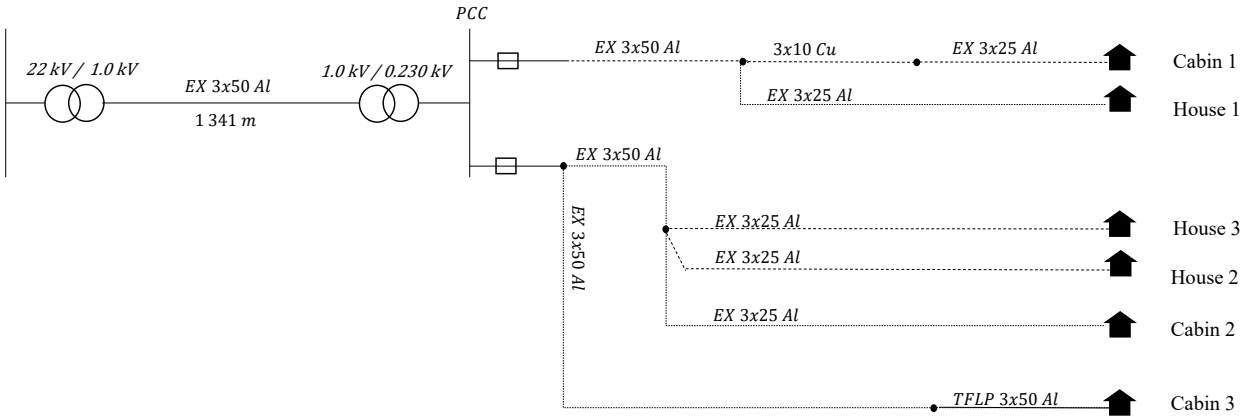


Figure 2.1. Overview of Existing Grid

Through long term calculations performed in the project thesis, and through discussions with Sunnfjord Energy, this thesis considers a microgrid with a wind turbine (WT), a photovoltaic (PV) system, a battery energy storage system (BESS) and a diesel generator (DGR).

¹ Anonymized in accordance to information provided by Sunnfjord Energi Nett AS

2.2 Microgrid Site Conditions

The microgrid site conditions are considered with three main aspects, namely the wind speed, solar irradiance and the load consumption. These has been assessed extensively in [3], with main findings restated in this section.

2.2.1 Load Consumption

The load consumption for the proposed area was obtained through measurements from the newly established *Avanserte Måle- og Styresystemer* (AMS). The measurements were obtained after the AMS had been operative for approximately one year. These were hourly measurements for each of the six customers in the microgrid. To account for yearly variations and future load development, the obtained measurements were increased by 25 % [3]. The total system demand through one year is provided in Figure 2.2. However, these are based upon hourly measurements, which implies that the maximum instantaneous power consumed is somewhat higher.

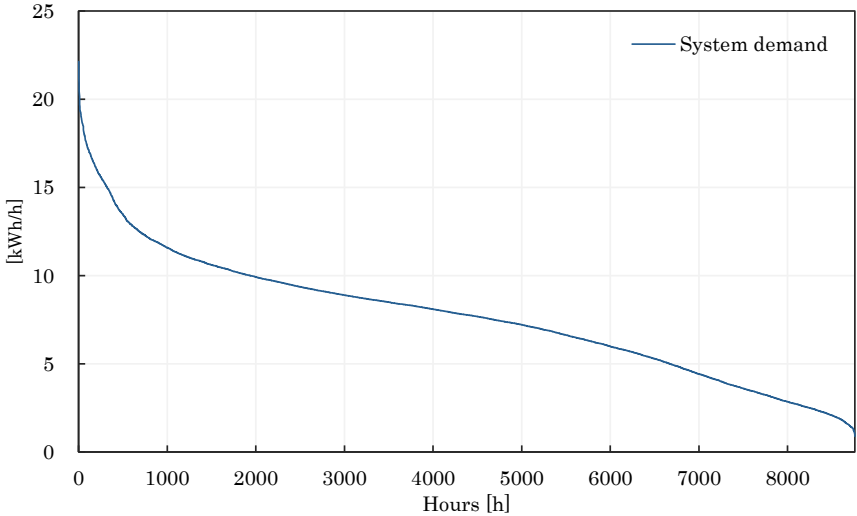


Figure 2.2. System Demand for Proposed Microgrid [3]

2.2.2 Wind Speed

The wind speed assessed in [3] was based on 10-minute interval measurements and estimated wind speed from the PVGIS database. For the long-term energy calculations this was considered sufficient. However, the measurements did not include wind gusts that could cause large power variations, thus challenging the microgrids stability. The obtained probability density function from both measurements and estimated data by PVGIS, see

Figure 2.3, showed a close correlation with the Rayleigh probability density function that is often used as a basis for evaluating good wind sites [3]. Average wind speed was found to be around 7.2 m/s [3].

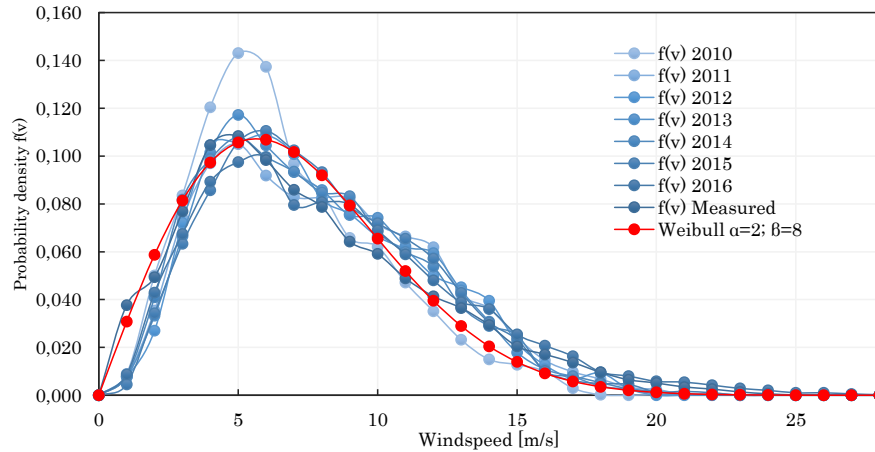


Figure 2.3. Probability Density Functions for Windspeed at Proposed Microgrid [3]

2.2.3 Solar Irradiance

The solar irradiance was the only parameter that was solely based on estimated data. Where both the wind speed and load consumption could be evaluated against measured data, the solar irradiance was based on interpreted satellite data [3]. The average solar irradiance throughout one year was calculated to be around 100 W/m², and a maximum solar irradiance around 1 300 W/m² [3]. The importance of considering the azimuth- and tilt angle for the PV modules were also pointed out, as seen from Figure 2.4.

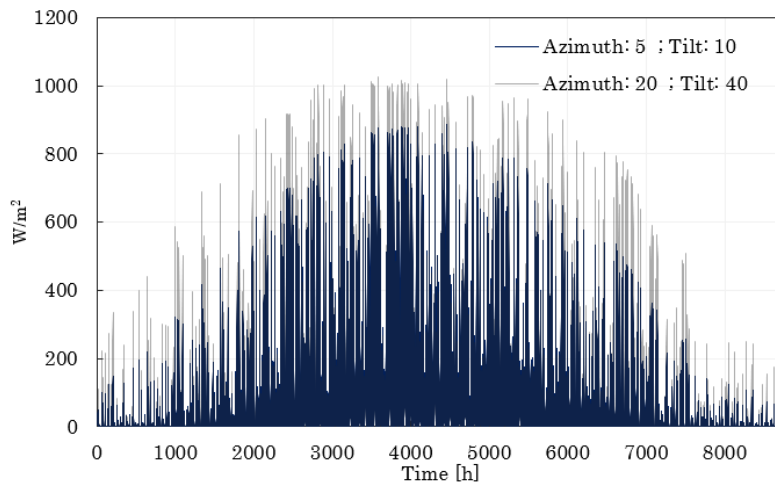


Figure 2.4. Effect on Azimuth- and Tilt Angle for Solar Irradiance [3]

2.3 Economics and Suggested Component Ratings

In [3], both the technical and economic feasibility was controlled and optimized based on hourly data. The objective was to reduce costs and provide a renewable share² above 90 %. A series of simulations considering both the *Levelized Cost of Electricity* (LCoE) and the renewable share led to various configurations that satisfied the requirement. Figure 2.5 shows how the LCoE was expected to increase with increasing renewable share. Thus, the favorable microgrid configuration was a tradeoff between cost and renewable production.

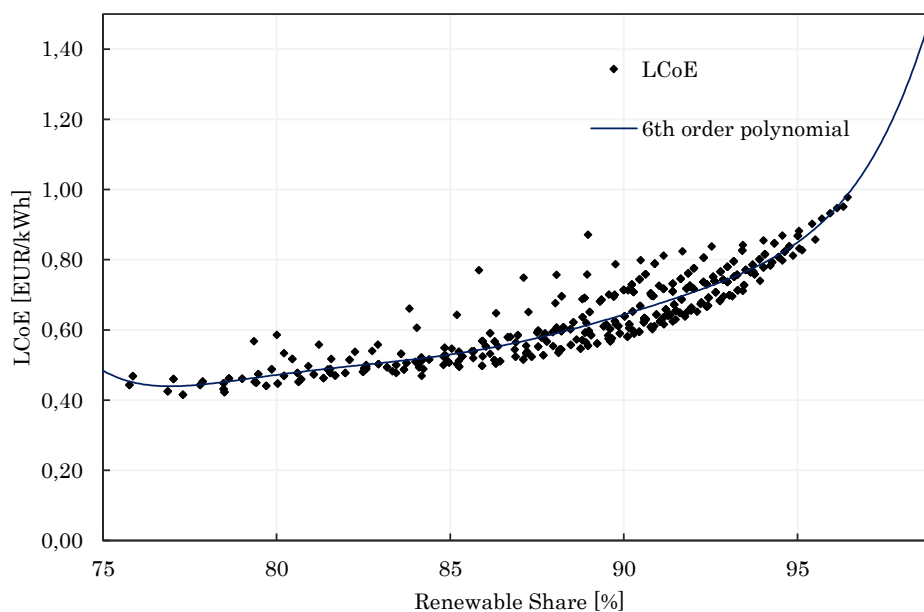


Figure 2.5. LCoE as a Function of the Renewable Share [3]

The suggested microgrid configuration consisted of a 30 kW PV-system, two 25 kW wind turbines and a 77 kWh battery energy storage system in combination with diesel generators [3]. The BESS power rating was assumed to manage the highest expected load of approximately 30 kW. With the proposed microgrid configuration a 20-year analysis resulted in a LCoE of 0.652 EUR/kWh, with a cost distribution as shown in Figure 2.6. Even though the economical results led to the presented configuration, the technical results provided some drawback with the configuration. One of these was the low capacity factors of the WT and PV system because of extensively use of power shedding to remain stable [3]. In addition, the analysis was performed for an islanded microgrid solely. Therefore, these results are only used as a guideline for further studies in this thesis.

² The share of energy produced by renewable resources

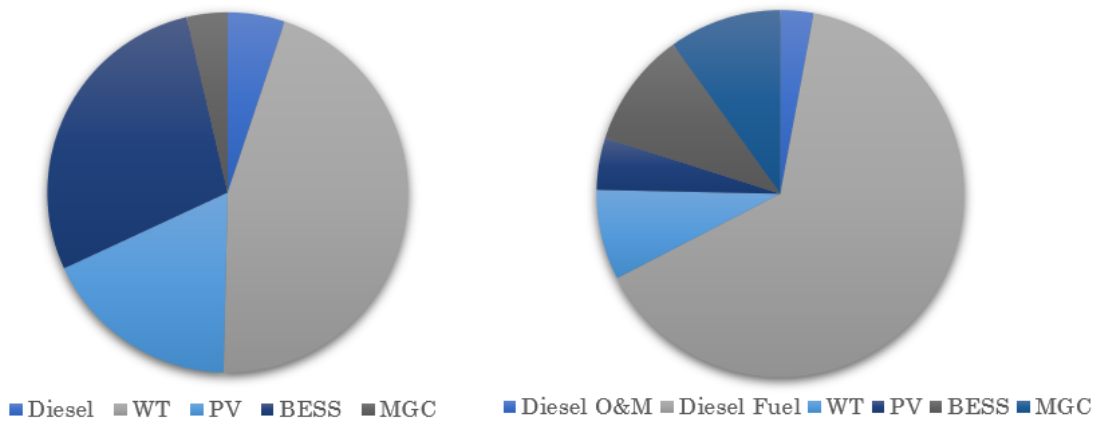


Figure 2.6. Cost Distribution for Suggested Microgrid in [3]. Capital Cost to the Left and Operation and Maintenance Cost to the Right (MGC = Microgrid Controller)

3 Microgrid Control and Modelling

This chapter presents the principles of control, mathematical representation of the system components and implemented control systems. This creates the foundation of the modelled microgrid.

3.1 System Description

The previous work briefly presented in chapter 2 “The Proposed Microgrid” gives guidelines for the modelled system in this thesis. The main objective is to present generic system components which can be altered according to the microgrid specification, rather than creating a replica model of the components used in [3]. Restricted information from manufacturers also restricts the possibility of replicating the full dynamic properties of the system components. Therefore, the mathematical representations and parameters presented are mainly based on methods given in literature.

Figure 3.1 present a schematic overview of the microgrid system with the modelled components and main control properties. This includes a photovoltaic system, a wind turbine, a diesel generator and a battery energy storage system. The PV and BESS are electronically coupled to the AC-grid through a *Voltage Source Converter (VSC)* while the WT system is connected through a back-to-back converter consisting of two VSCs. By using calculations given in [3] as a guideline, the following power ratings are utilized in this model:

- WT: 30 kVAr
- BESS: 32 kVAr
- PV: 30 kVAr
- DGR: 15 kVAr

With the amount of different power sources this creates an operating complexity that must be solved to provide a stable and robust system performance. To achieve an acceptable system performance for a microgrid there are mainly two different situations to consider, namely if the microgrid is operating as grid-connected or disconnected from the grid. In this thesis both operations and the transition from one operation to another is assessed. Detailed system parameters are provided appendix A.

The microgrid control system is developed in the dq-reference frame, utilizing the Park Transformation presented in appendix D.

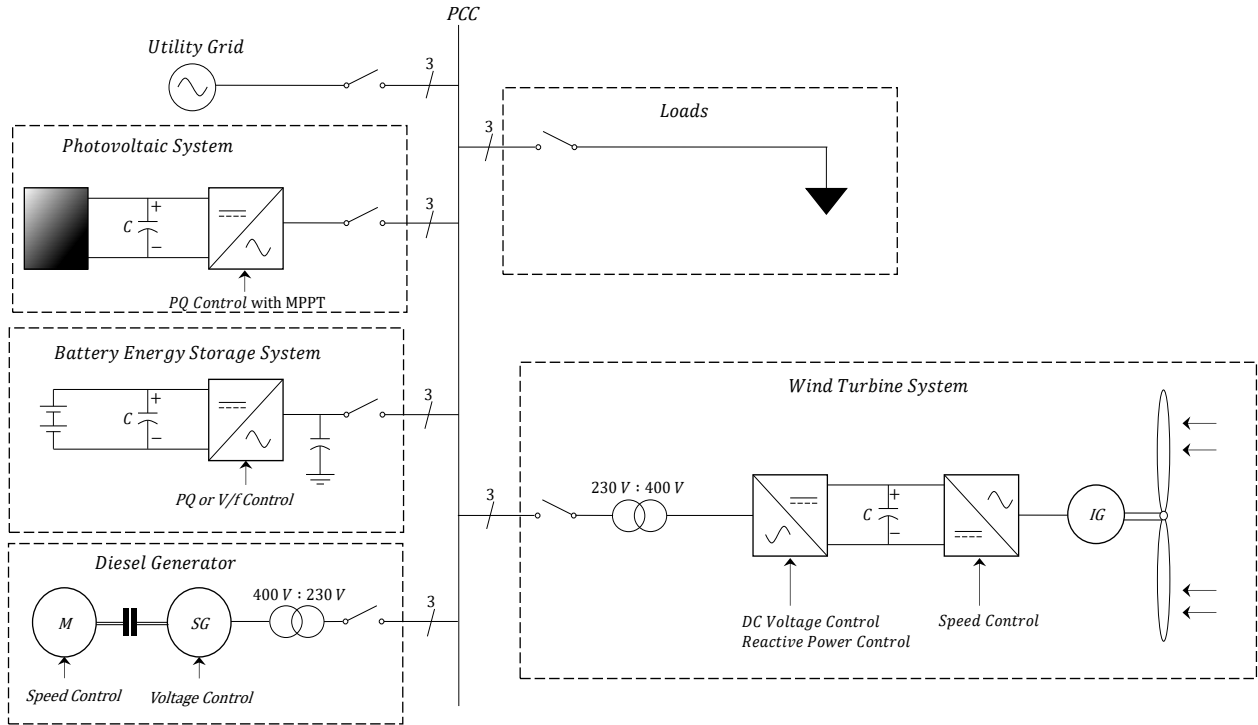


Figure 3.1. Schematic Presentation of the Proposed Microgrid

3.2 Control Strategy

In this thesis the objective is to implement a control strategy that provides a stable and robust microgrid operation when grid-connected, islanded, and in the transition between these. The control strategy depends on the state of the microgrid, where it is separated between the grid-connected mode and islanded mode. It is pointed out that the strategy is presented here, and the actions are followed out in simulation. Thus, the control is not implemented as an autonomous control system that can operate fully on its own.

3.2.1 Grid-Connected Mode

In grid-connected mode, the microgrid power sources operates as PQ-units. For the PV, and WT system the aim is to harvest the full amount of power available, while the BESS operates according to overlaying charge- and discharging schemes. The optimal charge- and discharge of the BESS depends on the objective, e.g. it could act on the cost of electricity or remaining at an optimal *State of Charge* (SOC) to increase run-time during islanded mode. This control scheme is not implemented in this thesis to restrict the scope. A series of previous work on the control scheme can however be found in literature, amongst these some implements machine learning for prediction and optimization [4] [5]. The diesel generator is not operating in grid-connected mode.

For the WT- and PV system these are normally set to operate at unity power factor. The BESS can also be set to operate at unity power factor, but beneficial gains from either providing or consuming reactive power during charging- and discharging could be considered. Considering an ideal VSC and battery, where resistive losses are neglected, this would not reduce the battery SOC.

3.2.2 Islanded Mode

In islanded mode there are various techniques for operation and control of the microgrid. In this thesis, the BESS operates as a master that controls voltage and frequency when in islanded mode. The WT- and PV system are mainly set to operate as PQ power sources. For the WT some experimentation with a droop controller have gained beneficial results in reducing the frequency deviations [6], thus implemented for specific scenarios. But with both the solar irradiance and wind speed being intermittent resources their available contribution varies and even though they have a positive influence, their ability to contribute is not constant. Hence, for worst case scenarios their contribution might be non-existing.

To keep the voltage around its nominal value, a voltage controller is implemented in the BESS. This acts on the difference between the measured voltage and the reference voltage. For frequency control a simple internal oscillator provides a reference for the VSC [7] [8]. This gives a reference tracking for the BESS, while the PV and WT continues to utilize the *Phase Locked Loop* (PLL). The reference signal could have been provided from a droop control method as used in [9], [10], [11], [12]. Normally, the traditional droop controller assumes a predominantly inductive grid, which is used as an assumption to decouple the active- and reactive powers impact on frequency and voltage, respectively [13]. However, in the low voltage microgrid, this assumption does not hold true, and the active- and reactive power is governed by (3.1) and (3.2), where subscripts 1 and 2 describes two systems separated by a line impedance. This can be solved by implementing a virtual impedance in the control [12]. However, this method is not implemented in this thesis, but a comparison between the internal oscillator method and the virtual impedance droop control is prosed for further work.

$$P = \frac{V_1}{R^2 + X^2} [R \cdot (V_1 - V_2 \cdot \cos\delta) + X \cdot V_2 \cdot \sin\delta] \quad (3.1)$$

$$Q = \frac{V_1}{R^2 + X^2} [-R \cdot V_2 \cdot \sin\delta + X \cdot (V_1 - V_2 \cdot \cos\delta)] \quad (3.2)$$

If the BESS capacity is outside the specified lower- or upper SOC limits, the diesel generator is activated with V/f-control. Ideally would the diesel generator start up to reach its operating temperature before the BESS switches from V/f- to PQ-control. This is however not implemented in the proposed control.

3.3 Voltage Sourced Converters

This section gives a brief introduction to the principle of operation for the VSCs and the deduction of the inner current control loop used for the electronically coupled power sources in the microgrid. The aspects of switching procedure and various transistor technologies are not covered in this thesis. It is therefore referred to [14] for a deeper insight to the theory behind the operation of the VSC.

3.3.1 Principle of Operation

The electric power sources in the microgrid produce power with voltages that are not in synchronism with the nominal voltage and frequency of the area. For the PV system and BESS these produce a DC-voltage that needs to be transformed to an AC-voltage of 50 Hz at the nominal voltage. To realize this, a two-level VSC is implemented as an interface between the DC production units and the microgrid's PCC. The principle of the converter is presented in Figure 3.2, with v_a , v_b , and v_c represents the phase voltages related to the AC system side, while V_{dc} is the DC system side voltage of the converter. The capacitor on the DC side ensures that the DC-voltage is kept close to constant, while the AC side inductors are either implemented as a filter or can arise from a coupling transformer [15].

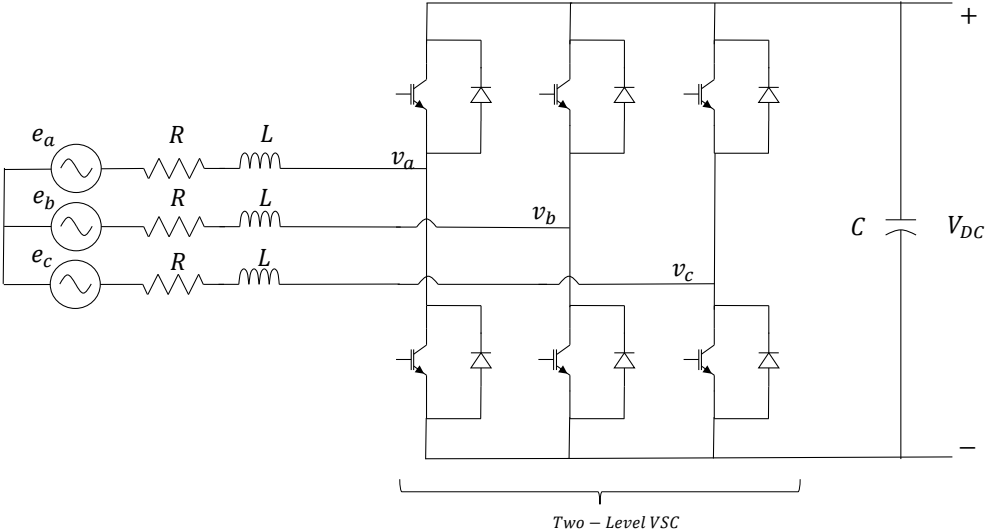


Figure 3.2. Two-Level VSC with IGBTs

To provide the desired output voltage the switches are triggered at specified instances. This creates a square waved output voltage where the voltage magnitude is equal to the DC-voltage. As the switching frequency can be significantly higher than the fundamental frequency an approximated sinus waveform can be achieved. Depending on the choice of switches used, the switching frequency can be several kHz. In this thesis, *Insulated Gate Bipolar Transistors* (IGBT) are the preferred choice based on the voltage level, current and switching frequency. These are the widely used for integration of distributed resources [15],

and operates normally in the kHz range [14]. For control, the switch-mode converters use *Pulse Width Modulation* (PWM) techniques to control the triggering of the switches [14]. It is also pointed out that for the VSCs must be bidirectional in order to handle currents flowing both ways.

Another advantage of having electronically coupled power sources through VSCs is the lack of inertia provided by the VSC. This gives a decoupling of the mechanical and electrical system for the WT. The high switching frequency also contributes to a potential fast response of the system, where the response is dependent on the source, e.g. a battery responds quickly while a fuel cell requires a slower ramped change [15].

Considering a synchronous generator, the active- and reactive power is controlled by the internal machine angle and field excitation, respectively. By neglecting the resistances, letting the internal voltage be V_a , and the electrical system angle δ be the difference between the internal voltage and the system voltage, the active and reactive power from the VSC can be described by [15]:

$$P = \frac{V_a V_{sys}}{X} \sin(\delta) \quad (3.3)$$

$$Q = \frac{V_{sys}^2}{X} \left(1 - \frac{V_a}{V_{sys}} \cos(\delta) \right) \quad (3.4)$$

Given (3.4), this implies that the VSC can operate at unity power factor if the relation $V_a \cos(\delta) = V_{sys}$ is fulfilled. In fact, the fast regulation means that the VSC, theoretically, may operate at a power factor ranging from 0.0 leading to 0.0 lagging. However, if not specified, the power factor is normally set to 1.0 for distributed generation as this is economically favorable [15].

3.3.2 Generic Current Control

The inner control loop for all the VSCs connected power sources in this thesis include a current controller. Thus, the controller principles are presented in general instead of an individual deduction for each of the systems. For the control loops, the Park's transformation is used, and the control is deduced in the dq -reference frame. The following equations are mainly based on those given in [16] [17], and per unitized. This transformation from the abc -reference frame to the rotating dq -reference frame is provided in appendix D.

Referred to Figure 3.3 the system dynamics can be described with space-phasor equation (3.5) [16]:

$$L \frac{d}{dt} \vec{i}_{abc} = -R \vec{i}_{abc} + \vec{V}_{t,abc} - \vec{V}_{s,abc} \quad (3.5)$$

Per unitized and transferred to the dq reference frame the system dynamics can be presented with (3.6) and (3.7). L and R make up the series RL branch or filters often used for such

applications. The on-state resistance for the transistors are included in R as they are approximately constant [18].

$$v_d = \frac{L}{\omega_b} * \frac{di_d}{dt} - L\omega_0 i_q + Ri_d + \frac{V_{DC}}{2} m_d \quad (3.6)$$

$$v_q = \frac{L}{\omega_b} * \frac{di_q}{dt} + L\omega_0 i_d + Ri_q + \frac{V_{DC}}{2} m_q \quad (3.7)$$

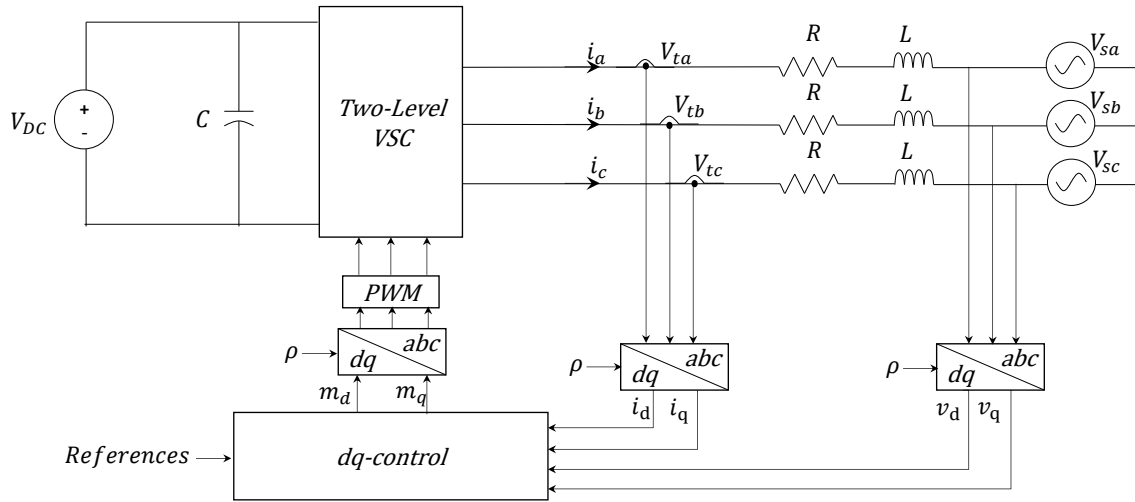


Figure 3.3. Schematic Two-Level VSC for Generic Current Control

From (3.6) and (3.7), i_d and i_q are state variables, v_d and v_q are disturbance inputs and m_d and m_q are control inputs. The dynamics are cross-coupled through the presence of $L\omega_0$ terms in both (3.6) and (3.7). By determining control inputs m_d and m_q in accordance with (3.8) and (3.9) the dynamics can be decoupled. Two new control inputs u_d and u_q are implemented to achieve the decoupling. Inserting equations (3.8) in (3.6) and (3.9) in (3.7) the resulting dynamics, in per unit, for the current controlled VSC are given in (3.10) and (3.11) [16].

$$m_d = \frac{2}{V_{DC}} (u_d - L\omega_0 i_q + v_d) \quad (3.8)$$

$$m_q = \frac{2}{V_{DC}} (u_q + L\omega_0 i_d + v_q) \quad (3.9)$$

$$\frac{L}{\omega_b} * \frac{di_d}{dt} = -Ri_d + u_d \quad (3.10)$$

$$\frac{L}{\omega_b} * \frac{di_q}{dt} = -Ri_q + u_q \quad (3.11)$$

The block diagram for the implemented current controlled VSC system is given in Figure 3.4. This shows that the system is represented by three parts. First a control system constituting of the PI-controller, then the time delay T_a representing sample- and hold and the PWM [19], and lastly the AC-side dynamics constituting of the RL branch. Transformed to the Laplace domain, the PI-controller is represented as (3.12). For the time delay this is included as a first order transfer function (3.13) with time constant T_a dependent on the switching frequency f_{sw} as given in (3.14) [17], with the gain of 1.5 is implemented to include sampling, hold and the PWM [19]. AC-side dynamics with a RL branch constitutes a first order transfer function (3.15) with time constant depending on R and L (3.16). Open loop transfer functions and tuning of the current controllers are presented in appendix F.

$$K(s) = K_{p,pu} \left(\frac{1 + T_i s}{T_i s} \right) \quad (3.12)$$

$$Y(s) = \frac{1}{1 + T_a s} \quad (3.13)$$

$$T_a = \frac{1.5}{2 * f_{sw}} \quad (3.14)$$

$$G(s) = \left(\frac{1}{R_{pu}(1 + T_{pu}s)} \right) \quad (3.15)$$

$$T_{pu} = \frac{L_{pu}}{R_{pu}\omega_{base}} \quad (3.16)$$

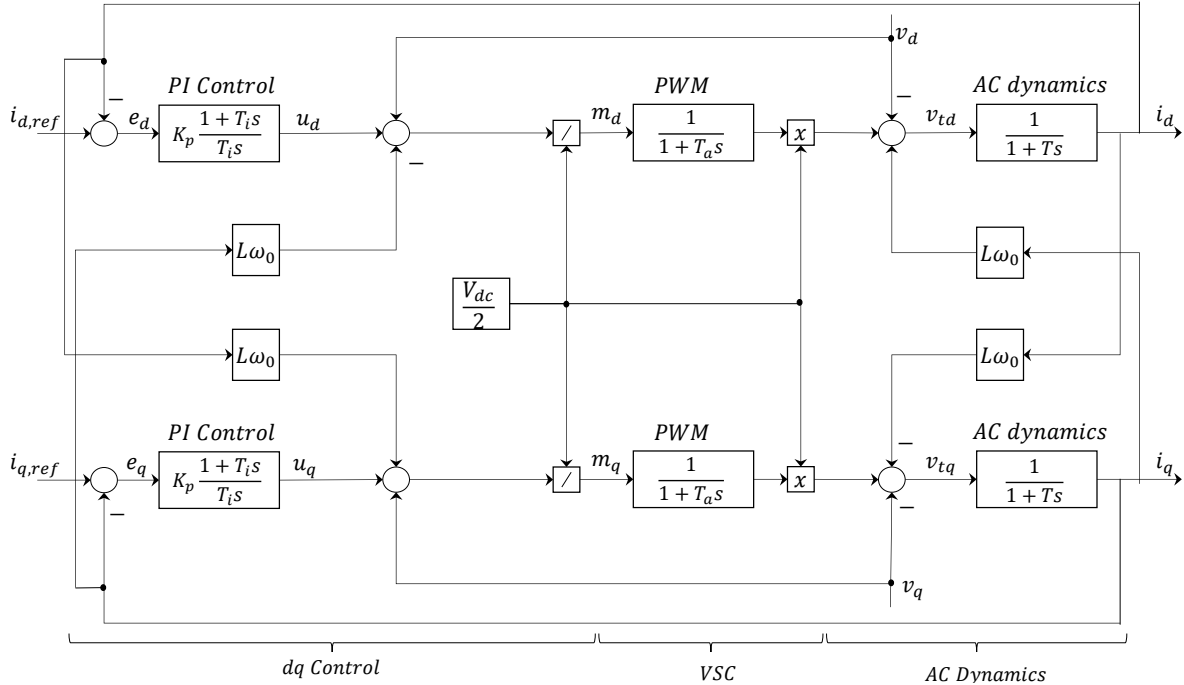


Figure 3.4. Block Diagram of Current Controlled VSC, based upon deduction in [16]

3.4 Existing Grid

Based on data provided by Sunnfjord Energy Nett a model of the existing grid was established in the Simulink environment. Figure 3.5 shows the connected loads and how they are connected to the distribution grid. In this section the mathematical expression and modelling of the lines, distribution grid and loads are further presented.

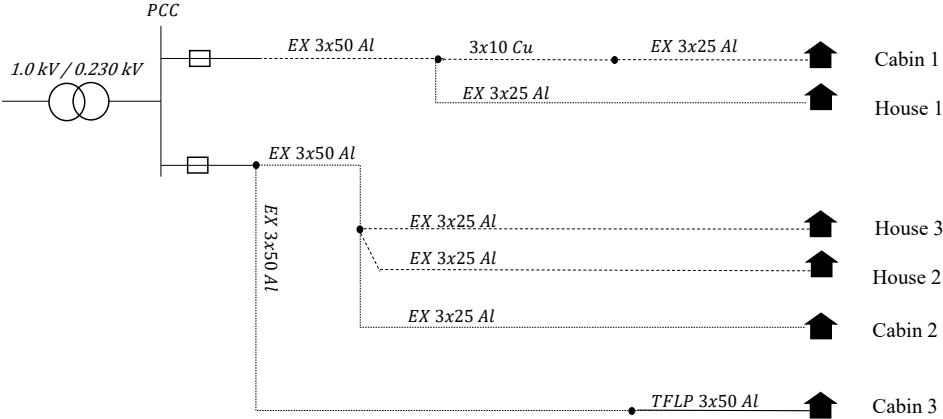


Figure 3.5. Existing Grid

3.4.1 Lines and Cables

The conductors are modeled with a three-phase π section line as shown in Figure 3.6. Since the lengths in the proposed case area does not exceed 1 km, each three-phase conductor is represented with one π -section. Utilizing π -sections has the advantage of being a linear model with finite number of states while disadvantage of a maximum frequency range that can be approximated by [20]:

$$f_{max} = \frac{N * v}{8 * l} \tag{3.17}$$

Where N represents numbers of π -section, v the propagation speed [km/s] and l the total line length [km]. Line lengths below 1 km modelled with one π -section should provide accuracy up to 37,5 kHz, thus the assumption of one section per line is valid. When considering higher frequency transients, a distributed line model should be considered for greater accuracy.

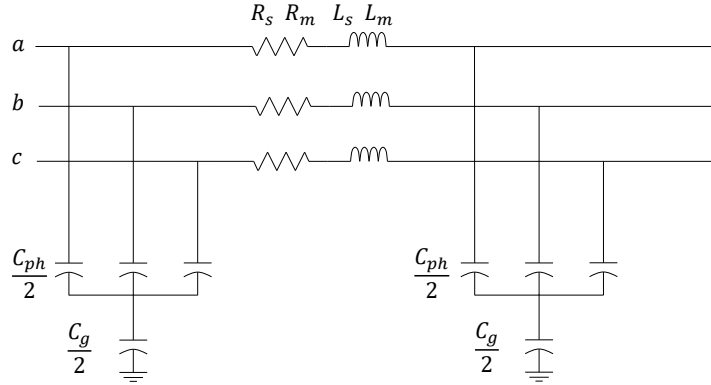


Figure 3.6. Three phase π -section line, based on n -section in [20]

For the positive-, negative- and zero sequence impedances these are obtained from Sunnfjord Energy Nett. Based on these line parameters the π -model quantities are estimated according to equations and impedances provided in appendix A.2. For long lengths (>50 km) hyperbolic correction should be utilized to obtain exact line model at specified frequency [21]. The Simulink block includes hyperbolic corrections in calculations, but for the proposed microgrid lines the correction factors will be close to unity, and hence not further considered.

3.4.2 Connection to Distribution Grid

The connection between the proposed microgrid area and the distribution grid is through a 1/0.23 kV YNyn0 transformer rated at 31 kVA. This transformer is disregarded during simulations as the distribution grid is modelled by a three-phase source acting with parameters according to appendix³ A.2. The source is modelled as a balanced three-phase voltage source with an RL impedance, as illustrated by Figure 3.7, with the dynamic properties of (3.18).

$$L_{th} \frac{d}{dt} \vec{i}_{abc} = \vec{V}_{abc} - R_{th} \vec{i}_{abc} - \vec{V}_{th,abc} - V_n \quad (3.18)$$

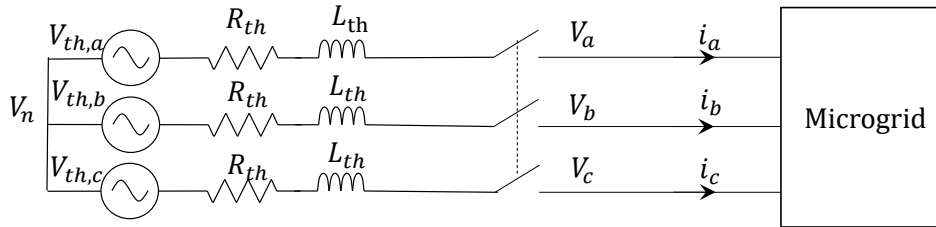


Figure 3.7. Modelled Connection to the Distribution Grid

³ Obtained from Sunnfjord Energi Nett AS at low-voltage side of transformer

3.4.3 Loads

The loads can be modelled as three-phase series- or parallel connected RLC loads with a star or delta configuration. In practice, the household loads will consist of composite loads where they are mostly connected between two phases, for IT-systems [3]. An assumption for further studies is that the complete load representing one resident can be modelled according to the dynamic model of a three-phase series connection shown in Figure 3.8, represented by [8]:

$$L \frac{d}{dt} \vec{i}_{abc} = -R \vec{i}_{abc} + \vec{V}_{abc} - \vec{V}_{C,abc} - V_n \quad (3.19)$$

$$C \frac{d}{dt} \vec{V}_{C,abc} = \vec{i}_{abc} \quad (3.20)$$

The loads power factor is altered by increasing, or decreasing, the inductive and capacitive components. In addition, the model allows for unbalanced loading per phase, which in practice often is the case for low-voltage distribution grids with households.

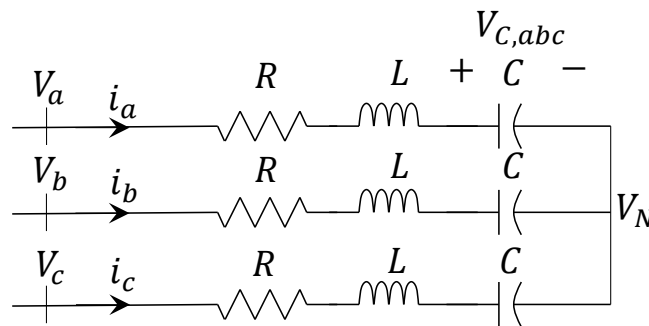


Figure 3.8. Series RLC Load

3.5 Photovoltaic System

In this section the mathematical representation of the PV array and the systems controls are presented. The PV system consist of a PV array connected through a two-level VSC where the output power is controlled by a *Maximum Power Point Tracking* (MPPT) algorithm, a DC-controller, and the inner current controller presented in section 3.3.2. Figure 3.9 gives an overview of the connected system.

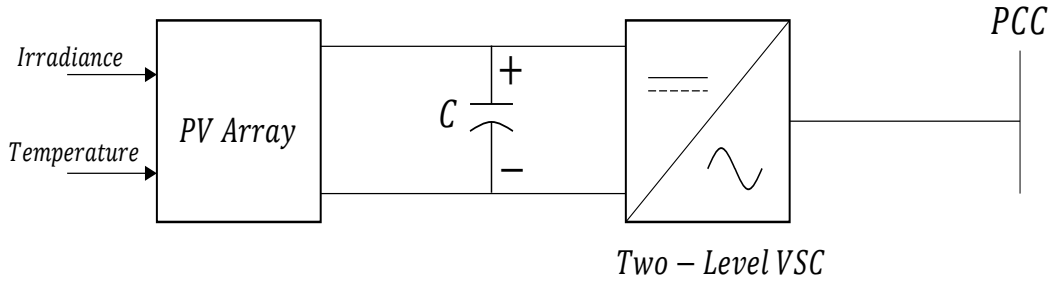


Figure 3.9. PV System

3.5.1 PV Array

The PV Array is based upon the prebuild PV array block from the Simulink Simscape library [22]. The block implements PV modules from the *National Renewable Energy Laboratory* (NREL) System Advisor. By defining *Standard Test Condition* (STC) parameters for the module, or choosing a predefined module, the array specifications are obtained. The current-voltage (I-V) characteristics for one module is set by (3.21) and (3.22) [22].

$$I_d = I_0 \left[e^{\frac{V_d}{V_T}} - 1 \right] \quad (3.21)$$

$$V_{module} = \frac{kT}{q} * nl * N_{cell} \quad (3.22)$$

Where I_d is the diode current [A], I_0 the diode saturation current [A], V_d is the diode voltage [V], V_T is the module voltage [V], k is the Boltzmann constant [J/K], T the temperature [K], q the electron charge [C], nl a ideality factor and N_{cell} the number of cells connected in series per module [22]. Main parameters and current-voltage (I-V) characteristics for the PV system is provided in appendix A.3.

3.5.2 Outline of Control Steps

The main objective is to operate at MPP for the PV array, which implies that the PV system produces the maximum power available. Further, the PV system is initially set to operate at unity power factor, i.e. not producing or consuming reactive power. To control and convert the DC-power from the PV array to three phase AC-power, the control steps provided in Table 3.1 is carried out.

Table 3.1. Outlined Control Steps of PV System Control

Control	Action	Input Signal	Output Signal
MPPT	Optimal DC-voltage (V_{MPP}) is calculated from a perturb and observe algorithm, based on the measured DC-voltage and current.	V_{DC} I_{DC}	V_{MPP}
Voltage Controller	The optimal DC-voltage is compared to the measured DC-voltage. Any deviation is handled through a PI-controller.	V_{MPP}	$i_{d,ref}$
Current Controller	dq-reference currents are compared to measured dq-currents and compensated according to the procedure presented in section 3.3.2. q-component set to zero if operating at unity power factor. Output signals are transferred to the <i>abc</i> -reference frame and processed by the PWM generator.	$i_{d,ref}$ $i_{q,ref}$	m_{dq}

3.5.3 MPPT Algorithm

Some of the main MPPT techniques available are the Perturb and Observe, Incremental Conductance, Ripple Correlation and various modified versions of these [23], [24]. In this thesis it is chosen to implement the Perturb and Observe algorithm because of its simplicity. The general idea is to periodically increment the output voltage and compare the obtained power with the previously measured power. If a change in voltage leads to an increase in power, the operation point is changed in that direction [23]. Otherwise, the operating point is changed in the opposite direction. This is further shown by a flow chart given in Figure 3.10. With a periodically increment, both the sampling period and the incremental change should be set to achieve an acceptable tradeoff between fast response and low fluctuation in steady state [23].

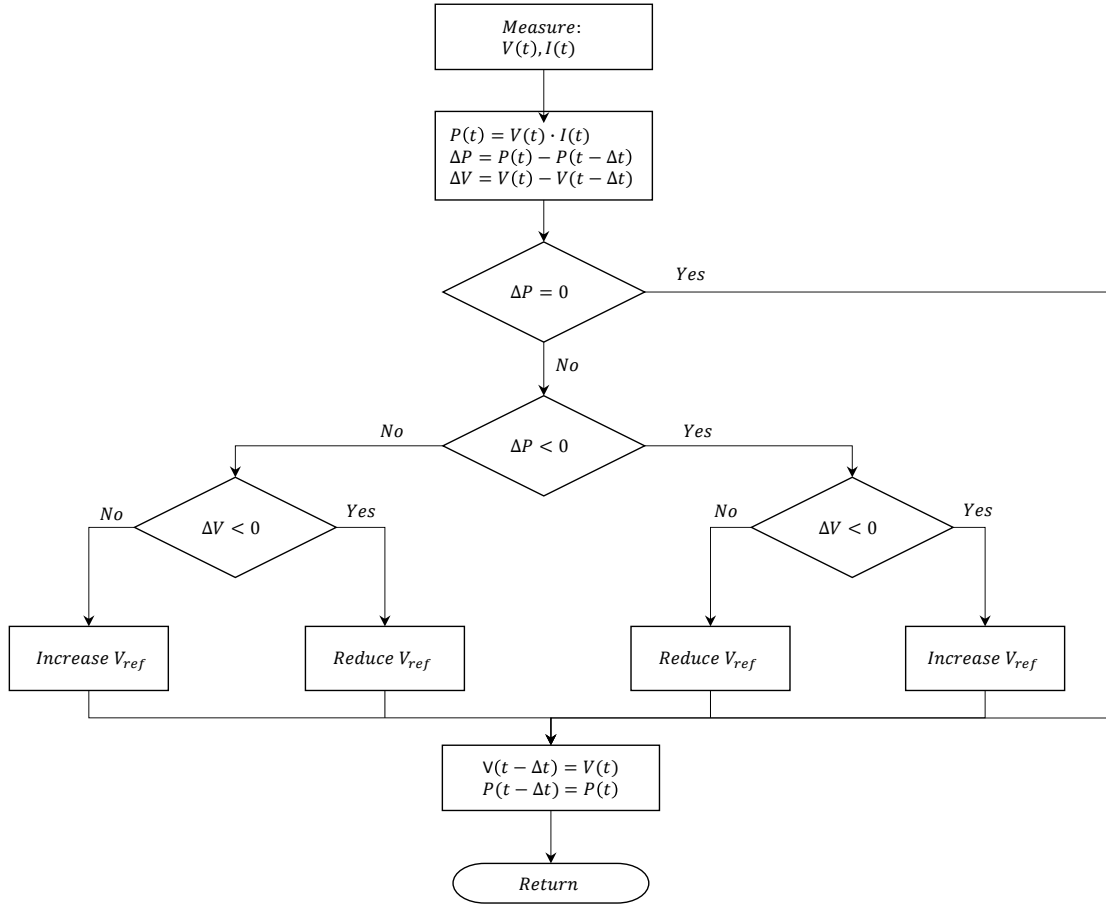


Figure 3.10. Flowchart for Implemented Perturb and Observe MPPT Algorithm [23]

3.5.4 DC Voltage Control

With the VSC connected to a PV application system, the DC side consist of a power source that varies according to solar irradiance and temperature. This implies that the DC-voltage needs to be regulated to control the power exchange with the AC grid [16]. The voltage control is based on a per unitized version of the presented equations in [17].

The DC-side dynamics can be described by applying *Kirchhoff's current law* (KCL) at point of connection for the DC-side capacitor (3.23) [17].

$$C \frac{d}{dt} V_{DC} = I_{DC} - I_{PV} \quad (3.23)$$

Where C is the DC-side capacitor, I_{DC} the current to the VSC and I_{PV} the current from the PV array. With the system represented in the dq-reference frame the per unitized power exchange between the DC and AC side are governed by (3.24) and (3.25).

$$P(t) = [v_d(t)i_d(t) + v_q(t)i_q(t)] = V_{DC}I_{DC} \quad (3.24)$$

$$Q(t) = [-v_d(t)i_q(t) + v_q(t)i_d(t)] \quad (3.25)$$

Hence the active- and reactive power exchanged is dependent on AC system voltage components and the reference currents. By assuming that the PLL is in steady state and aligned such that $v_{sq} = 0$ the per unitized power can be expressed as (3.26) and (3.27).

$$P(t) = [v_d(t)i_d(t)] = V_{DC}I_{DC} \quad (3.26)$$

$$Q(t) = [-v_d(t)i_q(t)] \quad (3.27)$$

By combining equation (3.23) and (3.26) the per unitized DC-side dynamics can be obtained:

$$\frac{1}{\omega_b C_{pu}} \frac{d}{dt} V_{DCpu} = \frac{v_{dpu}}{V_{DCpu}} i_{dpu} - I_{PVpu} \quad (3.28)$$

As this is a non-linear equation the system is linearized around its steady state operation point based on a Taylor series expansion according to [25]. By using Laplace transformation this can be presented in per unitized form as:

$$G_{DC}(s) = \frac{v_{dpu}}{V_{DCpu}} \cdot \frac{C_{pu}\omega_b}{s} \quad (3.29)$$

The block diagram of the DC-voltage control with the connections to the MPPT-controller and the current controller is shown in Figure 3.11. Open loop transfer function and tuning of the voltage controller is provided in appendix F.2.

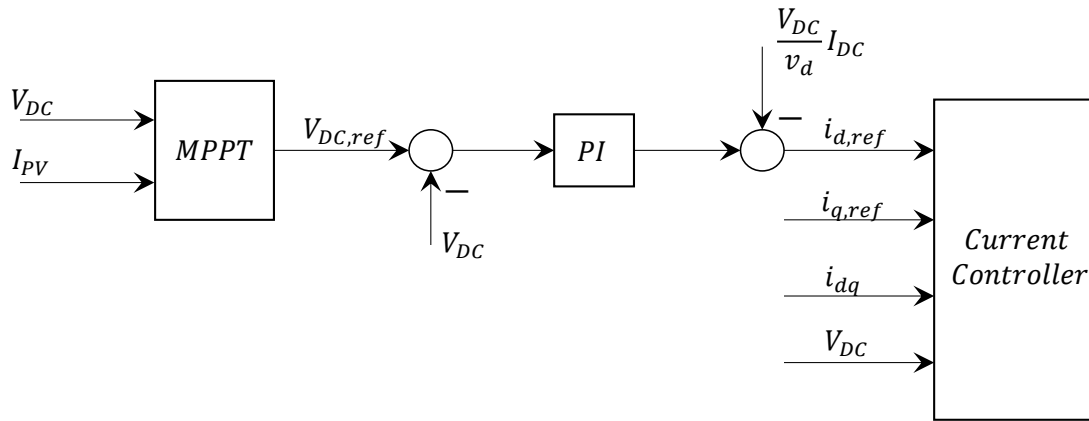


Figure 3.11. Block Diagram of Voltage Controller

3.6 Battery Energy Storage System

Due to the intermittency of both solar- and wind power, an energy storage is necessary for operation in islanded mode without the use of a diesel generator. Multiple storage solutions are possible for this, but lithium ion batteries stand out as one of the most cost-efficient solutions suited for the operation [3]. The battery energy storage system can provide electrical energy, on demand, if the SOC is above a set threshold and consume electrical energy if the SOC is below an upper limit. Figure 3.12 shown the BESS connection to the VSC and the dq-components obtained from the AC-side. The DC-side consist of a lithium ion battery model and a capacitor. In the following sections a brief introduction to the lithium ion battery is given, then the control strategy is presented, before the deduction of the power- and voltage controllers are provided. At last, island detection methods and implemented mode switch is presented.

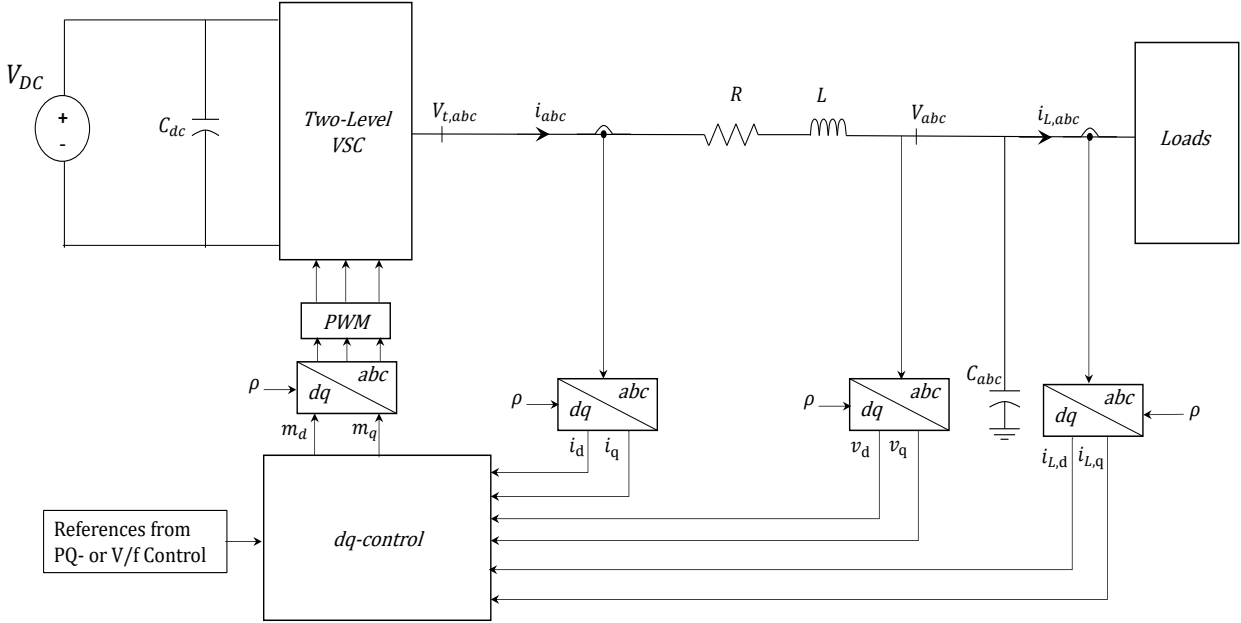


Figure 3.12. Battery Energy Storage System Overview

3.6.1 Applications and Lithium Ion Battery Model

In the specialization project both the applications and considerations associated with battery type selection was assessed [3]. There, Figure 3.13 summarized some of the main aspects to consider when applying and operating a BESS. By considering multiple technologies such as: Lead-Acid batteries, Sodium Sulphur batteries, Vanadium Redox Flow batteries and Lithium Ion batteries, the latter was highlighted as a mature and promising technology. This was validated by assessing storage projects that were announced, contracted and under construction in 2017, where lithium ion held the majority share [26].

Battery selection		
Ambient Temperature	Efficiency	Component cost
Space limitations	DoD	Maintenance requirement(cost)
Installation infrastructure	Performance requirements	Company warrants/performance guarantee
Safety	Utility grid requirements	Lifetime
Regulatory requirements	Energy Density	Replacement cost

Figure 3.13. Considerations for Battery Selection, based on [27]

The modelled lithium ion battery rack is based on the prebuild model provided in Simulink [28]. This model uses the modified Shepherd equation for describing the voltage dynamics at charging and discharging [28] [29]:

$$V_{B,charge} = E_0 - K \frac{Q}{it - 0.1Q} i \cdot (-K) \frac{Q}{Q - it} it + Ae^{-B \cdot it} \quad (3.30)$$

$$V_{B,discharge} = E_0 - K \frac{Q}{0.1it + Q} i \cdot (-K) \frac{Q}{Q - it} it + Ae^{-B \cdot it} \quad (3.31)$$

Where the parameter descriptions are collected in Table 3.2. With most simulations in this thesis being short term, the temperature and ageing effect is neglected. The parameters implemented are based on high energy modules manufactured by LG Chem [30]. Parameters and discharging curves are presented in appendix A.4.

Table 3.2. Battery Model Definitions [28]

V_B Nonlinear Voltage [V]	i Battery Current [A]	A Exponential Voltage [V]
E_0 Constant Voltage [V]	it Extracted Capacity [Ah]	B Exponential Capacity [Ah ⁻¹]
K Polarization Constant [V/Ah]	Q Maximum capacity [Ah]	

3.6.2 Outline of Control Steps

The general control strategy is to have the BESS function as a PQ-controlled source during grid-connected operation and at voltage- and frequency control during islanded operation. This possibility is realized through two outer control loops which is dependent on a mode command signal. At grid connected mode, the outer control loop consists of a simple PQ-control. For islanded mode, the outer control consists of a voltage controller and an internal oscillator to provide stable voltage and frequency in the microgrid. The outlined control steps are given in Table 3.3. The following sections deduces the power- and voltage control, while the inner control loop consists of a generic current controller as presented in section 3.3.2.

Table 3.3. Outlined Control Steps for the BESS

Mode	Control and Action	Input Signal	Output Signal
Grid-Connected	Outer PQ-Control Loop: PQ-controller provides current reference signals $i_{dq,ref}$ from the active- and reactive input signal P_{ref} and Q_{ref} , based upon equation (3.36) and (3.37).	P_{ref} Q_{ref}	$i_{d,ref}$ $i_{q,ref}$
	Inner Current Control Loop: dq-reference currents are compared to measured dq-currents and compensated according to the procedure presented in section 3.3.2. Output signals are transferred to the abc -reference frame and sent to the PWM generator.	$i_{d,ref}$ $i_{q,ref}$ i_d i_q	m_d m_q
Islanded	Outer Voltage Control Loop: Acting on the difference between voltage-reference $v_{dq,ref}$ and measured voltage v_{dq} . Outputs current reference signals $i_{dq,ref}$.	$v_{d,ref}$ $v_{q,ref}$ v_d v_q	$i_{d,ref}$ $i_{q,ref}$
	Inner Current Control Loop: Equal to Grid-Connected Mode	$i_{d,ref}$ $i_{q,ref}$ i_d i_q	m_d m_q

3.6.3 Power Controller

At grid-connected operation the BESS is not participating in voltage and frequency regulating. Thus, only a simple power controller decides the amount of power delivered or extracted. An overall control for charging and discharging might be included for studies over longer time periods, but this has not been implemented in this thesis. Equations presented are mainly deduced in [16] and per unitized according to per unit system given in appendix C.2.

With the system represented in the dq-reference frame, the per unitized power delivered at PCC are obtained with (3.32) and (3.33) [16].

$$P(t) = [v_d(t)i_d(t) + v_q(t)i_q(t)] \quad (3.32)$$

$$Q(t) = [-v_d(t)i_q(t) + v_q(t)i_d(t)] \quad (3.33)$$

From the equations the active- and reactive power is dependent on the AC system voltage components and the dq-components of the current. During grid connected mode the AC system voltage is assumed to be rather stable which implies that the power can be controlled by altering the dq current components. Further, by assuming that the PLL is in steady state and synchronized such that $v_q = 0$ the power can be expressed by (3.34) and (3.35).

$$P(t) = [v_d(t)i_d(t)] \quad (3.34)$$

$$Q(t) = [-v_d(t)i_q(t)] \quad (3.35)$$

Provided a fast reference tracking for the dq-current components the active- and reactive power can be independently controlled with $i_{d,ref}$ and $i_{q,ref}$ as given in (3.36) and (3.37) [16].

$$i_{dref}(t) = \frac{P_{ref}(t)}{V_{sd}(t)} \quad (3.36)$$

$$i_{qref}(t) = -\frac{Q_{ref}(t)}{V_{sd}(t)} \quad (3.37)$$

3.6.4 Voltage Controller

When the microgrid is operating in islanded mode the BESS provides voltage and frequency control. This is realized through a voltage controller which objective is to regulate the frequency and voltage of the PCC voltage, V_{abc} in Figure 3.12. In contrary to the other system components, the BESS has an AC-side filter composed of an RLC circuit. The implementation of the capacitive element is to ensure voltage support when loading conditions are unknown. In addition, the capacitive element will provide a low impedance path for harmonics generated from the two-level VSC [31]. The implemented voltage controller is based on the deduction performed in [32], and per unitized in accordance to per unit system in appendix C.2.

When the microgrid is connected to the utility grid a PLL ensures that the dq-reference frame rotates with an angular velocity of $\frac{d\rho}{dt} = \omega_n(t)$. In this thesis the generation of ρ is realized through a simple signal generator as shown in appendix G.3, but it is pointed out that other control strategies including a dynamically control of the frequency can be implemented [33]. During islanded mode this reference signal must be generated to align the d-axis as wanted. With V_{abc} obtained through (3.38), the alignment is made such that v_d and v_q are defined according to (3.39). This is the same choice of alignment as for the PLL during grid-connected operations.

$$\hat{V}_{abc,ph-g} = \sqrt{v_d^2 + v_q^2} \quad (3.38)$$

$$(v_d, v_q) = (1, 0) \quad (3.39)$$

By use of KCL at point of connection for the capacitor, see Figure 3.12, the load voltage dynamics can be described by space-phasor equation (3.40) [32]. Transformed to the dq-reference frame and per unitized, the voltage dynamics can be expressed as given in (3.41) and (3.42).

$$C_f \frac{d}{dt} \vec{V}_{abc} = \vec{i}_{abc} - \vec{i}_{L,abc} \quad (3.40)$$

$$\frac{C_f}{\omega_b} \frac{d}{dt} v_d = C_f \omega v_q + i_d - i_{Ld} \quad (3.41)$$

$$\frac{C_f}{\omega_b} \frac{d}{dt} v_q = -C_f \omega v_d + i_q - i_{Lq} \quad (3.42)$$

With V_{abc} being the pre-filtered voltage, i_{abc} the pre-capacitor current and $i_{L,abc}$ the load current. Further, C_f represent the capacitor capacitance, i_{Ldq} the dq-components of the load current, ω_b the base angular velocity and ω the per unitized angular velocity of the system. Provided with the dynamic equations, some observations can be made. Firstly, the dynamics of v_d and v_q are cross coupled through the term $C_f \omega v_{dq}$, which makes a decoupling desirable. Secondly, the voltage can be affected by altering the i_{dq} current references. And lastly, the load currents act as a disturbance that should be counteracted. By implementing two new control signals u_d and u_q , the decoupling and counteracting can be achieved [33]. These signals can be given as:

$$u_d = i_d - i_{Ld} + C_f \omega v_q \quad (3.43)$$

$$u_q = i_q - i_{Lq} - C_f \omega v_d \quad (3.44)$$

Implementing the new control signals with (3.41) and (3.42) and performing a Laplace transform yields a term with transient parts that will decay to zero in steady state [32]. By simplifications, explained in detail in [32], the expression can be expressed as (3.45) and (3.46) in per unit. Open loop transfer function and tuning can be obtained in appendix F.4.

$$\frac{v_d(s)}{u_d(s)} \approx H_v(s) \cdot \frac{\omega_b}{s C_{f,pu}} \quad (3.45)$$

$$\frac{v_q(s)}{u_q(s)} \approx H_v(s) \cdot \frac{\omega_b}{s C_{f,pu}} \quad (3.46)$$

3.6.5 Island Detection and Mode Switch

When transitioning from grid-connected operation to islanded operation, the BESS is dependent on a mode command signal to switch from PQ- to V/f-control. This command signal is provided when, or if, islanding is detected. Hence, to ensure correct operation in islanded mode there is a dependency on the island detection method. For islanding detection methods these can be divided into two main categories, local and remote, where the remote needs communication with the main grid [34]. The local methods are further divided into passive and active detection methods. The passive methods monitor variables or parameters, e.g. voltage- or frequency change. While the active intentionally injects disturbance signal to detect changes in parameters or variables, e.g. negative-sequence current injection [34].

For this thesis, the methods in themselves are not the main subject. However, the time delay associated with the various detection methods are of importance when considering unintentional islanding. The delay is naturally dependent on the chosen method, but the considered islanding detection methods in [34] suggest a time delay ranging from 4 ms to 2 s. Generally, for the passive methods the detection time is reduced when power exchange between the microgrid and main grid is increased. It should also be pointed out that islanding detection methods has non-detection zones that may reduce the reliability.

For the proposed microgrid a specific islanding detection method is not implemented. However, with the planned size and cost of the microgrid, the passive detection methods seem favorable. Thus, an assumed time delay between islanding and detection for passive detection methods is implemented for some of the simulations with unintentional islanding. Figure 3.14 gives a visual presentation of the proposed mode switch configuration with the implemented controllers and angular position reference.

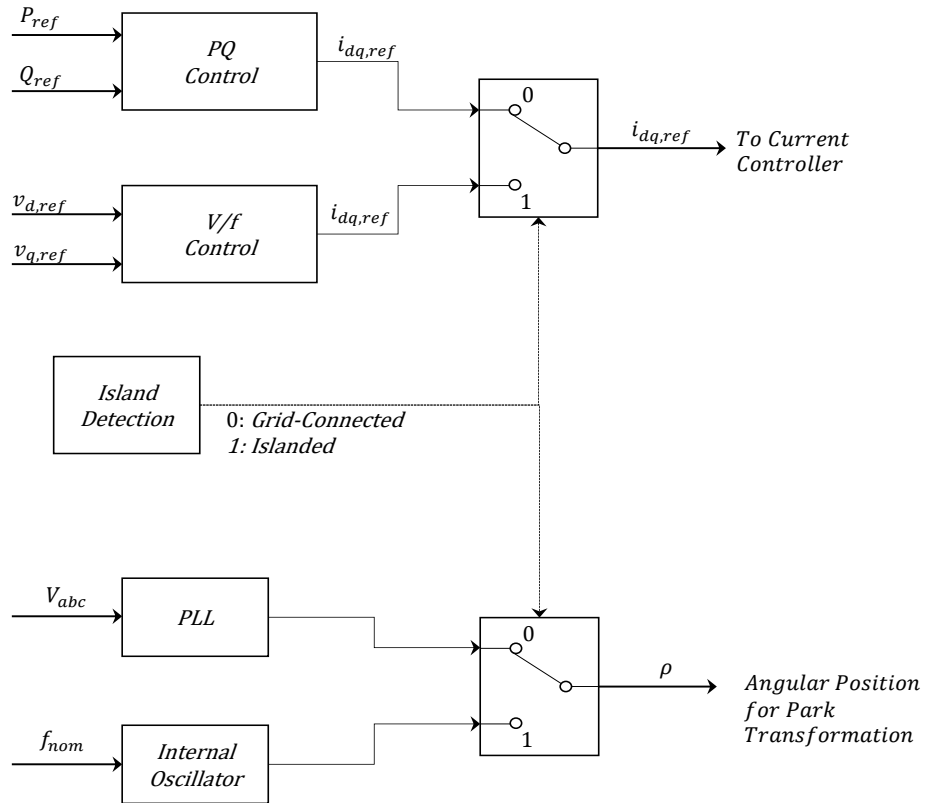


Figure 3.14. Change of Control with Mode Command from Islanding Detection

3.7 Wind Turbine System

Modelling of the wind turbine system has been performed in two ways, first an asynchronous generator directly coupled to the grid, and an electronically coupled wind turbine connected through a full power back-to-back power converter consisting of two-level VSCs. Through preliminary studies, the electronically coupled wind turbine has shown favorable performances, thus only this is further presented. According to IEC 61400-27-1 [35] this means that a Type 4 wind turbine is implemented. From [3] a 28 kW wind turbine was introduced during yearly energy calculations where both one and two wind turbines was considered. Therefore, the modelled wind turbine aerodynamics is based on the rotor efficiency for the wind turbine presented in [3], connected to a 30 kW induction generator. Figure 3.15 gives a schematic overview of the VSC connected wind turbine implemented in this chapter.

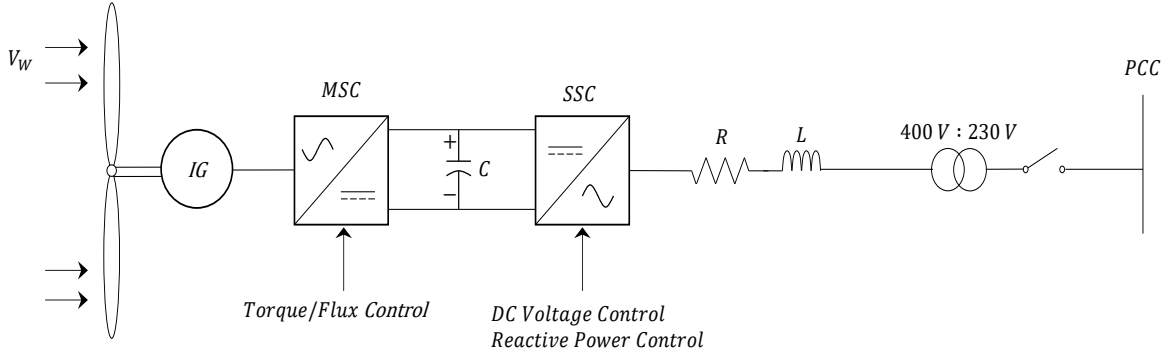


Figure 3.15. Schematic View of the Wind Turbine System

The following sections introduces the aerodynamics properties, blade pitch- and yaw control, and the drive train, before the induction generators and control system of the wind turbine system is presented.

3.7.1 Wind Turbine Aerodynamics

The principle of converting wind energy into electrical energy can be expressed according to (3.47).

$$P_m = \frac{1}{2} \rho \cdot A \cdot C_p(\lambda, \theta) \cdot V_w^3 \quad (3.47)$$

Where ρ is the air density [kg/m^3], A is the effective swept area [m^2], v_w is the wind speed [m/s] and C_p is the rotor efficiency⁴ [36]. The rotor efficiency is a function of the tip speed ratio λ and the pitch angle θ . With the tip speed ratio described by:

$$\lambda = \frac{\omega_m}{V_w} \cdot r_b \quad (3.48)$$

Where ω_m [rad/s] and r_b [m] is the rotational shaft speed and blade radius respectively. A common strategy for estimating the C_p is to implement an empirical formula as presented in (3.49) [37] [38] [39]. The values for constants c_1 to c_9 are dependent on the turbine design, mainly whether the turbine operates at constant- or variable speed [38]. Figure 3.16 and Figure 3.17 provides an example of the C_p with varying pitch angle θ for a variable speed turbine and C_p for a constant speed turbine. The constants used in this thesis, provided in appendix A.5, are estimated from manufacturer data and general values in [38].

$$C_p(\lambda, \theta) = c_1 \left(\frac{c_2}{\lambda_i} - c_3 \theta - c_4 \theta^{c_5} - c_6 \right) e^{-\frac{c_7}{\lambda_i}} \quad (3.49)$$

⁴ Also referred to as the power coefficient [86]

where

$$\lambda_i = \frac{1}{\frac{1}{\lambda + c_8\theta} - \frac{c_9}{\theta^3 + 1}} \quad (3.50)$$

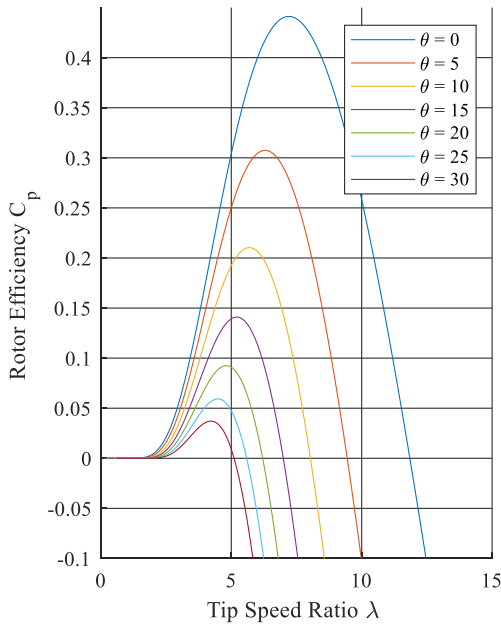


Figure 3.16. Rotor Efficiency: Variable Speed with $c_1 = 0.73$, $c_2 = 151$, $c_3 = 0.58$, $c_4 = 0.002$, $c_5 = 2.14$, $c_6 = 13.2$, $c_7 = 18.4$, $c_8 = -0.02$, $c_9 = -0.003$ [38]

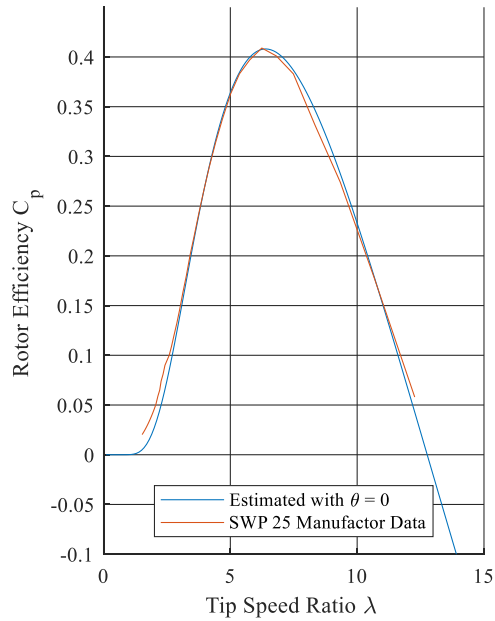


Figure 3.17. Rotor Efficiency: Constant Speed with $c_1 = 0.2$, $c_2 = 116$, $c_3 = 0$, $c_4 = 0$, $c_5 = 0$, $c_6 = 4.45$, $c_7 = 12.8$, $c_8 = 0$, $c_9 = 0.04$. And C_p -curve from SWP25 Wind Turbine [40].

Considering a stream tube where the wind passes the rotor blades, a portion of the kinetic energy will be extracted by the wind turbine. The upper theoretical limit of C_p is known as the Betz efficiency and gives a maximum rotor efficiency of $C_p = 16/27 \approx 0.59$. In practice, modern wind turbines can achieve a C_p of 0.4-0.5 during optimal operation conditions [36].

3.7.2 Blade Pitch Control

A common approach to optimize the power harvested from the wind is to implement a pitch control of the rotor blades. The effect of pitching the turbine blades allows for greater range of operating speeds of the turbine, as can be seen from Figure 3.16 where an optimal C_p can be achieved by altering the tip speed ratio. The pitch control also ensures that the power harvested will not exceed the generator rating by reducing the angle of attack at high wind speeds [36].

The wind turbine assessed in the long-term energy simulations in previous works [3] utilized a fixed pitch control. Thus, to ensure a correlation between the work performed in [3] and

this thesis, a blade pitch control is not implemented. With a fixed blade pitch, this implies that the operation range for the turbine speed is heavily reduced as the optimal tip speed ratio is achieved by operation at nominal rotor speed for nominal wind speed. Further, the fixed pitch reduces the ability of controlling the harvested power from the wind. This is however the drawback of many wind turbines in the proposed power range, where the absence of blade pitch control is justified by increased costs [41].

3.7.3 Yaw Control

Normally the objective of the yaw control is to rotate the nacelle such that the rotor blades are perpendicular to the wind direction. This leads to optimum wind conditions and hence maximum power production. The effect of not having the wind perpendicular to the rotor can be estimated by (3.51), where the effective area A_{eff} is reduced proportional to the cosine of yaw error angle ϕ [42].

$$A_{eff} = \pi R_{blade}^2 \cos(\phi) \quad (3.51)$$

The yaw control is available in the previously considered wind turbine from [3], and could have been implemented to provide power control. But with a maximum yaw rate limit around 0.03 rad/s [40] this yield to a rather slow control of power. The yaw control is therefore not implemented in the model. Instead, the wind direction is assumed to be perpendicular to the rotor at all time during simulations.

3.7.4 Wind Turbine Drive Train

The wind turbines system can be handled from complex multi-mass models to simple one-mass models. In [37] the rotor is modeled as a lumped mass and neglecting the shaft dynamics for a variable speed wind turbine. This is also known as the one-mass model where the rotor, shaft and gears are simply modelled as a rotating mass with a specified inertia. For wind turbines connected through power electronics (Type 4) this approximation can be acceptable as the shaft properties are barely reflected in the grid interaction [38]. The case is rather different for directly coupled turbines (Type 1) where the shaft properties is important for a correct behavior when exposed to voltage drops and short circuits [43]. A two-mass drivetrain could be considered a good tradeoff between accuracy of transient analysis and complexity for a Type 1 turbine [44], this is presented in appendix A.7. For the utilized WT (Type 4) the following lumped one mass drivetrain is included:

$$2H_{tot} \frac{d}{dt} \omega = T_m - T_e \quad (3.52)$$

Where H_{tot} , ω , T_m and T_e represents the total inertia, rotational speed, mechanical torque and electrical torque respectively. To estimate the inertia constant H_{wr} [s] for the rotor an estimation based on the power rating of the wind turbine can be used [45]:

$$H_{wr} \cong 1.87 * P^{0.0597} \quad (3.53)$$

3.7.5 Induction Generator

The induction generators mainly used in wind turbines are so-called squirrel cage induction generators where the rotor circuit is short circuited. Various rotor designs are available which affects the machines behavior during start-up and under transient conditions [46]. Main categories used for modelling is the single- and double cage induction generator, with the single cage studied in many literatures [47]. Figure 3.18 shows an equivalent per phase circuit, based on deductions in [46] [48], for both single (a.) and double cage (b.) induction machines with neglected core losses.

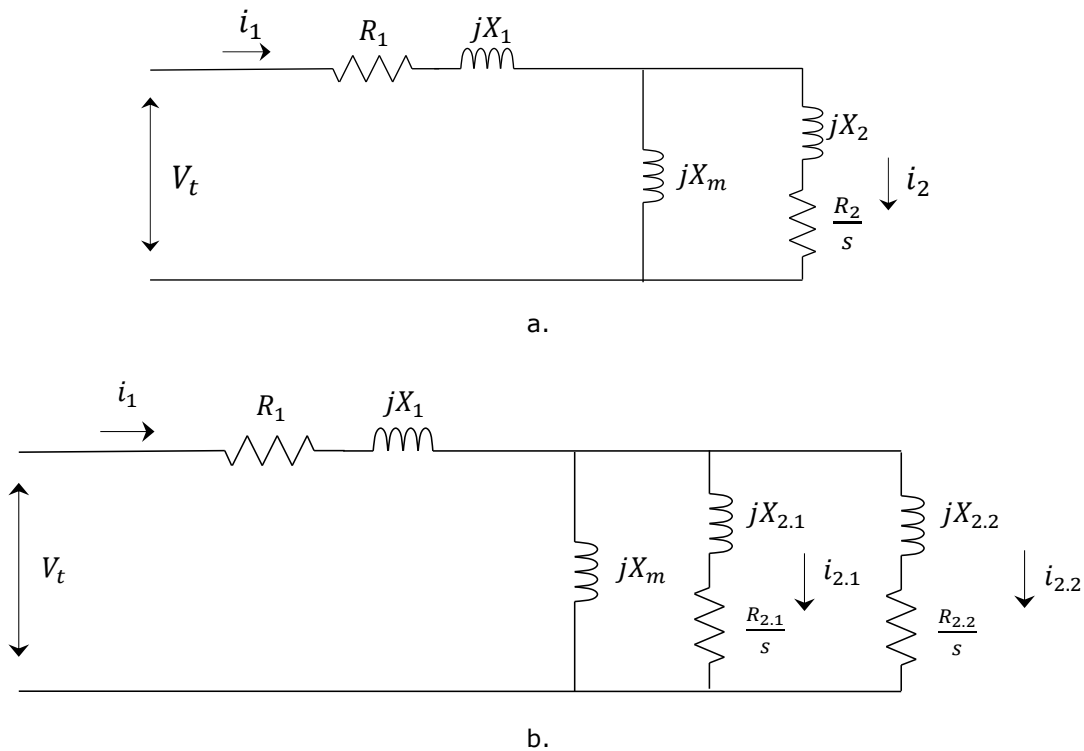


Figure 3.18. a. Single Cage Induction Machine, b. Double Cage Induction Machine

Where R_1 and X_1 denotes the stator effective resistance and stator leakage reactance, respectively. R_2 and X_2 are the referred rotor resistance and leakage reactance, while s is the slip, defined as:

$$s = \frac{n_{sync} - n_{mech}}{n_{sync}} \quad (3.54)$$

Where a positive slip indicates that the induction machine operates as a motor, while a negative slip indicates that the machine is operating as a generator. By further deducing a Thevenin equivalent of the single cage induction machine, the simplified equivalent circuit can be presented as shown in Figure 3.19 [48], where subscript Th indicates the Thevenin

equivalent. This equivalent circuit forms the basis for some fundamental relations between the induction machine parameters and performance. Now, the active power in the air gap P_{AirG} can be given as (3.55) [48]. Knowing that the torque is defined as power over the synchronous speed gives an expression for the torque developed by the induction machine (3.56) [48]. From these equations, two factors should be pointed out. Firstly, the torque is dependent on the squared Thevenin voltage, implying that the induction machine torque is sensitive to voltage changes. Secondly, the torque is proportional to the term R_2/s which is dependent on the rotor resistance and the slip of the machine.

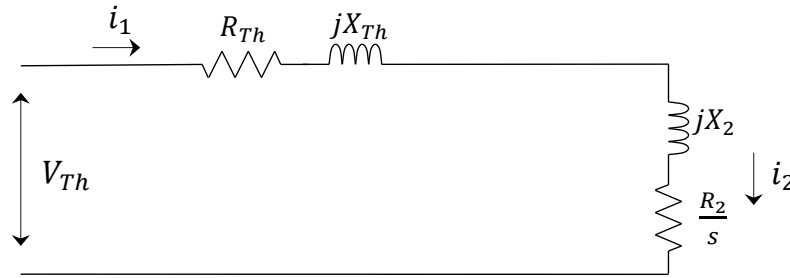


Figure 3.19. Simplified Thevenin Equivalent Circuit of the Single Cage Induction Machine

$$P_{AirG} = 3 \cdot I_2^2 \cdot \frac{R_r}{s} = \frac{3 \cdot V_{Th}^2}{\left(R_{Th} + \frac{R_2}{s}\right)^2 + (X_{Th} + X_2)^2} \cdot \frac{R_2}{s} \quad (3.55)$$

$$\tau = \frac{P_{AirG}}{\omega_{sync}} = \frac{3 \cdot V_{Th}^2}{\omega_{sync} \left(\left(R_{Th} + \frac{R_2}{s}\right)^2 + (X_{Th} + X_2)^2 \right)} \cdot \frac{R_2}{s} \quad (3.56)$$

A normal practice is to establish a 1st, 3rd or 5th order model of the single cage machine depending on the level of accuracy necessary. The first order model ignores the rotor and stator dynamics, the third order ignores the stator dynamics, while the fifth order is considered to be a full order model for an induction machine [49]. In [50] the author argues for use of a double cage model when estimating parameters from manufacturer data. In addition, it is in [47] shown that the double cage induction generator provides a better oscillation damping and frequency control than the single cage. Therefore, the induction generator presented in this thesis is a double cage model provided in the Simulink library [51].

The machine is represented by a 6th order state-space model with an 2nd order mechanical system [51]. The representation of the electrical and mechanical system in the dq-reference frame is provided in [51], with the parameters requested for the double cage induction generator given in Table 3.4. To estimate the necessary equivalent parameters, the estimation tool in [52] is used. The algorithm behind this is further described in [50] with testing on real machines with power ratings of the same magnitude as presented in this thesis. The input data to the algorithm is provided in standard manufacturer data sheets, while the

outputted parameters are those shown Table 3.4. Both input and output parameters are provided in appendix A.5.

Table 3.4. Output Parameters of Estimating Algorithm [52]

Description	Parameter
Stator Resistance [Ω]	R_s
Stator Leakage Inductance [H]	L_{ls}
Cage 1 and 2: Rotor Resistance [Ω]	R_{r1} and R_{r2}
Cage 1 and 2: Rotor Leakage Inductance [H]	L_{lr1} and L_{lr2}
Magnetizing Inductance [H]	L_m

3.7.6 Control of Machine Side Converter

As shown in Figure 3.15 the wind turbine is connected through two converters, one connected to the AC grid and one connected to the induction machine. In this section the main control principles of the *machine side converter* (MSC) is presented. Figure 3.20 gives the block diagram for the MSC where the wind turbine speed, torque and flux are controlled.

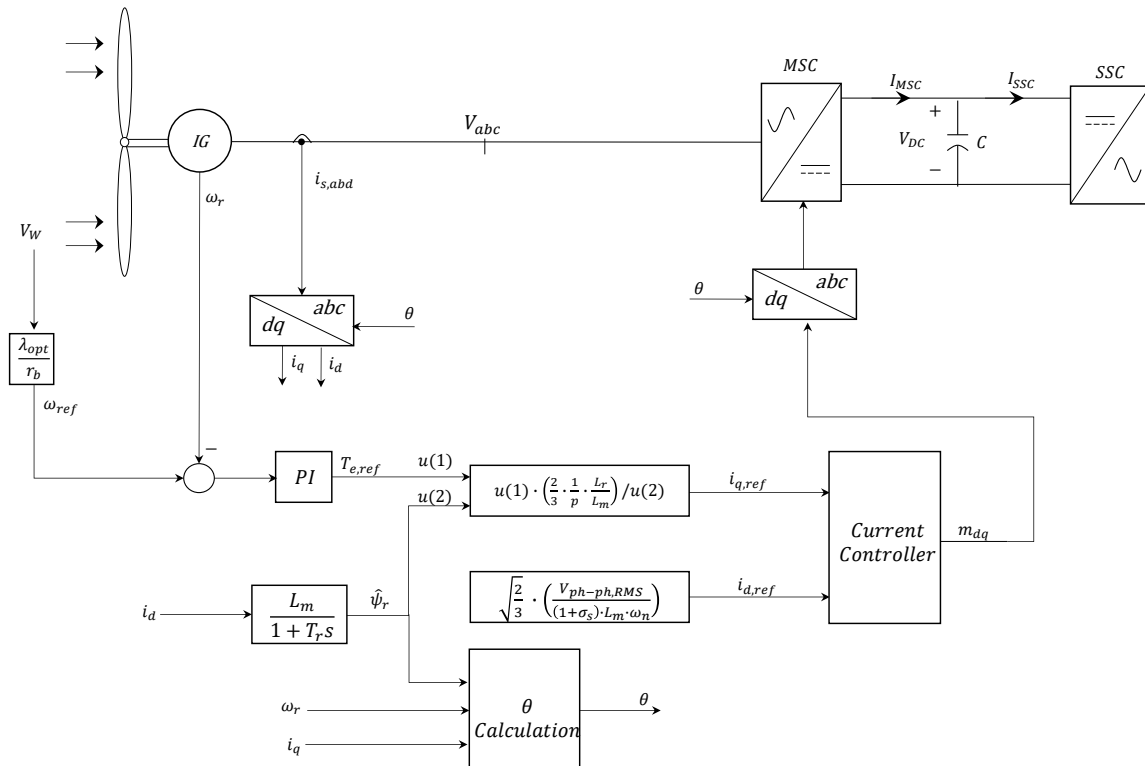


Figure 3.20. Control of MSC for Wind Turbine System

3.7.6.1 Speed Control

The speed reference is set according to the MPP given by (3.57), where the optimal tip speed ratio λ is obtained through the calculations of rotor efficiency previously presented in section 3.7.1. Through comparing the reference speed with the actual rotor speed, the difference serves as input to a PI-controller which in turn gives the reference electromagnetic torque from the relation given in (3.58).

$$\omega_{ref} = \frac{V_w}{r_{blade}} \lambda_{optimal} \quad (3.57)$$

$$T_{ref}(s) = k \frac{1 + T_i s}{T_i s} \cdot (\omega_{ref} - \omega) \quad (3.58)$$

3.7.6.2 Frequency Droop Control

With a full-scale power converter, the natural inertia response from the wind turbine is heavily reduced [6]. For a small microgrid this could be beneficial as variations has a lower impact on the electrical system. But during transient conditions it could be beneficial to utilize the inertia for system stability. Therefore, a droop control is included. Based on the frequency deviation, the electromagnetic torque reference is altered. This implies that the turbine can deliver extra power if the frequency is reduced, and less if the frequency is increased. When the droop control is activated, the speed control, presented in section 3.7.6.1, is disabled. A lower limit for the rotor speed is set to prevent the droop controller from stopping the turbine.

Depending on the inertia stored and frequency deviation this affects the turbines rotating speed. Thus, a high-pass filter is added to allow the turbine to restore to pre-fault conditions, and to not contribute in steady-state [6]. Figure 3.21 shows the conceptual idea behind the frequency droop control, while specific values for the droop control are varied for simulations.

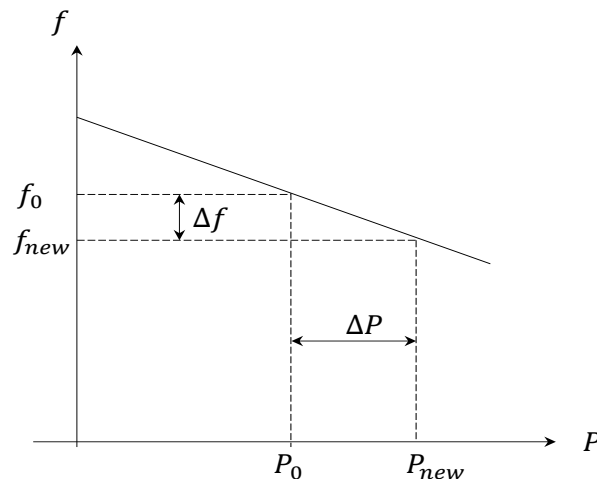


Figure 3.21. Frequency Droop Control

The reaction to change in frequency varies according to (3.59). With deviating frequency, the output power can be varied by altering the droop constant K_{droop} . However, the contribution will in practice be restricted by the inertia stored in the rotating mass of the wind turbine, i.e. if there is no wind the turbine cannot contribute.

$$\Delta P_{ref} = K_{droop} * \Delta f \quad (3.59)$$

This is a rather simple droop controller with a fixed droop method that gives an insight to the effect of applying droop control. It is however pointed out that adaptive droop control methods could also be beneficial to explore [53]. Especially since the availability of power from the WT is dependent on the wind speed.

3.7.6.3 Vector Control of Induction Machine

The induction machine terminals are connected to a VSC where the VSC controls the voltage and frequency experienced for the machine. By this, the machines torque and flux are controlled, which gives control over the extracted power and operating speed of the induction machine [31]. In the proposed control, the input variables are the torque from the speed control or the frequency droop control, and a reference flux set to the nominal flux of the machine.

The following dynamics and relationships for the vector control is based on the Parks transformation to the dq reference frame, and the representation of the induction machine in the dq reference frame as provided in [54]. The following section presents main relations and deductions for decoupled torque and flux control. Equations presented are mainly based on those given in [31] [54], with the subscripts in Table 3.5 used throughout this section.

Table 3.5. Subscripts for Deduction of Vector Control of Induction Machine

Subscript	Description
ed and eq	Electrical Reference Frame
sd and sq	Stator Reference Frame
rd and rq	Rotor Reference Frame
d	d-axis Component
q	q-axis Component

To perform the transformation from the rotating abc-frame to the rotating dq-reference frame, the rotor pole position is required. This can be found by considering both the rotor speed ω_r and slipping frequency ω_{slip} as shown in (3.60).

$$\theta_e = \int \omega_e dt = \int (\omega_r + \omega_{slip}) dt = \theta_r + \theta_{slip} \quad (3.60)$$

With θ indicating the position and ω the frequency. To provide a decoupled control of the flux and torque, the stator flux and torque current components, i_{sd} and i_{sq} , are aligned with the electrical dq-axis d_e and q_e , respectively [54]. This forms the foundation for the equivalent circuit of a single cage induction machine shown in Figure 3.22, derived in [54]. Provided with the equivalent circuit diagram, the rotor circuits can be represented by (3.61) and (3.62) [54].

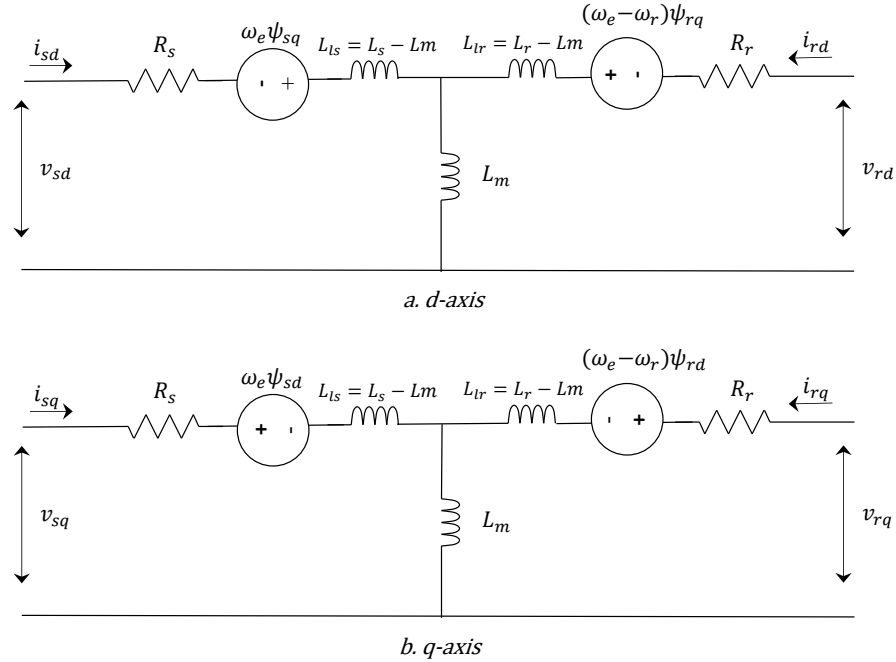


Figure 3.22. Equivalent Circuit Diagram of Single Cage Induction Machine in Electrical dq-Reference Frame, given in [54]

$$\frac{d\psi_{rd}}{dt} + R_r i_{rd} - (\omega_e - \omega_r) \psi_{rq} = 0 \quad (3.61)$$

$$\frac{d\psi_{rq}}{dt} + R_r i_{rq} - (\omega_e - \omega_r) \psi_{rd} = 0 \quad (3.62)$$

Where the $\psi_{r d/q}$ are the flux linkages for the d- and q-axis current components. From the electrical equivalent the flux linkage for d- and q- axis can be expressed as (3.63) and (3.64) respectively, with L_m being the mutual inductance [54]. This connects the dq components of the rotor currents with the dq component of the stator currents and allows for the removal of the unmeasurable rotor currents. Solving the flux linkage equations with respect to i_{rd} and i_{rq} and inserting these in (3.61) and (3.62) gives the rotor circuit equations (3.65) and (3.66) [54].

$$\psi_{rd} = L_r i_{rd} + L_m i_{sd} \quad (3.63)$$

$$\psi_{rq} = L_r i_{rq} + L_m i_{sq} \quad (3.64)$$

$$\frac{d\psi_{rd}}{dt} + \frac{R_r}{L_r} \psi_{rd} - \frac{L_m}{L_r} R_r i_{sd} - (\omega_e - \omega_r) \psi_{rq} = 0 \quad (3.65)$$

$$\frac{d\psi_{rq}}{dt} + \frac{R_r}{L_r} \psi_{rq} - \frac{L_m}{L_r} R_r i_{sq} + (\omega_e - \omega_r) \psi_{rd} = 0 \quad (3.66)$$

Equation (3.64) and (3.65) imply that a decoupled control can be achieved by letting the q-axis flux linkage $\psi_{rq} = 0$, which corresponds to aligning the rotor flux in the d-axis direction. This result leads to the important relationship used in modelling of the vector control, where (3.67) provides an estimation of the rotor flux [54], and (3.68) the transfer function. Further, when the rotor flux is assumed constant (3.69) gives the relationship between i_{sd} and the rotor flux $\hat{\psi}_r$ at steady state [54], where the total rotor flux $\hat{\psi}_r = \psi_{rd}$.

$$\frac{L_r}{R_r} \frac{d\hat{\psi}_r}{dt} + \hat{\psi}_r = L_m i_{sd} \quad (3.67)$$

$$|\psi_r|_{estimated} = \frac{L_m \cdot i_{sd}}{1 + L_r/R_r * s} = \frac{L_m \cdot i_{sd}}{1 + T_r * s} \quad (3.68)$$

$$i_{sd} = \frac{\hat{\psi}_r}{L_m} \quad (3.69)$$

Combined, the electrical torque can be expressed according to (3.70), with p representing number of poles [54].

$$T_e = \frac{3}{2} \left(\frac{p}{2}\right) \left(\frac{L_m}{L_r}\right) \psi_r i_{sq} \quad (3.70)$$

To provide a reference for i_{sd} , i.e. the nominal flux reference, the steady-state current is estimated by use of [31]:

$$i_{sd,ref} = \sqrt{\frac{2}{3}} \cdot \frac{V_{ph-ph,RMS}}{(1 + \sigma_s) \cdot L_m \cdot \omega_n} \quad (3.71)$$

$$\sigma_s = \frac{L_s}{L_m} - 1 \quad (3.72)$$

Output signals from the torque/flux control are the reference currents $i_{dq,ref}$. These are inputs to the current control, which follows the same procedure as the generic presented in section 3.3.2, with compensation for stator dynamics as given in [31], instead of the filter compensation. Open loop transfer function and tuning of the controllers are provided in appendix F.

3.7.7 Control of System Side Converter

The system side converter is set to control the DC-link voltage and the reactive power exchange from the wind turbine system. This is achieved through a DC-link voltage controller and a reactive power controller, acting on the d- and q-components of the current, respectively. Figure 3.23 gives the block diagram for the system side control, with the controllers derived in the following sections. The current controller implemented is the same as presented in section 3.3.2.

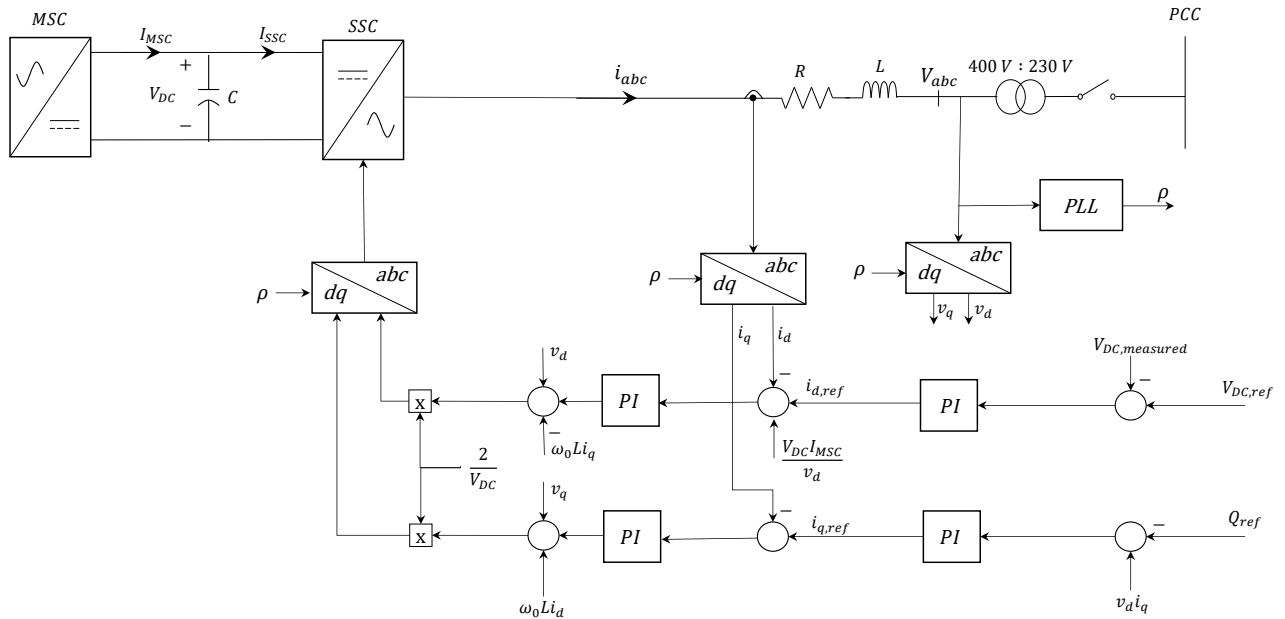


Figure 3.23. Control of SSC for Wind Turbine System

3.7.7.1 DC Voltage Control

The DC-link voltage controller is like the presented DC voltage controller for the PV system. Therefore, only the main equations are presented in this section, for detailed derivations see section 3.5.4.

The DC-link dynamics can be described by applying KCL at point of connection for the DC-side capacitor (3.73) [17].

$$C \frac{d}{dt} V_{DC} = I_{MSC} - I_{SSC} \quad (3.73)$$

Where C is the DC-side capacitor, I_{MSC} the current from the MSC and I_{SSC} is the current to the SSC, referred to Figure 3.23. By assuming that the steady state operation and alignment such that $v_q = 0$ the per unitized power can be expressed as (3.74) and (3.75) [17].

$$P(t) = [v_d(t)i_d(t)] = V_{DC}I_{SSC} \quad (3.74)$$

$$Q(t) = [-v_d(t)i_q(t)] \quad (3.75)$$

By combining equation (3.73) and (3.74) the per unitized DC-side dynamics are given as [17]:

$$\frac{1}{C_{pu}\omega_b} \frac{d}{dt} V_{DCpu} = \frac{v_{dpu}}{V_{DCpu}} i_{dpu} - I_{MSCpu} \quad (3.76)$$

Open loop transfer function and tuning of the voltage controller is provided in appendix F.7.

3.7.7.2 Reactive Power Control

In similarity to the other VSC connected generation units, the wind turbine system can contribute with reactive power production or consumption. This could have been implemented in the same fashion as for the frequency droop controller, where the reactive power reference is altered when deviations in the voltage is measured. However, in grid connected mode it is anticipated that the grid will provide the necessary voltage support, while the BESS acts as a master unit during islanded mode. If a voltage droop control was to be implemented, the predominantly resistive nature of the low voltage microgrid should be accounted for, as shown in [12] [13] [55].

The reactive power control in this thesis is however limited to acting on a reference power, which is normally set to zero to operate at unity power factor. The implemented controller compares the reference reactive power with the measured reactive power, given by (3.77) [17]. The resulting error is then regulated through an PI controller which outputs the q-current reference $i_{q,ref}$.

$$Q(t) = [-v_d(t)i_q(t)] \quad (3.77)$$

Compared to a directly coupled induction generator, this is highly beneficial as there is no need for reactive power compensation in form of capacitor banks. Open transfer loop and tuning of the reactive power controller is provided in F.8.

3.8 Diesel Generator System

The diesel generator system consists of a combustion engine connected through a clutch to a generator. Standalone diesel generator systems mainly utilize a synchronous generator [56], and with the capability of providing reactive power, a synchronous generator is also chosen for the proposed microgrid. Modelling of the diesel generator system consists of these main elements:

- Combustion engine
- Speed governor
- Excitation system
- Synchronous generator

Figure 3.24 shows a schematic view of the diesel generator system components. In [3] it was highlighted the challenges of running the diesel generators on low load, and a proposed configuration of multiple lower rated generators was presented instead of a single generator. Hence, the diesel generator system should consist of multiple low rated generators. In this thesis a single 15 kVAr rated system is implemented during simulations. However, this system can be duplicated to increase the system reliability. If parallel operation is to be performed, measures should be taken to avoid the diesel generators from swinging against each other, which could lead to oscillations in the system.

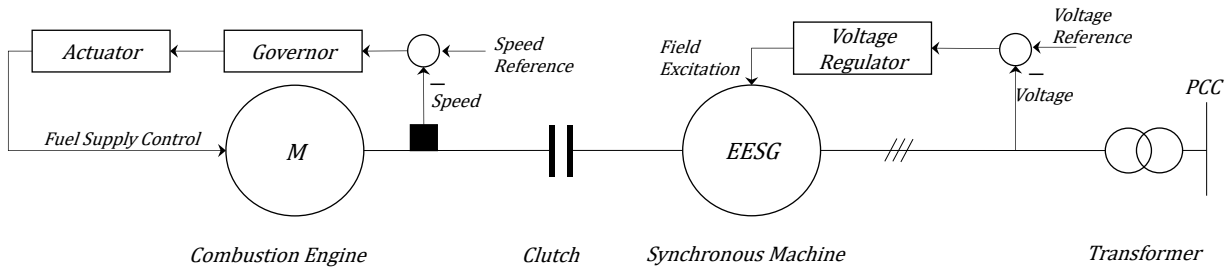


Figure 3.24. Schematics of Diesel Generator

3.8.1 Internal Combustion Engine, Drivetrain and Control

The representation of a diesel generator can be modelled in various ways with large differences in accuracy, especially for the combustion engine modelling. In [57] the system is modelled with a second order speed controller, third order throttle actuator and the engine represented with a transport delay. This implies that the engine inertia is either neglected or implemented in the synchronous machine model. In [58], [59], [60] and the actuator is modelled as a first order transfer function, the engine as a transport delay, a flywheel as an integrator and including a friction- and disturbance factor.

In this thesis the regulator is modelled by a PI-controller according to (3.78), the actuator as a first order transfer function (3.79) and the combustion engine as a transport delay (3.80). The drivetrain is implemented as a two-mass model to include the shaft properties and the combustion engine inertia. The drivetrain parameters are set similar to those explored for the wind turbine in appendix A.7, while the actuator and engine parameters are based on those presented in [58] [59]. Full parameter list is presented in appendix A.6 and tuning of PI controller in appendix F.5.

$$H_{PI} = K_p \cdot \frac{(1 + T_i s)}{T_i s} \quad (3.78)$$

$$H_{act}(s) = \frac{K_a}{1 + T_a s} \quad (3.79)$$

$$H_{engine}(s) = K_e e^{-T_e s} \quad (3.80)$$

3.8.2 Synchronous Generator

The synchronous generator implemented is the pre-built model given in [61], where the electric system is represented by a sixth order state-space model such that dynamics from both stator, field and damper windings are considered. The parameters included for simulations are based upon the ABB 0180AA04 synchronous generator, designed for diesel and gas applications. A detailed parameter list is provided in appendix A.6.

Without going into depth on the synchronous machine theory, the functionality and ability should be presented. Essentially, electrical power is generated by conversion of applied shaft torque through the interaction of *magnetomotive forces* (mmf) in the electromagnetic fields of the machine [15]. By increasing the applied shaft torque, the angular difference, referred to as torque angle, between the stator- and rotor field will increase. This leads to an increase in electrical power from the machine. Figure 3.25 shows the basic equivalent model of a synchronous generator, with a voltage source and a reactance. V_t represents the terminal voltage, V_g represents the machine open circuit terminal voltage, while X_s is the synchronous reactance composed of the armature- and leakage reactance. The deduction of the synchronous machine basic model, based on the machine flux and phasor relationships, is neatly presented in [15].

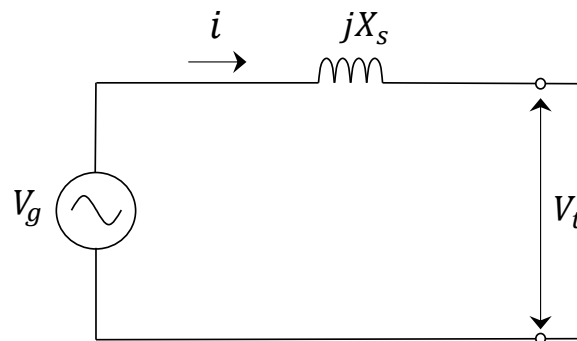


Figure 3.25. Simplified Synchronous Machine Per Phase Armature Equivalent Circuit

From an operating point of view, the synchronous generator can both deliver and absorb reactive power depending on the field excitation. Figure 3.26 gives an example of a typical synchronous generator capability curve, without considering the limitations of rotor- and stator current. This shows that the synchronous generator can increase the excitation to produce reactive power and reduce the excitation to absorb reactive power. The field regulation is in this thesis performed by a standard excitation system presented in the next section.

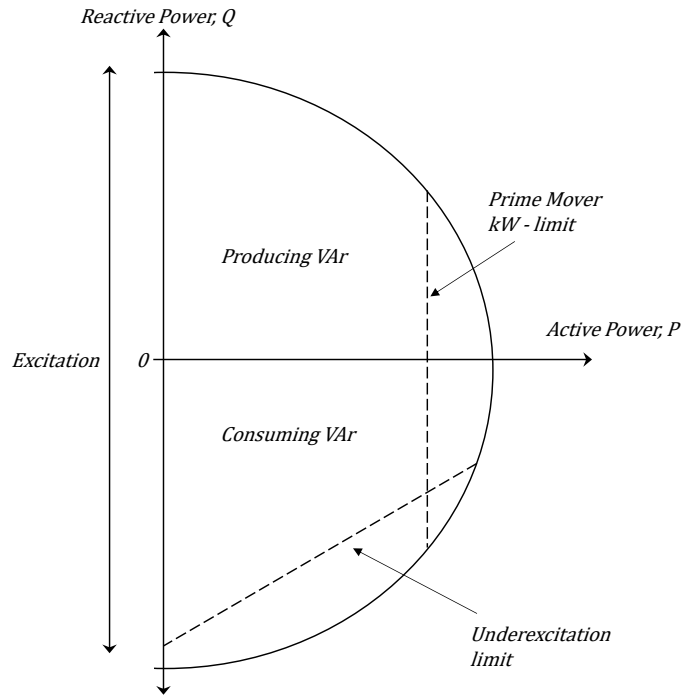


Figure 3.26. Capability Diagram for Synchronous Generator

Figure 3.27, rendered from [15], shows the phasor diagrams for operating at leading and lagging power factor with the parameters from Figure 3.25. The internal machine voltage V_g changes proportional to the applied field excitation, while the terminal voltage V_t is set to a fixed value. This process leads to a change in stator current, thus defining whether the machine operates at leading or lagging power factor [15]. It should also be noticed that the torque angle δ remains constant as the voltage drop over the synchronous reactance is not changed. This implies that the active power production is equal for the two scenarios [15].

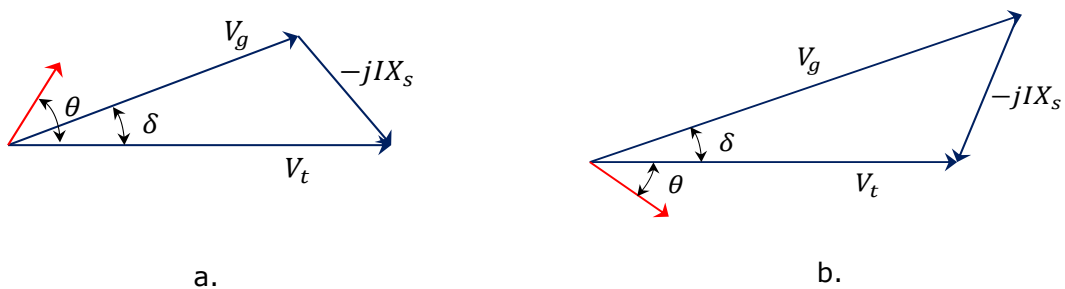


Figure 3.27. Phasor Relationship for Synchronous Generator [15].
 a. Absorbing Reactive Power, b. Consuming Reactive Power

3.8.3 Excitation System

The excitation system implemented is the AC5A excitation model based on recommended practice in [62]. The excitation system is adopted from the pre-build model provided in the Simscape library [63]. AC5A is chosen because of the uncertainty of vendor choices in the microgrid. Based on the previous standard [64], the AC5A is widely used by the industry and can be used when detailed data are not available or for simplified models. Further, the AC5A represents a simplified brushless excitation system where the regulator is supplied from a permanent magnet generator or similar sources that are not affected by system disturbances [64]. Alterations to the system parameters in the AC5A model are not executed, however it might be favorable if extensive simulation with the diesel generator activated are to be performed in further work.

4 Validation of Subsystem Models

In this chapter, the subsystems are simulated to validate their behavior during operation. The subsystems consist of the existing grid, PV system, WT system, BESS and the DGR system. This should not be considered a full validation of the subsystem's behavior, but as a test of their main functionality.

4.1 Existing Grid

To validate some of the properties of the existing grid model, a series of three phase short circuit have been carried out. These are compared to obtained values from model used at Sunnfjord Energi Nett, in their software, Netbas.

4.1.1 System Response During Short Circuits

Three-phase short circuits has been simulated at the six connection points and at the PCC. The calculations are executed according to (4.1), with a voltage factor c , nominal phase-phase voltage U_n and positive-sequence equivalent impedance Z_k . For maximum short circuit currents, the voltage factor is set to 1.05 [65].

$$I_{k,3ph} = \frac{c \cdot U_n}{\sqrt{3} \cdot Z_k} \quad (4.1)$$

Table 4.1 summarize the short circuits currents at the connection point for customers from simulations, and from obtained values retrieved from Sunnfjord Energi Nett. For three-phase maximum short circuits the results are equal except for *Cabin 1* with a deviation of 4.5 % between the model and the obtained values. Cabin 1 is connected through an unknown copper conductor, which could be the reasoning for the difference. Results are otherwise considered satisfactory. Even though the results show a low short circuit current at the connection points, as discussed in [3], the currents and voltages could be higher as the tap changer position of the transformer is unknown⁵. Detailed parameter data for the existing grid is provided in appendix A.2.

⁵ Information from Sunnfjord Energi Nett AS

Table 4.1. Short Circuit Calculations in Simulink Model and Obtained Values from Netbas

	Simulink Model	Retrived from Netbas*
Connection point	$I_{k,3ph}$ [kA]	$I_{k,3ph}$ [kA]
PCC	0.809	0.809
House 1	0.557	0.557
House 2	0.621	0.621
House 3	0.637	0.637
Cabin 1	0.193	0.202
Cabin 2	0.565	0.565
Cabin 3	0.303	0.303

* Voltage factor: $c = 1.05$

4.2 PV System

The PV system validation is performed with the system connected to an infinite voltage source, corresponding to a Thevenin impedance equal to zero, referred to Figure 3.7. With varying solar irradiance, the system behavior is investigated throughout this section.

4.2.1 Numerical Parameters

Table 4.2 gives the PV system main parameters. The PV module data is based upon the REC Solar 260PE provided from [22], while the resistance, inductance and DC-capacitance is based around on the values given in [17] and [66], but are altered to enhance system performance. Further parameters and details on the PV module performance can be found in appendix A.3.

Table 4.2. Numerical Parameters, PV System

Parameter	Abbreviation	Value
Number of Modules	N_{mod}	120
Number of Strings	N_{string}	6
MPPT DC-Power at STC	P_{DC}	31.3 kW
MPPT DC-Voltage at STC	$V_{dc,nom}$	614 V
MPPT DC-Current at STC	$I_{DC,nom}$	51 A
Filter Inductance	L_f	0.92 p.u.
Filter Resistance and Switc	R_f	0.05 p.u.
DC-Capacitance	C_{DC}	1.36 p.u.

4.2.2 Power Output

Power output at Standard Test Conditions (STC) can be estimated according to (4.2) [67], which corresponds to approximately 32 kW when assuming efficiency factor of 16 %, DC-AC ratio of 1 and derating factor of 1. This corresponds well with the given MPPT power from Table 4.2 and resulting AC power of approximately 30 kW in Figure 4.1.

$$P_{AC}(t) \approx S(t) \cdot A_{PV} \cdot \eta_{PV} \cdot DF * \frac{R_{DC}}{AC} = 1 \frac{kW}{m^2} \cdot 200m^2 * 0.16 * 1 = 32 kW \quad (4.2)$$

4.2.3 Control Behavior

The PV system is coupled to the grid through a two-level VSC that regulates the DC-voltage based on the MPPT algorithm. As solar irradiance changes, the voltage reference is adjusted to obtain maximum power from the PV system. With the MPPT algorithm based on the perturb and observe technique, the voltage reference varies, according to chosen sampling time and voltage increment, to find the optimal point. The reference variation, even at close to steady-state, can be noticed in Figure 4.1.c. The measured DC-voltage is also seen to follow the reference DC-voltage satisfactorily.

Figure 4.1.d shows the dq-components of the reference- and measured current. The reference $i_{q,ref}$ is set to zero, which corresponds to operating at unity power factor. This is verified by zero production, or consumption, of reactive power in Figure 4.1.b. $i_{d,ref}$ is seen to vary according to the solar irradiance, and hence the active power as anticipated from equation

(3.26). Lastly, the measured i_{dq} currents are observed to follow their respective references throughout the simulation.

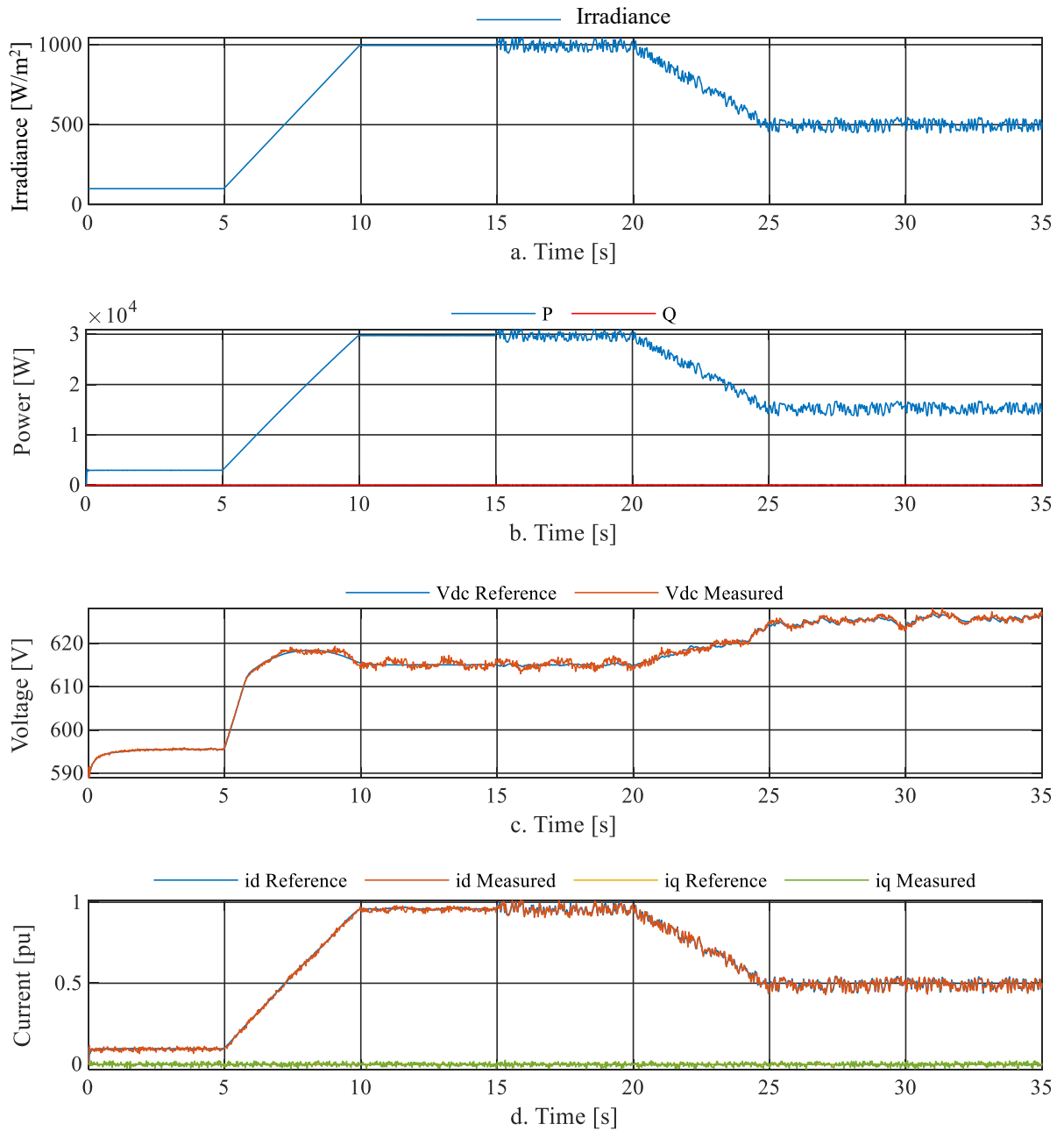


Figure 4.1. PV system validation, a. Solar irradiance, b. Power Output, c. DC-voltage, d. dq-Current Components

4.3 Battery Energy Storage System

To perform a system validation the BESS is connected to an infinity strong grid for testing of the power controller. Further, the system is disconnected and operates in islanded mode with varying load in order to validate performance of the voltage controller.

4.3.1 Numerical Parameters

Table 4.3 gives the main parameters for the BESS. These parameters are based on the high energy lithium ion battery modules from LG Chem [30]. The filter resistance, filter inductance and DC-capacitance is set to the same order of magnitude as for the PV system, while the rated energy of the battery is around the capacity suggested in previous workings of [3]. Further parameters of the battery system are provided in appendix A.4.

Table 4.3. Numerical Parameters, BESS

Parameter	Symbol	Value
Rated power	P_{nom}	32 kW
Rated Energy	E_{nom}	74 kWh
Nominal Voltage	$V_{dc,nom}$	514 V
DC Capacitance	C_{dc}	1.88 pu
Filter Inductance	L_f	0.95 pu
Filter Resistance	R_f	0.026 pu
Filter Capacitance	C_f	0.19 pu

4.3.2 Power Reference Response

In grid-connected mode, the BESS is controlled through a PQ-controller that determines the active- and reactive power consumption, or production. Provided with a reference power the BESS capability during both charging and discharging is controlled. Throughout the simulation, the BESS is connected to an infinity strong utility grid. The reactive power reference is adjusted to compensate for the capacitor bank such that the measured reactive power for the system corresponds to the reference. Figure 4.2.a and Figure 4.2.b shows that the resulting active- and reactive power follows their respective references as intended. The SOC level, see Figure 4.2.c, can also be noticed to decrease during discharging, and increase during charging of the batteries.

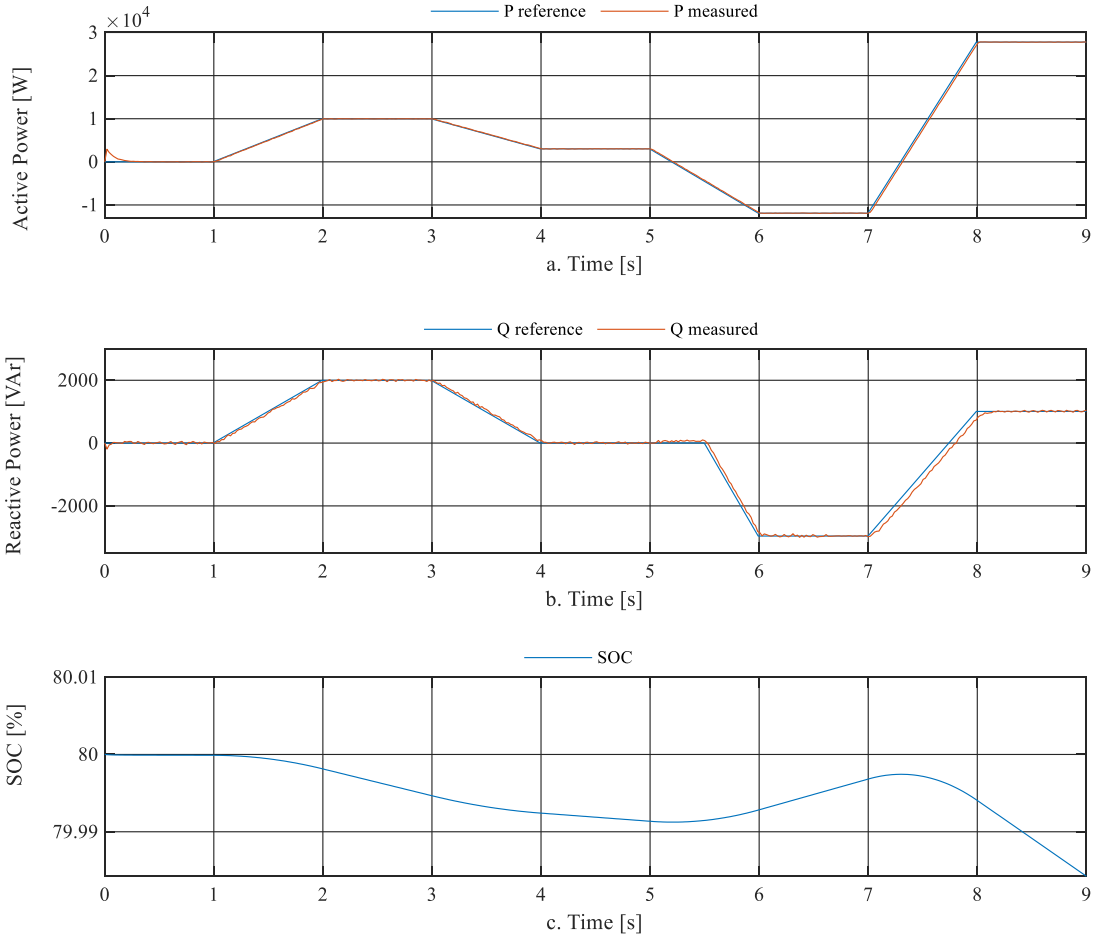


Figure 4.2. Power controller enabled: a. Active Power, b. Reactive Power, c. State-of-Charge

4.3.3 Islanded Operation

In islanded operation the BESS task is to regulate voltage and frequency to comply with the regulatory demands. The regulatory demands in Norway allows for a short-term voltage deviation of maximum 5 % and a frequency deviation as regulated by the Nordic administrative in general, and a deviation of maximum 50 Hz \pm 2 % during temporarily island operations [68]. The regulating capability is tested by altering the load connected to the BESS, according to Table 4.4. Figure 4.3 presents the power drawn by the loads, frequency, phase to ground voltage at PCC and the line current.

Table 4.4. Load scheme for islanded operation

Time	Load [kVA]	Loading pu
$t > 0$ s	$(1 + j0)$	$0.033 + j0$
$1 \text{ s} < t < 2 \text{ s}$	$(5 + j3)$	$0.167 + j0.1$
$2 \text{ s} < t < 3 \text{ s}$	$(25 + j10)$	$0.83 + j0.3$
$3 \text{ s} < t < 4 \text{ s}$	$(2 + j)$	$0.067 + j0.033$

Resulting simulations shows a fluctuating frequency with deviations of maximum 0.1 Hz at $t = 2$ seconds, as a large load is connected without ramping. Further a quite severe overvoltage of 50 % is observed at $t = 3$ s, as the large load is disconnected, with a duration less than one period. This is well above the regulations, but it should be noticed that this is at PCC with loads directly coupled to the BESS and not a part of the complete microgrid with lines and cables that would influence the resulting overvoltage at connection point of the consumer.

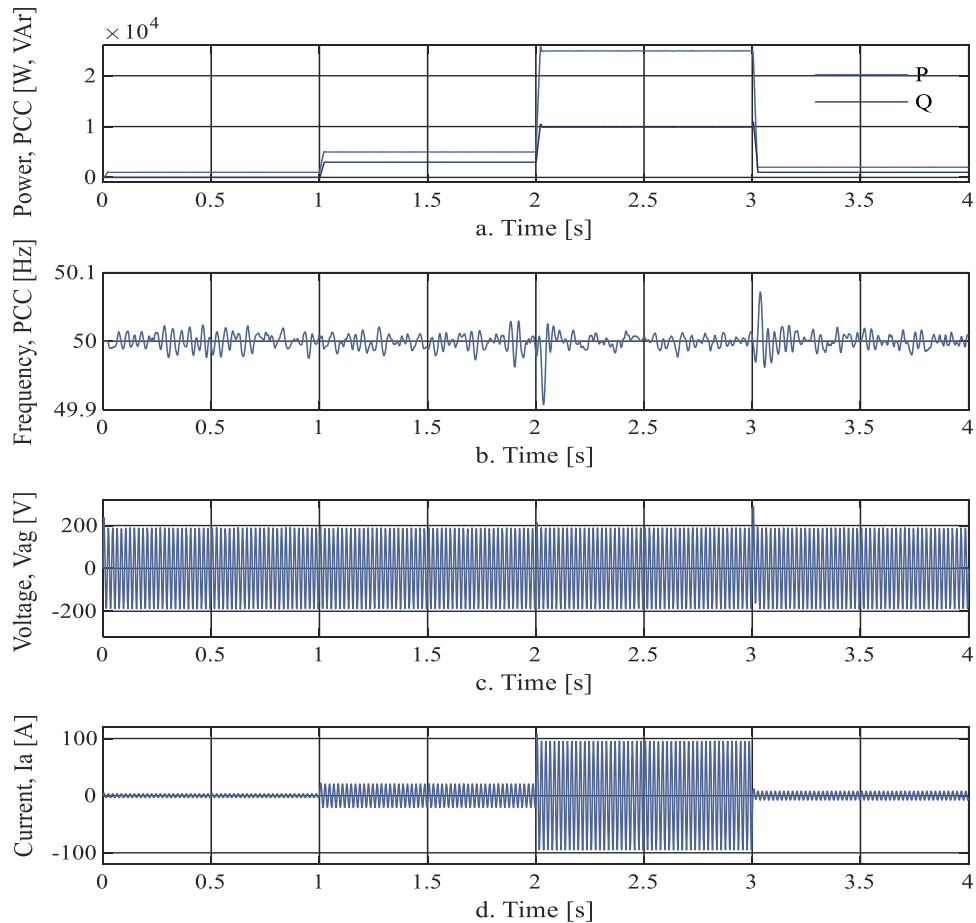


Figure 4.3. Islanded mode: a. Power at PCC, b. Frequency at PCC, c. Voltage at PCC, d. Current at PCC

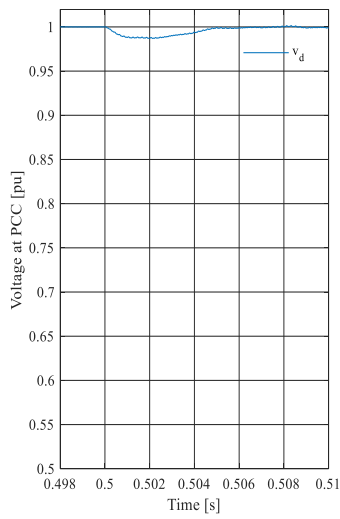
4.3.4 Transient Response to Islanding

An important aspect of the BESS is to provide continuously power if the utility grid is disconnected, either because of a fault or intentionally. For the proposed model this implies that the BESS switches from power control to voltage control, and from utilizing PLL for signal reference to generating an internal reference for the Park transformation. An important factor during islanding of the microgrid is the degree of import or export of power, which can be seen in context with intentional or unintentional islanding [7]. During a planned islanding procedure, the capability of providing power in the microgrid is ensured before disconnection while an unplanned islanding might lead to large deficit or surplus of power.

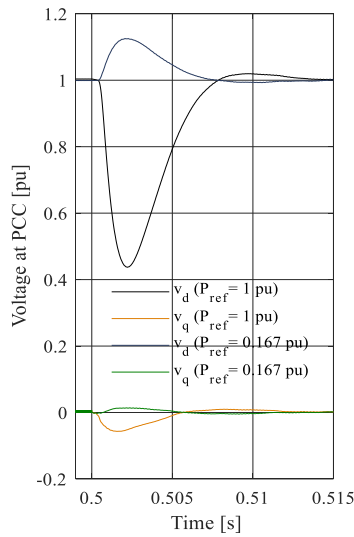
To validate the BESS functioning during islanding, three scenarios are considered according to Table 4.5. For planned islanding, Figure 4.4.a, the voltage change is observed to be rather small as the BESS output power is aligned with the load. The situation is quite different as the BESS is discharging, Figure 4.4.b, or charging, Figure 4.4.c. This causes severe voltage dips depending on the deficit or surplus of energy delivered by the BESS, which can also be found for similar cases [32] [69] [70]. It is emphasized that an increase in v_{dq} does not directly relate to an equal increase in peak voltage in the abc -frame as it depends on the magnitude of V_a, V_b and V_c at moment of islanding.

Table 4.5. Scenarios for Islanding of BESS

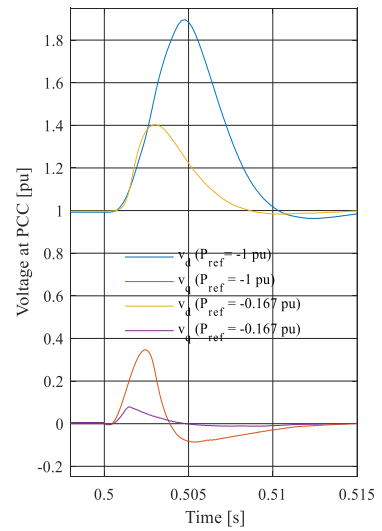
Planned Islanding	Unintentional Islanding while Discharging BESS	Unintentional Islanding while Charging BESS
	BESS Discharging	BESS Charging
$P_{\text{BESS}} = P_{\text{Load}}$	Scenario 1: $P_{\text{BESS}} = 30 \text{ kW (1 p.u.)}$	Scenario 1: $P_{\text{BESS}} = -30 \text{ kW (-1 p.u.)}$
	Scenario 2: $P_{\text{BESS}} = 5 \text{ kW (0.167 p.u.)}$	Scenario 2: $P_{\text{BESS}} = -5 \text{ kW (-0.167 p.u.)}$
* Load constant at $(10 + j6.2) \text{ kVA}$. Reactive power reference set to zero for BESS		



a.



b.



c.

Figure 4.4. Islanding of BESS.

a. Planned Islanding, b. Unintentional Islanding while Discharging, c. Unintentional Islanding while Charging

4.4 Wind Turbine

To validate the wind turbine performance, the electronically coupled turbine is connected to a low impedance grid while input parameters are altered. Through the following sections the turbines operation is firstly tested with varying wind speeds, before the frequency droop control and reactive power control are assessed.

4.4.1 Numerical Parameters

The main numerical parameters for the wind turbine are given in Table 4.6 with full parameter list given in appendix A.5.

Table 4.6. Main Numerical Parameters for the Wind Turbine

Parameter	Abbreviation	Value
Rated Power	P_{nom}	30 kW
Nominal Voltage MSC	V_{nom}	400 V
Nominal Voltage SSC	V_{nom}	400 V
Frequency	F_{nom}	50 Hz
Frequency Droop*	K_{droop}	5
Cut-in Wind Speed	V_{wmin}	3 m/s
Cut-out Wind Speed	V_{Wmax}	25 m/s
Total Inertia Constant	H_{tot}	1.91 s

* Only activated for frequency droop control testing

4.4.2 Response During Change in Windspeed

The expected outcome with varying windspeed is closely linked with the aerodynamics of the wind turbines rotor efficiency. With the rotor blade efficiency, C_p curve, based on the constant speed turbine presented in [3], this implies that the turbine will only operate below nominal speeds at wind speeds between 3-6 m/s. If allowed, the turbine would obtain speeds above the nominal speed as the wind speed is increased. However, a restriction to the maximum speed is implemented to avoid the turbine from operating beyond nominal ratings.

Through a 20 second simulation the wind speed is increased from 6 m/s to 16 m/s, as shown in Figure 4.5.a. From $t=16$ s, a rapidly varying distortion in the wind speed is added to control the systems behavior. Figure 4.5.b gives the resulting rotor speed that shows an initial deviation as the simulation is initiated, but reaches nominal speed after approximately 3 s. Further, the rotor speed is observed to increase slightly as the wind speed starts to increase, but the speed control ensures a deviation less than 0.4 % before the speed is reduced.

From Figure 4.5.b the active power is seen to increase as the wind speed increases until the fixed pitched ensures a reduction of power according to the given C_p curve. This implies that shedding of power is performed for wind speeds above approximately 15 m/s. Figure 4.5.c shows the electrical torque associated with the induction generator throughout the simulation, while Figure 4.5.d gives the DC-link voltage. Overall, the system behavior is considered acceptable for varying wind speeds.

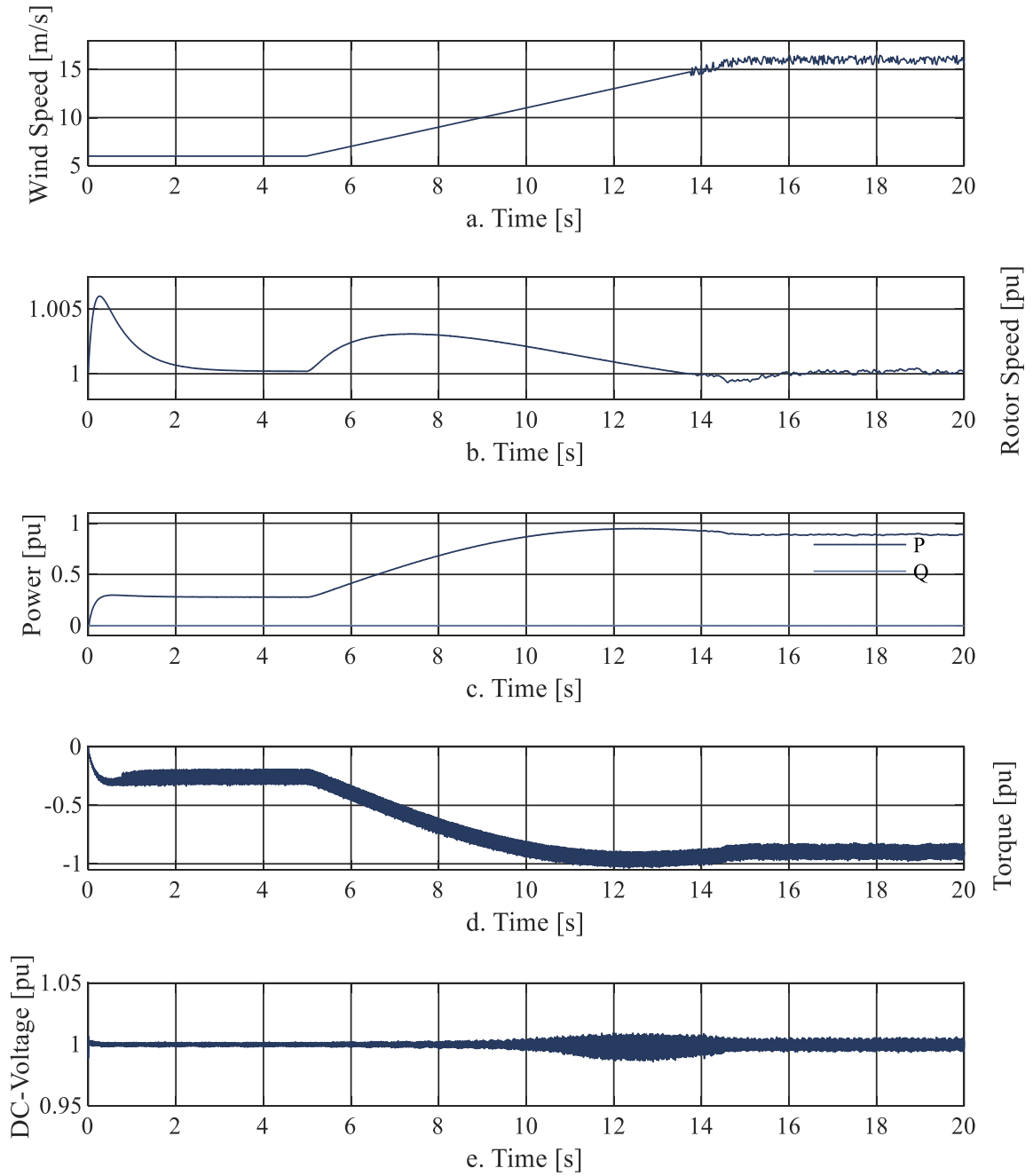


Figure 4.5. WTS Response to Change in Wind Speed

4.4.3 Frequency Droop Controller

The power contribution during frequency deviations is governed by (4.3) when the turbine is operating, and the frequency droop control is activated. By letting $K_{droop} = 5$ and introducing a frequency decrease of 1 Hz at $t = 5 \text{ s}$, with a duration of 500 ms , the resulting response is shown in Figure 4.6.

$$\Delta P_{ref} = K_{droop} * \Delta f \quad (4.3)$$

The results show three important validations:

1. The output power is increased when frequency decreases
2. The rotor speed is reduced
3. The turbine is underproducing after the frequency is stabilized to regain pre-disturbance conditions.

Even though the complexity of this droop controller can be considered rather low, it demonstrates the desired influence on the power output. The effect of including an integrating term is assed in section 5.2.4, "Unintentional Islanding without BESS".

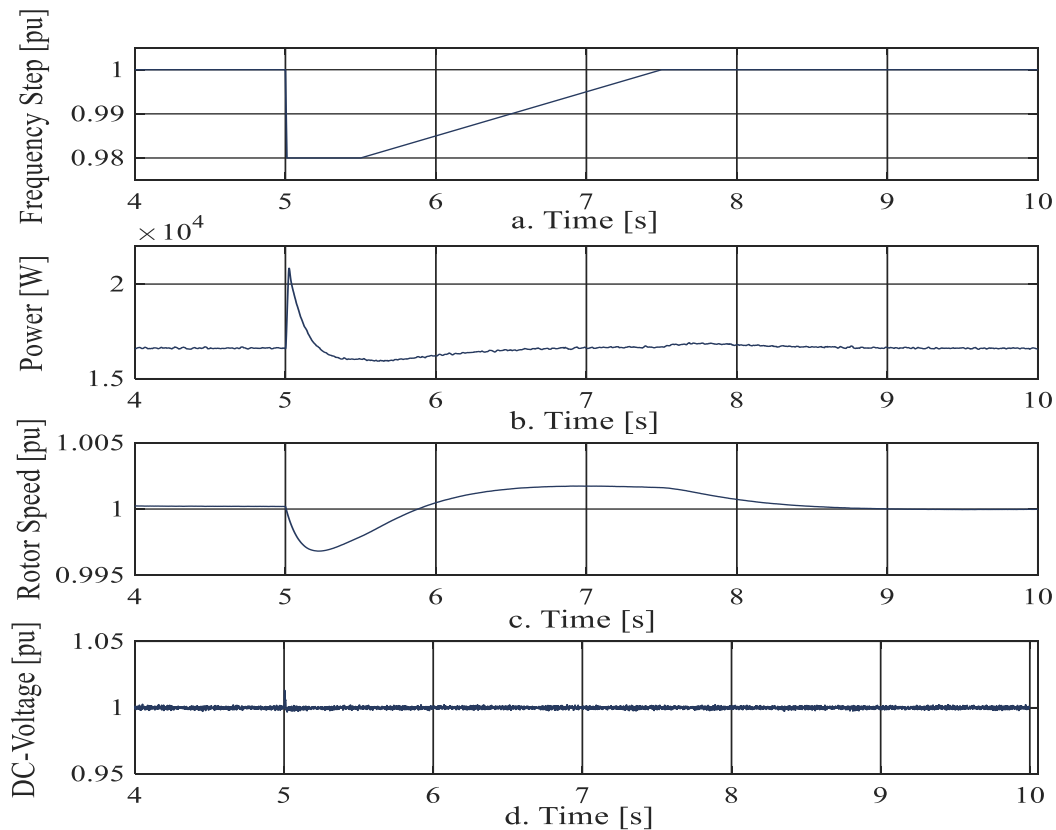


Figure 4.6. Frequency response WTS, $K_{droop} = 5$ (constant wind speed of 8 m/s)

4.4.4 Reactive Power

One of the major advantages with the wind turbine connected through a full power converter is the reduced demand of reactive power from the grid. The reactive power controls objective is to ensure that the wind turbine system produces or consumes the reactive power according to the reference. For the considered scenarios the wind turbine is set to operate at unity power factor, but the ability to produce or consume reactive power is available in the given WT model. In Figure 4.7 the ability to follow the reference and the impact on the DC-voltage is shown. This reveals that the wind turbine system can change the reactive power output from zero to 0.5 p.u. within 20 ms. From the figure it is also notices that an increase in the reference leads to a decrease in reactive power, i.e. delivers reactive power. This is however only dependent on how the system control is defined, where an increased reference leads to production of reactive power.

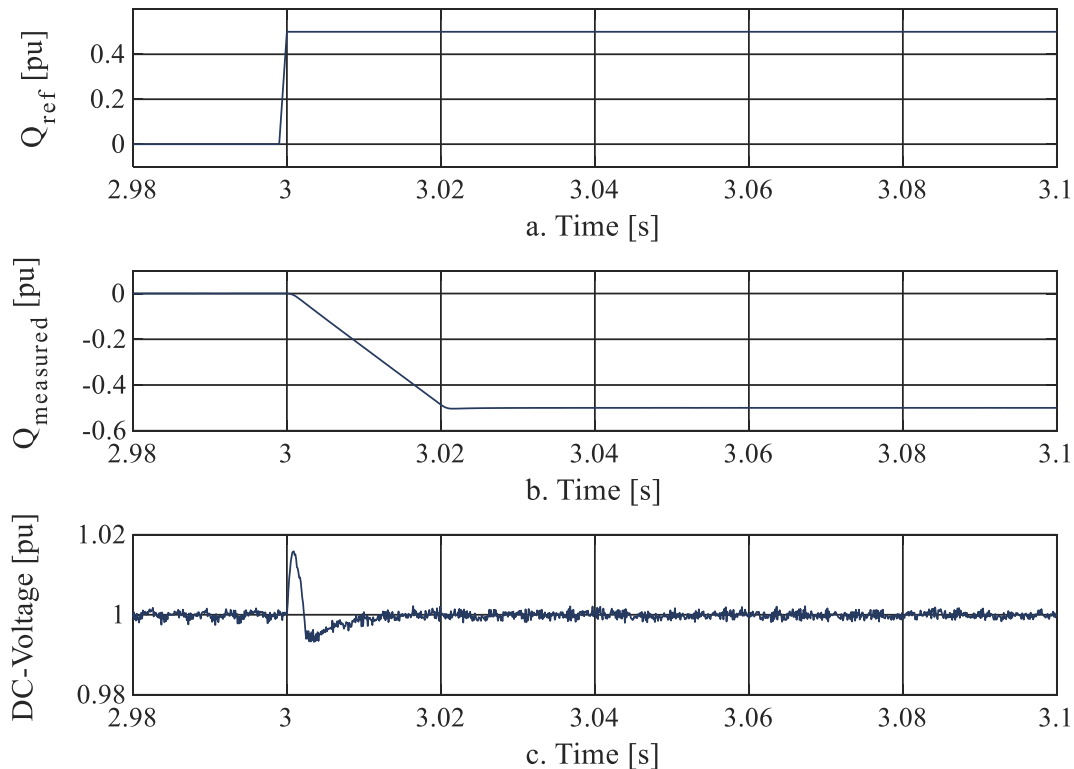


Figure 4.7. Reactive Power Reference Tracking (Constant wind speed of 8 m/s)

4.5 Diesel Generator

Use of diesel generators for power supply is a mature technology that is not considered in detail in this thesis. The diesel generator model consists mainly of pre-defined models with parameters established from manufacturer data. Thus, the aim is to validation a response and behavior that corresponds with literature and expectations. The idea is to have the diesel generator only operating while the BESS SOC level is below the critical threshold, hence the diesel generator is only operative in islanded mode.

4.5.1 Numerical Parameters

The main numerical parameters for model validation are given in Table 4.7, while a full parameter list is provided in appendix A.6.

Table 4.7. Main Numerical Parameters Diesel Generator

Parameter	Abbreviation	Value
Power	S_n	15 kVA
Voltage	S_n	400 V
Frequency	S_n	50 Hz
Generator Inertia	J_{SM}	0.19 kgm ²
Combustion Engine Inertia	J_{DGR}	0.24 kgm ²
Pole Pairs	p	2

Specifications from ABB data sheet [71]

4.5.2 Islanded Operation

During islanded mode the diesel generator must provide voltage and frequency regulation as the consumption changes. To validate the performance a series of loads are connected and disconnected in accordance to Table 4.8. The resulting voltage, frequency and rotor speed can be seen in Figure 4.8.

Table 4.8. Load Intervals During Islanded Operation, DGR.

Time	Load [kVA]
$t \leq 5 \text{ s}$	$(5+j1)$
$t > 5 \text{ s}$	$(10 + j5)$
$8 \text{ s} < t < 11 \text{ s}$	$(7 + j1)$
$11 \text{ s} < t < 14 \text{ s}$	$(7 - j1)$

From the results it is observed that the generator speed, frequency and voltage follow the loading conditions as expected. A small transient behavior is seen in the power as a response to the load changes. This is strongly correlated with the change in both speed of the generator and frequency of the system. Even though the load changes are instantaneously and rather large compared to the generator rating, the system frequency and rotational speed is recovered within one second for the simulated cases. The largest frequency deviation is observed to be $|\Delta f| = 3.2 \text{ Hz}$ at $t = 5 \text{ s}$. In the same period, the rotational speed is reduced to 0.93 p.u. While the terminal voltage V_t remains around 1 p.u., the applied field voltage V_f varies to provide the outputted power. The field voltage is normalized such that 1 p.u. gives 1 p.u stator voltage at no-load.

With the current parameters for the drive train, the difference between combustion engine- and generator speed is around 1 % during under transient conditions. This suggest that a two-mass model might be unnecessary for the given application, with the given drive train specifications.

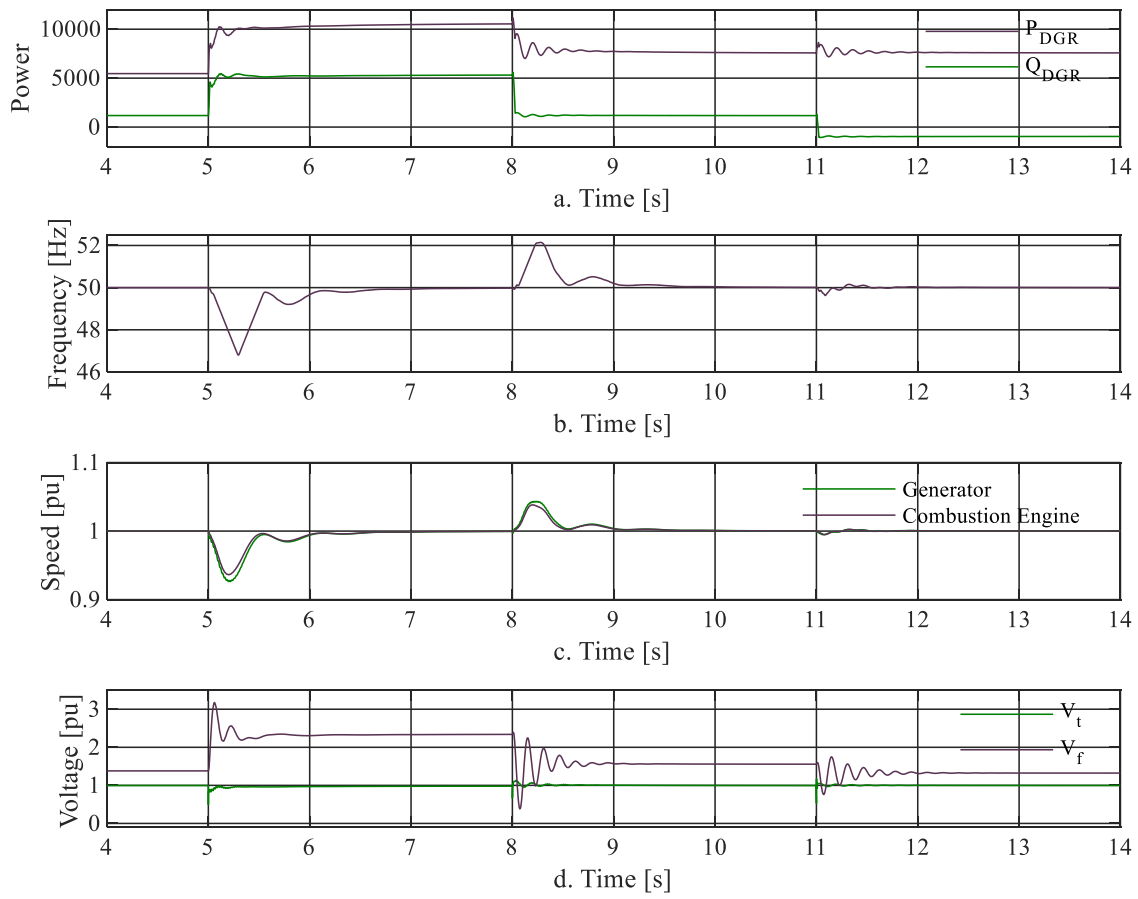


Figure 4.8. Isolated Operation Diesel Generator.
a. Active- and Reactive Power, b. Frequency, c. Generator- and Engine Speed, d. Terminal- and Field Voltage

5 Cases and Results

This chapter presents main findings from critical scenarios where the microgrid transitions from grid-connected to islanded operation. Each case is introduced before main findings are presented and commented briefly. The next chapter will further discuss the validity and impact of the results.

5.1 Case Study Introduction

The purpose of the following case simulations is to assess the microgrid behavior and stability during critical scenarios. With a focus on the transition from grid-connected operation to islanded operation, the following cases has been assessed:

- Case 1 – Intentional Islanding
- Case 2 – Unintentional Islanding with BESS
- Case 3 – Unintentional Islanding with Detection Time Delay
- Case 4 – Unintentional Islanding without BESS
- Case 5 – Black Start Capability

Despite that a fully autonomous control is not directly implemented, the control strategy presented in section 3.2 has been followed. Further, all simulations presented in this chapter has been executed with simulation steps and control sampling times according to appendix A.1. At last it is highlighted that the following results has been obtained with the modelled control and components as presented in chapter 3.

5.2 Transient Response to Islanding

An important aspect of the autonomous system is to provide a continuous power balance if the utility grid is disconnected, either because of a fault or intentionally. The term islanding is according to the IEEE std. 1547 defined as [15] :

A condition in which a portion of an area EPS (electric power system) is energized solely by one or more local EPSs through the associated PCCs while that portion of the area EPS is electrically separated from the rest of the area EPS.

The standard further separates, as in this thesis, between intentional- and unintentional islanding with the intentional being a planned action while the unintentional is an unplanned action [15].

For the proposed model this implies that the BESS switches from power control to voltage and frequency control, and from utilizing PLL for signal reference to generating an internal reference for the Park transformation when the mode command of an islanding situation is received.

An important factor during islanding of the microgrid is the degree of import or export of power during at disconnection of the grid [7]. The degree of import or export of power can be seen in context with intentional and unintentional islanding of the microgrid. During a planned islanding procedure, the power mismatch between generation and consumption within the microgrid is minimized before disconnection, while the unintentional islanding could imply severe power mismatches.

5.2.1 Intentional Islanding

Intentional islanding⁶ is the transition from grid-connected operation to islanded operation after a request to perform the transition. This implies that the microgrid control has time to balance the load and generation pre-islanding. In IEEE Std. 2030.7-2017 the procedure is set to adjust active- and reactive power such that the exchange at PCC is zero, then adjust the controllers and protection devices before the island is created [72]. This strategy is adopted for the following scenario.

The power reference signals of the BESS are adjusted according to (5.1) and (5.2). This reduces the amount of import, or export, to a minimum, hence reducing the transient response at islanding. However, if the rated WT and PV power rating exceeds the BESS capability the WT or PV power output must be reduced before islanding, unless a dump load is present.

$$P_{\text{BESS,ref}} = P_{\text{WT}} + P_{\text{PV}} - P_{\text{Load}} \quad (5.1)$$

$$Q_{\text{BESS,ref}} = Q_{\text{WT}} + Q_{\text{PV}} - Q_{\text{Load}} \quad (5.2)$$

During simulation the PV- and WT-system is configured to operate at unity power factor throughout. One assumption provided for the simulations is that the BESS switches from PQ- to V/f-control simultaneously as the disconnection is performed.

The simulation has been carried out with the parameters listed in Table 5.1. As the subject is to have a planned islanding, the consumption and production conditions pre-islanding does not have a profound influence on the transient behavior, provided that the BESS can ensure system balance before islanding, i.e. export/import within range of BESS power rating.

⁶ Also referred to as planned islanding in literature [74]

Table 5.1. Main Parameters for Planned Islanding Scenarios

Scenario	BESS	WT	PV	Load
1. Intentional Islanding	PQ-Control until islanding mode command signal received. Changes to V/f-control in islanded mode.	Wind Speed:8 m/s P = 16.5 kW Q = 0 kW K _{droop} = 0	Irradiance: 500 W/m ² Cell temperature: 25°C P = 15.4 kW Q = 0 kW	Total Load*: 24,75 kW + j 8.13 kVAr Dispersed according to appendix B.

* at 230 V reference

The loading conditions are dispersed to the various loads in accordance to the findings in [3]. The total load is rather high compared to the consumption found in [3] and could therefore be interpreted as a high load situation. For the wind turbine the wind speed is set to 8 m/s which is slightly above the yearly average wind, while the PV system is set to an irradiance of 500 W/m² and a cell temperature of 25 °C.

Figure 5.1 gives the resulting active- and reactive power associated with the PV, WT, BESS, grid and load. From Figure 5.1.a and Figure 5.1.b it is observed how the BESS reduces the systems export to a minimum before islanding the system at $t = 3$ s. The process of reducing the microgrid export is set to take approximately one second, from $t = 2$ s. Further, the production from the wind turbine is around 16.5 kW while the PV is producing around 15.3 kW, both at unity power factor. The load, including transmission, is consuming approximately 23.4 kW and 7.52 kVAr before islanding. After disconnection, the BESSs active- and reactive power is adjusted with approximately -0.4 kW and -0.6 kVAr to balance the generation and consumption. Further, no large deviations are observed for the PV, WT, BESS or load at moment of islanding.

In Figure 5.2 the microgrids frequency and RMS phase to ground voltage are shown throughout the transition. Figure 5.3.a present the DC-voltages for the WT, PV and BESS, and Figure 5.3.b the WTs generator speed. Throughout the transition from grid-connected to islanded mode, the frequency, RMS voltage, DC-voltage, and generator speed is remained stable.

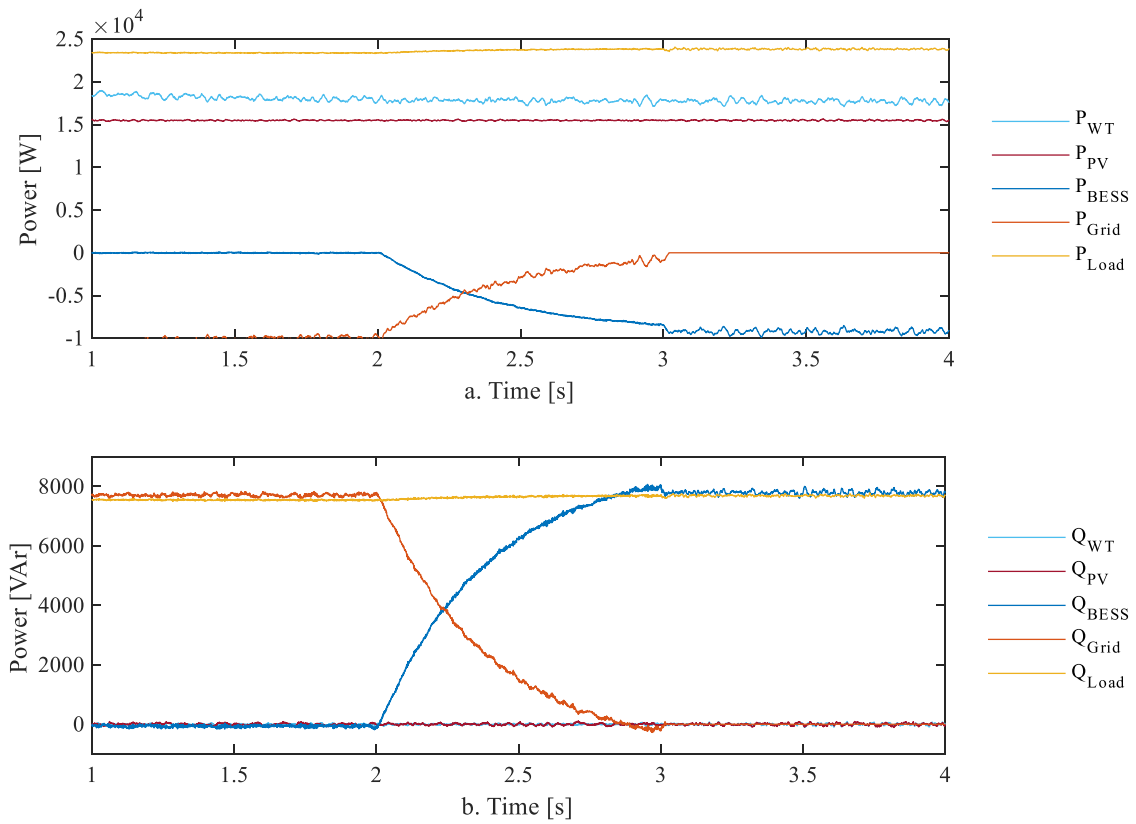


Figure 5.1. Scenario 1, Active- and Reactive Power During Planned Islanding

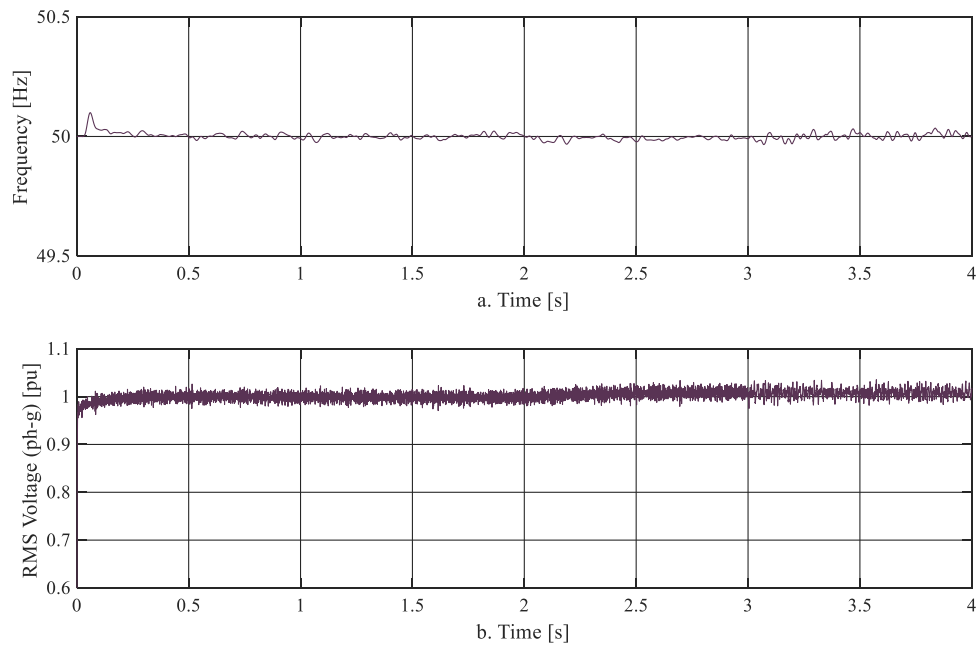


Figure 5.2. Planned Islanding. a. Frequency [Hz], b. RMS Voltage (ph-g) [pu]

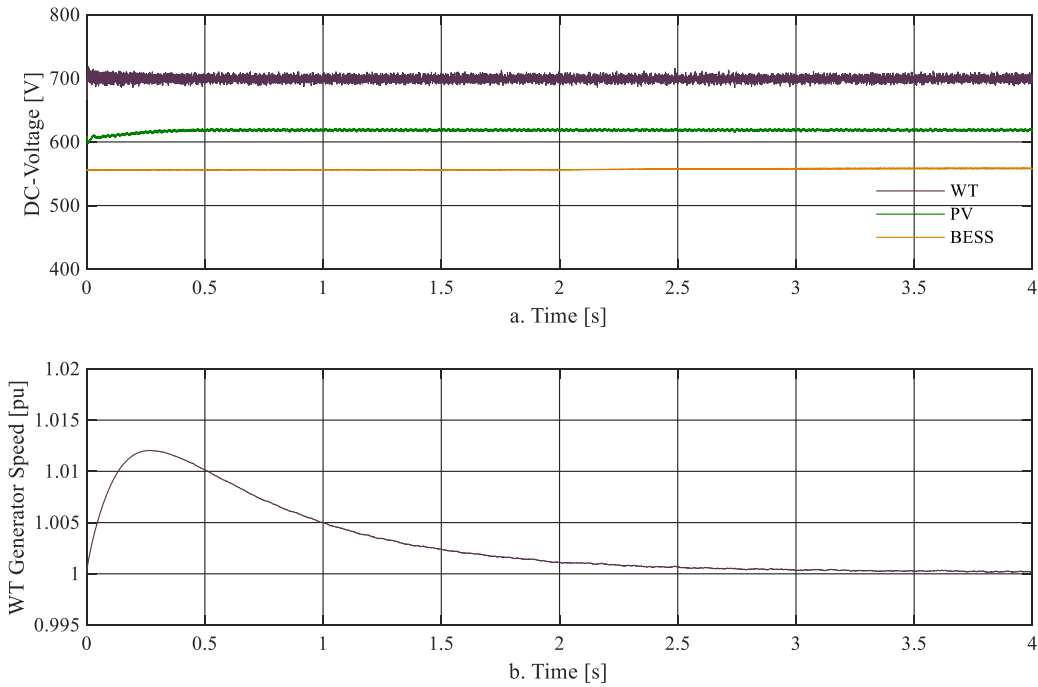


Figure 5.3. Planned Islanding. a. DC-Voltage [V], b. WT Generator Speed [pu]

5.2.2 Unintentional Islanding with BESS

In contrast to the intentional islanding, the unintentional islanding may occur at any time. There is no guaranty that the power export, or import, is low during these situations. Hence the microgrid system might experience under- or overproduction during the transition to an islanded microgrid. This implies that there are two main situations for unintentional islanding:

1. The BESS capability can handle the over- or underproduction within the microgrid
2. The BESS capability cannot handle the over- or underproduction within the microgrid

With the first situation, the BESS should be able to counteract the power imbalance in the system. For the second situation a dump load is necessary if there is overproduction, and extra generation, or a load shedding scheme, necessary if there is underproduction. To restrict the scope of this section, only the first situation is assessed.

In Table 5.2, the series of configurations simulated are shown. These are set to include low and high export, and import, at islanding. It is assumed an ideal situation where the island detection works instantaneously. This assumption is later discussed in section 6.3.1. To simulate the loss of connection an ideal breaker immediately disconnects all three phases at $t = 3$ s and separates the microgrid from the distribution grid at PCC.

Table 5.2. Scenarios for Unintentional Islanding

Scenario	WT	PV	BESS	Load*	Export at Islanding**
2. Low Export	Wind speed: 5 m/s P = 7.8 kW Q = 0 kW	Solar Irradiance: 800 W/m ² Cell Temperature: 25°C P = 24 kW Q = 0 kW	P = -8.8 kW Q = 7 kW	Total Load: P = 16.5 kW Q = 5.4 kVAr	$\Delta P = 6.5$ kW $\Delta Q = 2.6$ kVAr
3. High Export	Wind speed: 10 m/s P = 24 kW Q = 0 kW	Solar Irradiance: 500 W/m ² Cell Temperature: 25°C P = 15.4 kW Q = 0 kW	P = 0 kW Q = 0 kW	Total Load: P = 16.5 kW Q = 5.4 kVAr	$\Delta P = 22.5$ kW $\Delta Q = -5.4$ kVAr
4. Low Import	Wind speed: 6 m/s P = 9.5 kW Q = 0 kW	Not Applied	P = 0 kW Q = 0 kW	Total Load: P = 16.5 kW Q = 5.4 kVAr	$\Delta P = -7$ kW $\Delta Q = -5.4$ kVAr
5. High Import	Not Applied	Not Applied	P = 0 kW Q = 0 kW	Total Load: P = 16.5 kW Q = 5.4 kVAr	$\Delta P = -16.5$ kW $\Delta Q = -5.4$ kW
* Loading dispersed according to appendix B.					
** Export defined as: grid delivers active- and reactive power if negative					

5.2.2.1 Low Export

The term *low export* is not precise, but as pointed out in Table 5.2, this corresponded to an export of 6.5 kW and 2.6 kVAr when the microgrid was islanded. Figure 5.4 shows the resulting frequency, and active- and reactive power for the BESS and grid when the microgrid was disconnected at $t = 3$ s. From the simulations it was observed a lower frequency of 49.93 Hz as the BESS overcompensates the consumption. This is however regulated quickly, and the frequency is 50 Hz \pm 0.1 % again after 30-50 ms. The BESS fast response ensures a stable transition to islanded operation.

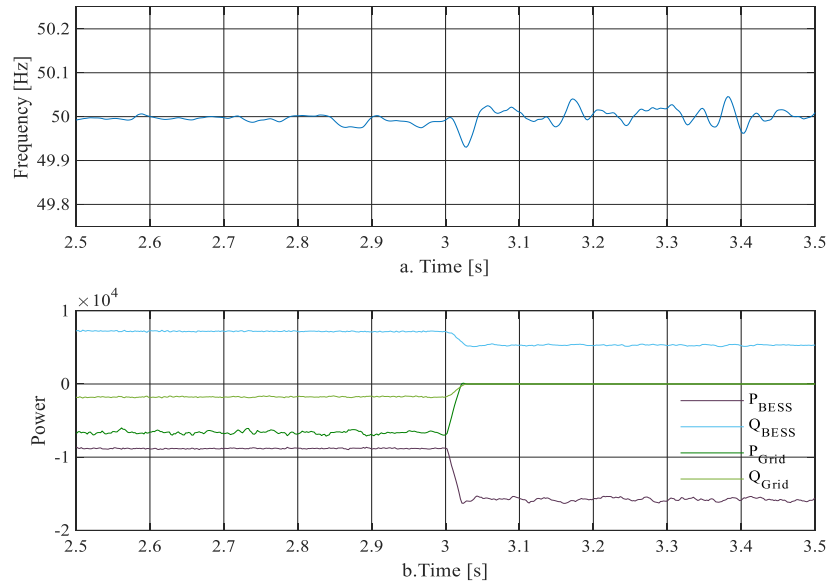


Figure 5.4. Scenario 2, Low Export and Unintentional Islanding at $t = 3$ s

5.2.2.2 High Export

In scenario 3, *High Export*, the production exceeds the consumption by 22.5 kW while consuming 5.4 kVAr. When the grid is disconnected this implies that the BESS must absorb the overproduction to keep the frequency and voltage around their nominal values. From Figure 5.5.a it is seen that the frequency is reduced to 49.82 Hz when disconnected from the grid. After the initial response the system frequency is restored around the nominal value after approximately 100 ms.

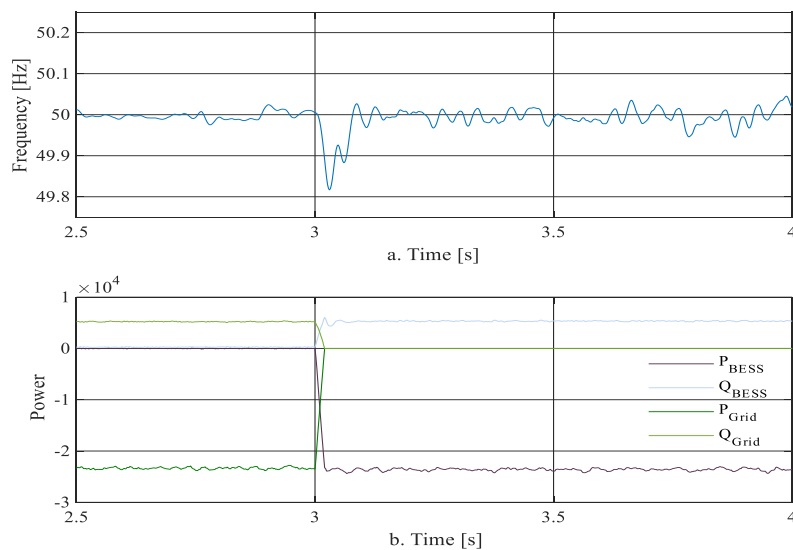


Figure 5.5. Scenario 3, High Export and Unintentional Islanding at $t = 3$ s

5.2.2.3 Low Import

In the case of *Low Import*, the PV system is not applied while the wind speed is set to 6 m/s. The BESS is online but not producing or consuming power except for the compensation of the capacitor bank. This might be one of the most common situations experienced for the microgrid area as this is a likely situation after sunset with a windspeed close to the average of 7.2 m/s [3]. As for the previous cases with zero delay, the fast response of the BESS ensures a frequency around 50 Hz, as seen in Figure 5.6.

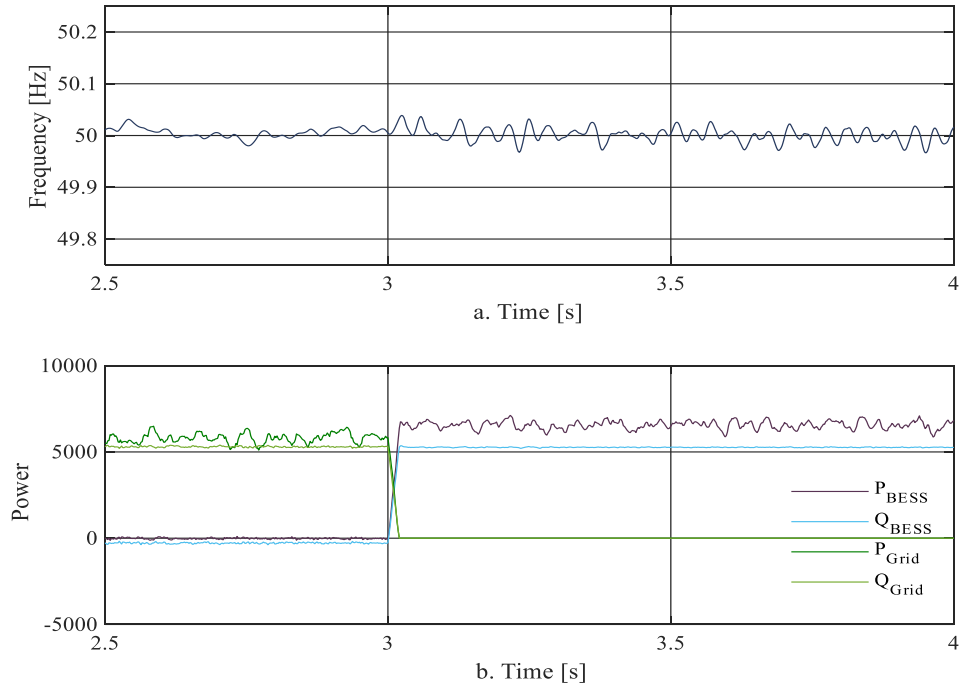


Figure 5.6. Scenario 4, Low Import and Unintentional Islanding at $t = 3$ s

5.2.2.4 High Import

The *High Import* scenario is a special case where the consumption is fully provided by the grid, i.e. the only difference from before establishing a microgrid is the active BESS. At disconnection from the grid the BESS switches instantaneously from PQ-control to V/f-control and must deliver the full load of 16.5 kW and 5.4 kVAr. Figure 5.7 shows that the change from grid connected to islanded is handled without larger frequency deviation than $\Delta f = 0.16$ Hz, as the BESS active power production has a slight overshoot before settling. The disconnection of the WT and PV system pre-islanding also reduced the harmonics in the voltage, such that the frequency measured is seen to be somewhat smoother pre-islanding. The results further imply an increased reliability for the area if the impact of ideality, with regards to neglecting time delay, is disregarded.

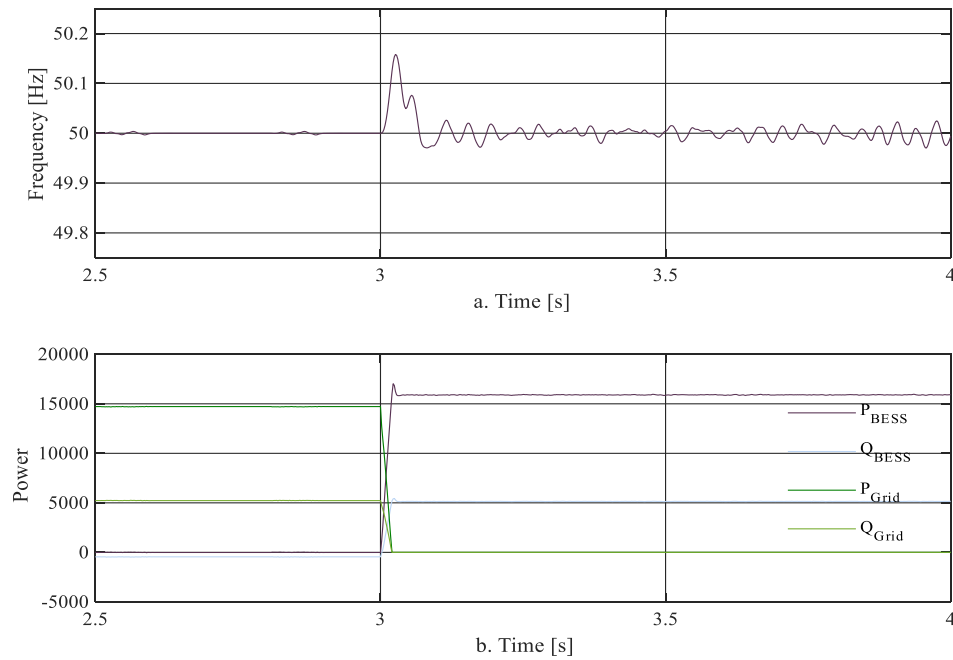


Figure 5.7. Scenario 5, High Import and Unintentional Islanding at $t = 3$ s

5.2.3 Unintentional Islanding with Detection Time Delay

The results presented in scenarios 2-5 gives an insight to an ideal situation where the mode command to the BESS is provided instantaneously as the grid is disconnected. However, in practice there will be a time delay from the grid connection is lost until the BESS switches mode. This time delay is highly dependent on the island detection method used. For the proposed methods a detection time varying from 4 ms to 2 s is anticipated, depending on the method and the state of the microgrid at disconnection [34].

In the following simulations the *High Export* scenario is considered, see Table 5.2. In this scenario, the microgrid exports 22 kW and imports 5.4 kVar. Without the delay, the BESSs fast response can restore balance between generation and consumption such that only small deviations in power quality is observed. By implementing the detection time delay this means that all the microgrid generation units operates at PQ-control. Table 5.3, gives the considered time delays between disconnection and received mode command for the BESS. No droop control is implemented for these simulations and the internal reference oscillator is aligned with the measured PLL signal at activation of V/f-control.

Table 5.3. Time Delay, Unintentional Islanding

Time Delay
$t_{delay} = 10 \text{ ms}$
$t_{delay} = 50 \text{ ms}$
$t_{delay} = 100 \text{ ms}$

Figure 5.8 shows the respective frequencies and RMS voltages measured, when the distribution grid is disconnected at $t = 3 \text{ s}$. From the results both the frequency and voltage are seen to increase as a consequence of the power mismatch within the microgrid. With the loads being modelled as RLC-loads the heightened voltage causes an increased power consumption according to $S = \frac{U_n^2}{Z_{load}}$ during the transition. An increase of 75 % is observed for the RMS voltage, which implies that the voltages are beyond the nominal operating voltage of most household equipment, leading to risk of both damaged equipment and can poses a safety hazard. Thus, protection schemes are vital.

With delays over 100 ms, the frequency deviation exceeds 5 Hz. At this rate of change, the island detection method should have detected the situation, or the microgrid could have tripped by under-frequency or over-voltage protection. This is also correspondent to the findings in [34], where large power mismatches normally lead to quicker detection times.

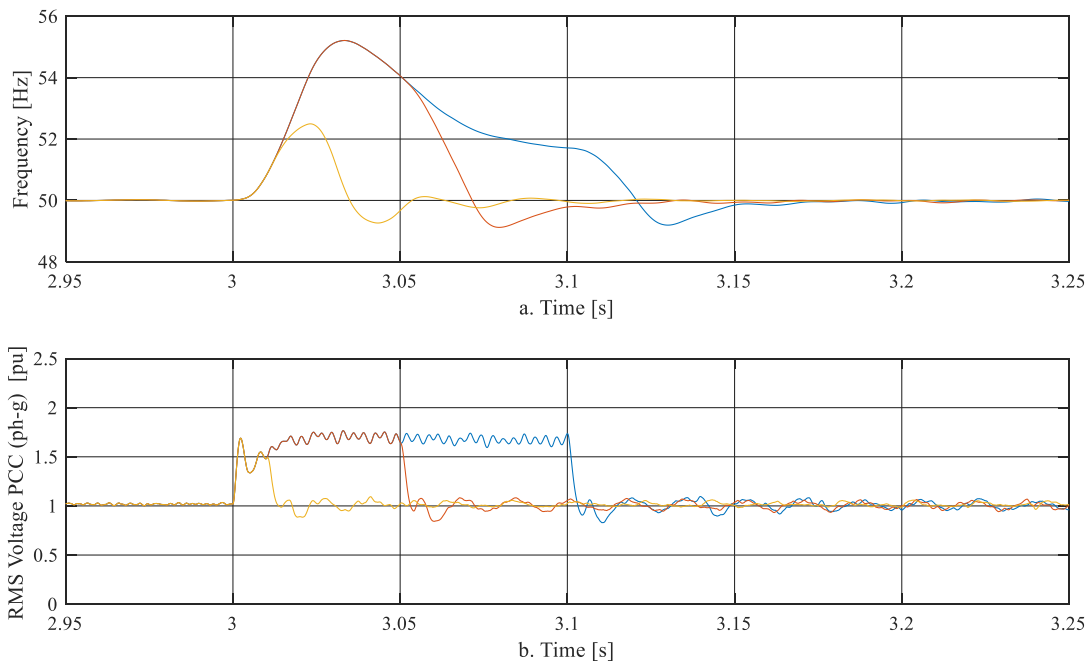


Figure 5.8. Unintentional Islanding with Delayed Mode Command. Islanding at $t = 2\text{s}$ with 22 kW export and 5.4 kVAr import.

a. Frequency, b. RMS voltage at PCC (ph-g)

5.2.4 Unintentional Islanding without BESS

In the case of an unintentional islanding during import of power without the BESS available, two alternative operations can be considered:

1. Disable the production units and perform a black start with the diesel generator
2. Balance generation and consumption without the use of the BESS

The first option would mean that the microgrid is deenergized until the diesel generators are available to perform a black start of the system. This is further assessed in section 5.3.2, "Black Start with Diesel Generator". The second option implies that the microgrid can remain operating during the transition.

In this section the microgrid is considered to import power from the grid at transition. Without the BESS capability of providing voltage and frequency support, loads must be curtailed, or the PV or WT system must alter their power output to match the consumption. To demonstrate the concept, two control actions take place. Firstly, the use of WT frequency droop control to reduce the frequency deviation, and secondly the use of load shedding to equal production and consumption. The activation of load shedding measures is assumed to take one second from islanding is detected.

Even though the simple droop controller assumes a predominantly inductive grid, the concept should provide some information on how the WT control system can be used to remain stable through a transition from grid-connected operation to islanded operation. But without the BESS activated, there is no integrator in the control system to restore the frequency to 50 Hz. Therefore, a third option is included where the WT droop controller is provided with an integrator term, enabled through an PI-controller. It is emphasized that this control should only be active if the microgrid is islanded, and that the BESS is not operating in voltage control, to avoid fluctuations in WT power and thus WT generator speed.

The PV system cannot increase its power production as it is already operating at MPP and has no inertia available. Hence the PV system can only contribute with reactive power compensation in this situation. It is therefore set to deliver the reactive power drawn from the load. No autonomous control is implemented for this, only an alteration of the reactive power reference in the PV control system.

Three scenarios were simulated for the given situation. First, a scenario with only the simple WT droop control enabled. Secondly, a scenario with both the droop control enabled and load shedding. And lastly, the improved droop control with integrator term. The sequences of these scenarios are given in Table 5.4, while Table 5.5 gives the production and consumption at islanding.

Table 5.4. Sequence of Actions for Islanding without BESS

Time	Only WT Droop Control	Load Shedding and WT Droop Control	WT Droop Control with Integrator Term
$t = 3 \text{ s}$	Microgrid Islanded	Microgrid Islanded	Microgrid Islanded
$t = 4 \text{ s}$	-	1 kW Load Shedding	-
$t = 5 \text{ s}$	-	0.5 kW Load Shedding	-
$t = 6 \text{ s}$	Reconnected to Grid	Reconnected to Grid	Reconnected to Grid

Table 5.5. Production and Consumption at Islanding without BESS

WT	PV	BESS	Load	Import at Islanding**
Wind speed: 7.5 m/s P = 7.8 kW Q = 0 kW $P_{\text{Droop}} = 5$ $I_{\text{Droop}} = 5$	Solar Irradiance: 350 W/m ² Cell Temperature: 25°C P = 15 kW Q = 6 kVAr	Not Applied	Total Load*: P = 28.2 kW Q = 6.0 kVAr	$\Delta P = 2 \text{ kW}$ $\Delta Q = 0 \text{ kVAr}$

* At 230 V reference. Dispersed according to appendix B.

** Import defined as: Grid delivers active- and reactive power if positive

The resulting frequency, RMS voltage and WT generator speed are shown in Figure 5.9 for the three given scenarios. From the frequency measurements it is clearly favorable to include an integrator term in the WT droop control, with this being the only option that restores the frequency for the given situation. With only the simple droop control, the frequency falls until the grid is reconnected at $t = 6 \text{ s}$. Whereas for the scenario with load shedding, the frequency is stabilized around 49.3 Hz.

An interesting observation is the generator speed in Figure 5.9.c. As the WT is operating at MPP when the grid is disconnected, the increased delivery of power is provided by the stored inertia in the rotating mass. Again, the WT droop control with an integrator term is favorable as this only leads to a 5.1 % reduction in generator speed before the grid is reconnected. However, it is observed that the load shedding has a positive effect on the simple proportional gain droop controller.

At last, the RMS phase to ground voltage is seen in Figure 5.9.b. With only the PV and WT operating there is unfortunately an increased share of harmonics in the voltage. This should however be possible to reduce by a closer inspection on the control- and filter design. An increase in RMS voltage of approximately 5 % during the islanded period is considered acceptable.

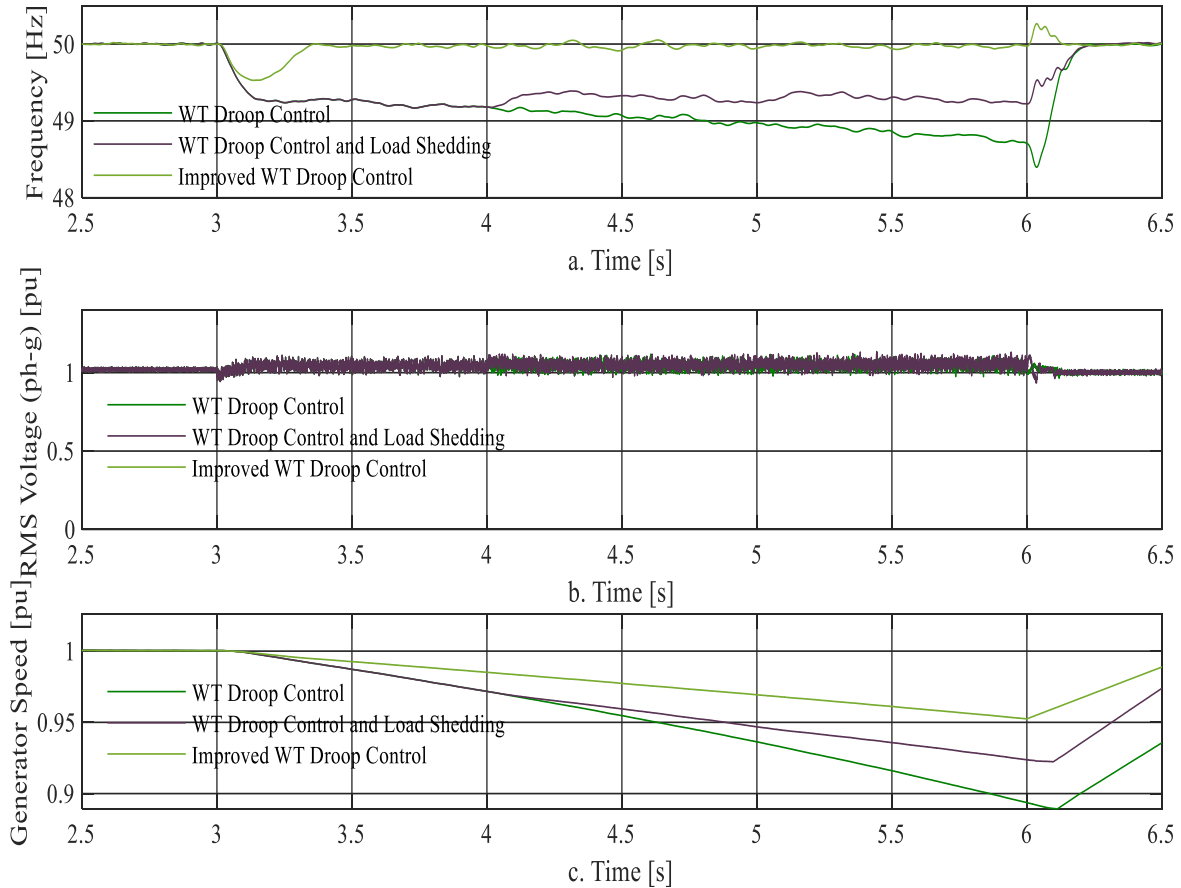


Figure 5.9. Islanding without BESS. a. Frequency [Hz], b. RMS Voltage (ph-g) [pu], c. WT Generator Speed [pu]

5.3 Black Start Capability

A blackout of the microgrid could arise from an unstable transition from grid-connected mode to islanded mode, an internal fault or large disturbances in the main grid. Protection schemes are planned to deenergize the microgrid in cases where further operation could cause harm to residents, property or DG units. To reduce the interruption time and increase the reliability of power supply, a black start capability is essential [73]. A black start implies that the microgrid can recover the nominal voltage and frequency from a deenergized system. For the

proposed microgrid, the BESS or the diesel generator must be able to provide such services to enhance the reliability.

In [73], a serial restoration strategy is implemented. In short, the procedure is to disconnect all the loads before establishing nominal voltage and frequency by letting one of the microgrid power sources operate at V/f-control. After ensuring that the power demand can be met, the loads are reconnected. The last step is to connect the PQ-controlled distributed generation, provided that the power balance is remained in the microgrid [73]. This strategy is adopted for the following scenarios.

5.3.1 Black Start with BESS

The existing structure of the proposed microgrid gives some challenges with a stepwise reconnection of the load without introducing changes to the existing grid structure. This is further discussed in section 6.4. Therefore, in the simulations performed it is assumed one controllable breaker between the main busbar and the connected loads. This implies that the full load is reconnected at once. Following the loads, the PV system is reconnected, before the wind turbine is connected at last. The reconnection of the WT and PV system is only performed if (5.3) and (5.4) is fulfilled. In Table 5.6, the black start procedure is presented for the simulated case.

$$P_{PV} + P_{WT} + P_{BESS,min} \leq \sum P_{Load} \quad (5.3)$$

$$Q_{PV} + Q_{WT} + Q_{BESS,min} \leq \sum Q_{Load} \quad (5.4)$$

Table 5.6. Black Start Procedure BESS

Time	Action
t = 0	BESS Activated with V/f – Control
t = 20 ms	Loads Connected*: P = 16.5 kW Q = 5.4 kVAr
t = 500 ms	PV System Connected. Solar Irradiance: 500 W/m ² Cell Temperature: 25°C P = 15 kW Q = 0 kW
t = 1000 ms	WT System Connected. Wind speed: 7 m/s P = 19 kW Q = 0 kW

* at 230 V reference, dispersed according to appendix B.

Figure 5.10 presents the resulting frequency and RMS voltage at PCC for the black start with the BESS. A black start procedure with the BESS has a very small impact on both frequency and voltage because of the rapid response. The initial frequency in the measurement block is set to 50 Hz, explaining why the frequency does not initiate at zero Hertz. Figure 5.11 shows the BESS active- and reactive power throughout the simulation. It is evident that the BESS response to changes is fast, which leads to small frequency and voltage deviations during a black start. The transient response to the PV connecting is larger than for the WT since the PV produces close to the MPP instantaneously. For both the PV and WT a ramped increase in power can be implemented by a more extensive control, implying a further reduced transient condition.

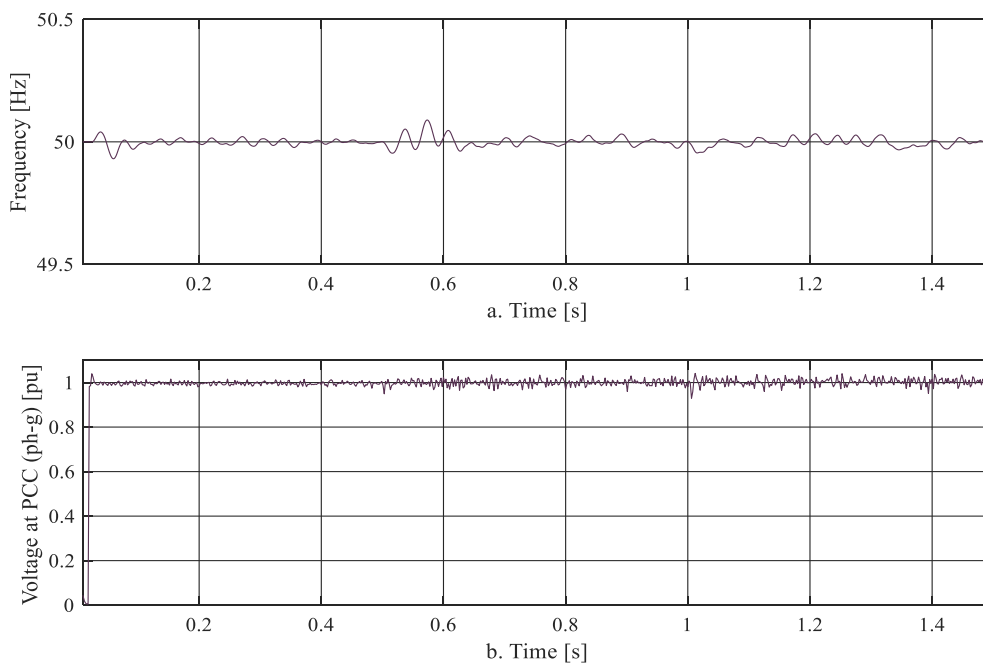


Figure 5.10. Black Start. a. Frequency [Hz], b. RMS Voltage at PCC (ph-g) [pu]

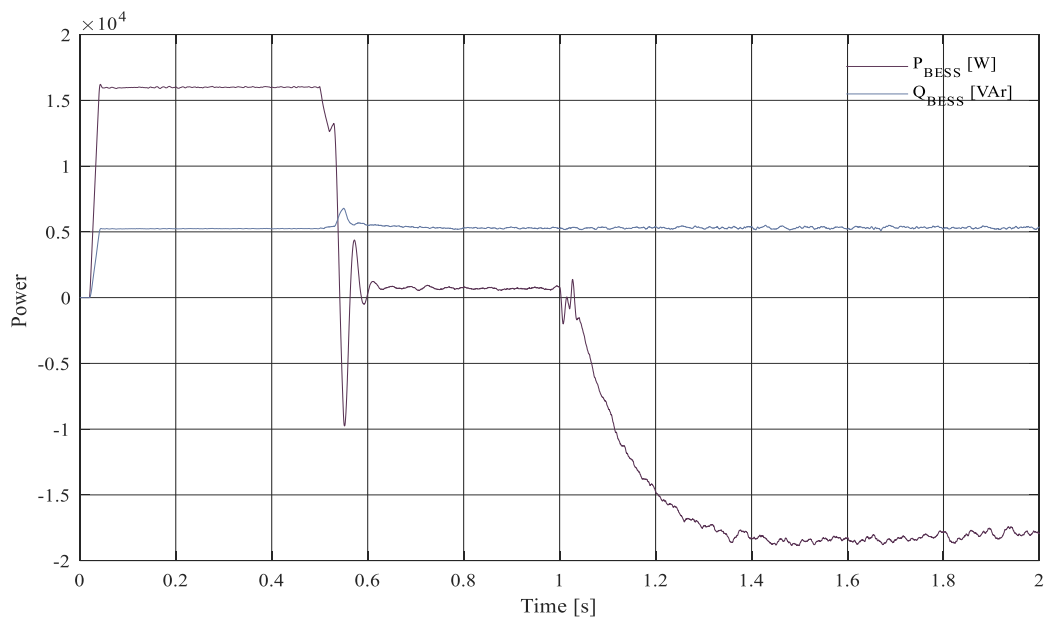


Figure 5.11. BESS Active- and Reactive Power During Black Start

In Figure 5.12 the DC-voltages are provided for the PV, WT and BESS during the black start procedure. All the voltages are observed to be rather stable around their nominal values

except for a transient condition when the PV and WT is connected. The largest deviation is observed for the PV system, which corresponds with the fastest ramping of produced power. After the PV is connected, the DC voltage is increased with approximately 20 V because of the reference voltage provided by the MPPT algorithm. For the WT a voltage dip of 10 % is observed before the DC-voltage stabilizes at the nominal value. After $t = 1$ s, the BESS consumes active power, hence the DC-voltage of the battery terminals are heightened. Fast fluctuating DC-voltage for both the BESS, PV and WT can be seen, these are present because of the rapid switching performed by the VSCs and dependent on both the control system and the DC-capacitor dimensioning.

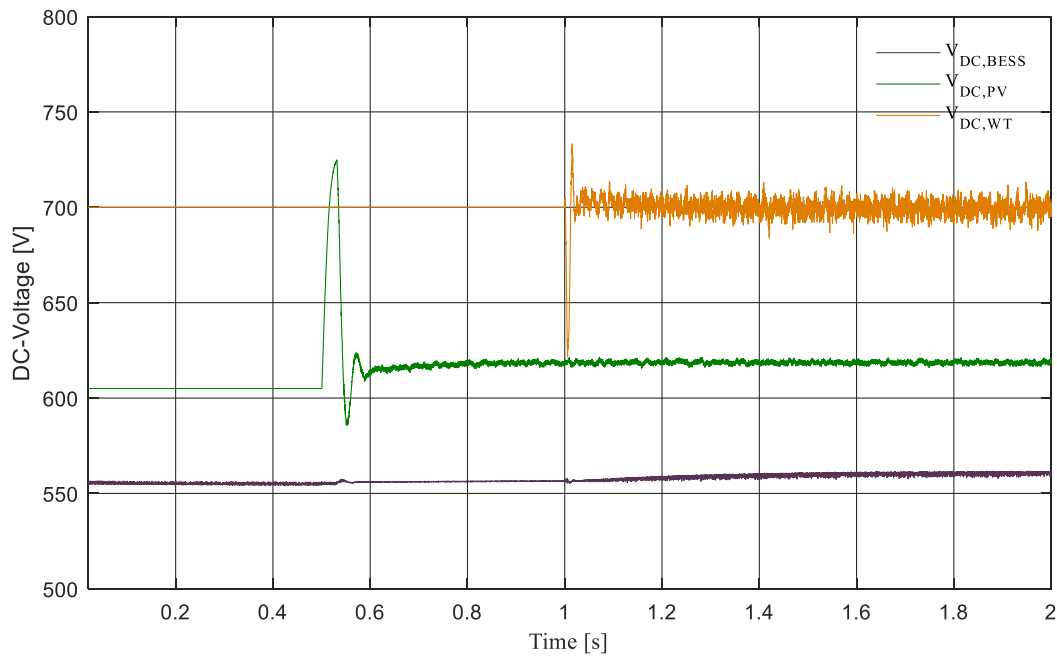


Figure 5.12. DC-voltages During Black Start Procedure with BESS

5.3.2 Black Start with Diesel Generator

If the BESS has reached its lower SOC-limit a black start as presented in the previous section cannot be performed. Instead, the black start can be provided by use of the diesel generator system. As the diesel generator response is slower than the BESS, the time period for the procedure is increased. Another important factor of the diesel generator is the lacking ability to consume active power. Therefore, the power balances given in (5.5) and (5.6) is not fulfilled if the WT is connected for the given scenario in Table 5.7. Thus, only the PV system is connected. Because of limitations in the diesel generator model, the load is directly connected at $t = 0$ s. The load is slightly reduced, compared to the black start with BESS, to prevent running two generators at low load.

$$P_{PV} + P_{WT} + P_{DGR,min} \leq \sum P_{Load} \quad (5.5)$$

$$Q_{PV} + Q_{WT} + Q_{DGR,min} \leq \sum Q_{Load} \quad (5.6)$$

Table 5.7. Black Start Procedure with Diesel Generators

Time	Action
t = 0	Diesel Generators Activated Loads Connected*: P = 11.9 kW Q = 3.9 kVAr
t = 2.5 s	PV System Connected. Solar Irradiance: 300 W/m ² Cell Temperature: 25°C P = 8.8 kW Q = 0 kW

* at 230 V reference, dispersed according to appendix B.

Figure 5.13 shows the resulting frequency and RMS voltage. The initial frequency, for the measuring block, is set to 50 Hz. This changes rapidly as the diesel generator is ramping up with the loads already connected. With a slower response than for the BESS, the frequency deviations are larger. The lowest frequency is observed to be 45.9 Hz at $t = 0.4$ s. The frequency is then restored to the nominal value after approximately 2 seconds. At $t = 2.5$ s the PV system is connected. When the PV system is connected, the DC-voltage is heightened before the PV system delivers the expected power at $t = 2.9$ s. This is noticed in the frequency, which reaches a maximum value of 53.1 Hz at $t = 3.3$ s. At $t = 5$ s the frequency was restored to the nominal value.

The RMS voltage is observed to be 0.02 p.u. below the nominal phase to ground voltage before the PV system was connected. Further, the RMS measurements indicated an enhancement to 1.2 p.u. for the phase to ground voltages as the PV production is increased at $t = 2.9$ s. This voltage is however below 1.05 p.u. after approximately 50 ms. Rapid variations in the RMS voltage measurement, from $t = 2.5$ s, origin from the harmonics generated by the PV system.

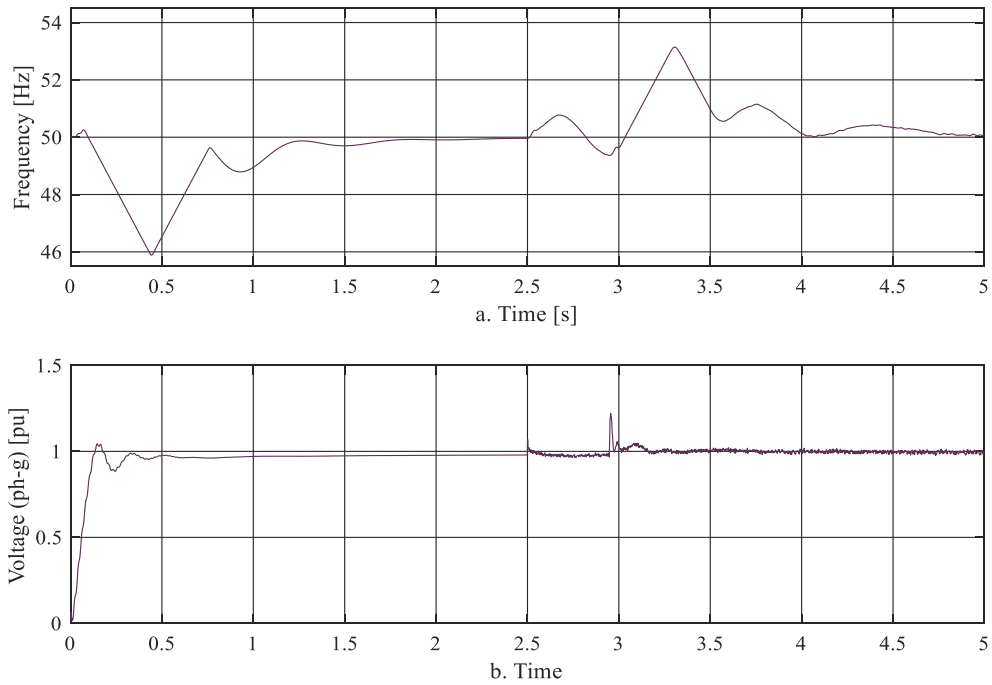


Figure 5.13. Black Start with Diesel Generator. a. Frequency, b. Voltage (ph-g)

Figure 5.14.a gives the active power produced by the diesel generator and PV-system, while Figure 5.14.b shows the generator speed. Initially the generator is running at nominal speed. This is however rapidly reduced as the loads are connected at $t = 0$ s. This reduces the speed to 0.86 p.u. while the active power production is increased to approximately 11 kW. The reduction in speed can also be seen in contexts with the frequency reduction in Figure 5.13.a. When the PV production increased to approximately 9 kW, the rotational speed reached 1.12 p.u. before the nominal speed was restored after $\Delta t = 3$ s. It is pointed out that the PV system did not perform as expected during these simulations, thus the validity of the results is further discussed in section 6.4.2.

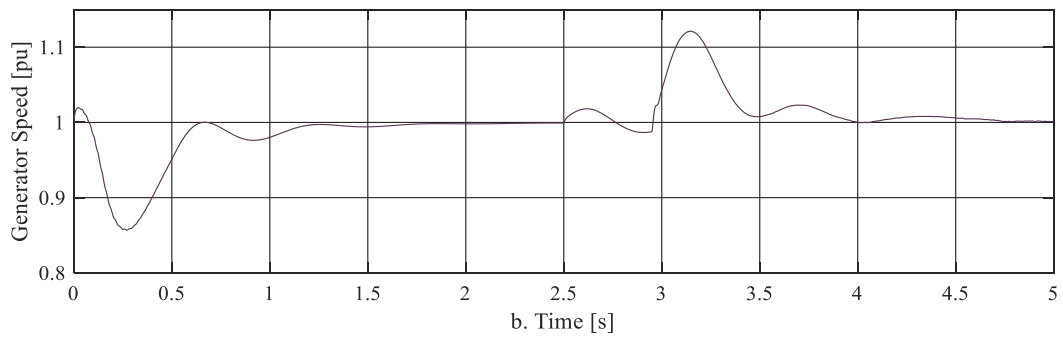
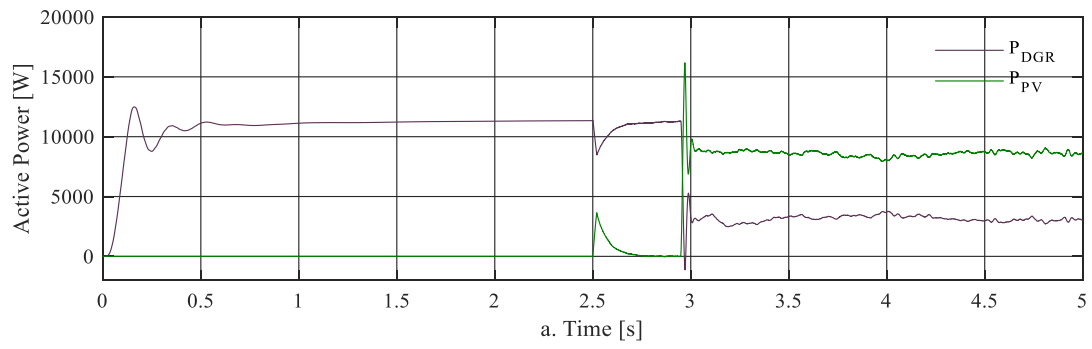


Figure 5.14. Black Start with Diesel Generator, a. Active Power [W], b. Generator Speed [pu]

6 Discussion

In this chapter the results provided in 5, "Cases and Results" are further discussed with regards to how they should be interpreted, and their limitations. First a general discussion on the simulation parameters and considered standards are provided, before each case is discussed individually.

6.1 General

Through the developed microgrid model a series of cases was simulated with a focus on the transition from grid-connected operation to islanded operation. With the complexity of several distributed generation units both the control and the choice of cases to simulate has been challenging. With the developed model a large variety of scenarios could be tested, either with a focus on grid-connected operation, islanded operation, or as presented in this thesis, the transition from one mode to another. In the previous chapter, only the main findings were presented and briefly commented. Hopefully, this chapter will contribute to clarification of any uncertainties and present possible improvements for further work with the subject.

To start off, all the simulations were performed with a discrete solver which time step is presented in appendix A.1. To give a realistic performance, the controllers sampling time is limited to two times the switching frequency. Impacts of changing both the simulation time step and control sampling time could affect the results, and these should be updated if further information on these parameters are obtained. However, simple testing in the model suggests that reduced sampling time and simulation time step has limited effect on the results.

Further, it would be interesting to compare the power quality from the results with demands for power quality in microgrids. Such standardized regulations have not been found for microgrids by the author. But, as stated in IEEE std. 2030-2018 [74] the operating requirements and range should be defined between the microgrid owner and the utility. Where grid codes, requirements in the jurisdiction and requirements from the DSO could serve as a foundation for such an agreement. Without clear requirements for microgrids, the Norwegian PQ-code FOL [68] and guidelines in IEEE Std. 1547-2018 [75] are used to give an insight to the power quality of the microgrid system. To restrict the scope of the thesis, THD-levels are not considered. It is pointed out that the harmonics generated from the VSC-connected distributed generation are present, but the content is not considered to influence the main findings and information provided. These harmonics can be reduced by enhanced control and better filter dimensioning.

The power quality at the connection points for the six consumers are not presented in this thesis. The results presented mainly utilizes measurements at the PCC. This means that the measured power consumption also includes the losses in the existing low voltage grid. With the existing low voltage grid being predominantly resistive this mainly impacts the active consumption. In addition, the voltage is reduced at point of connection for the customers compared to those obtained at PCC.

At last, it is highlighted that the obtained results in this thesis is based upon the developed model and has not been compared to laboratory tests or tangible measurements from an operating microgrid.

6.2 Intentional Islanding

The intentional islanding is a transition from grid-connected to islanded mode after a request to perform such an action. This implies that there is enough time to align the consumption and generation within the microgrid, thus reducing the active- and reactive power exchange at PCC to a minimum before disconnection is performed.

As the results reveal, this should not create any large deviations in the microgrid voltage or frequency. Small deviations can be observed because of two main reasons. Firstly, the generation and consumption are not perfectly aligned, with a mismatch in power of approximately -0.4 kW and 0.6 kVAr. It is argued that the small deviation could also be experienced in practice because of measurement errors or rapid changes in either loading condition or generation. Secondly, the BESS changes from PQ-control to V/f control. This change of control can introduce some challenges. When the BESS is in V/f-control the reference frequency is provided by an internal oscillator that gives the angular position of the rotating frame to perform the Park transformation. It is therefore of great importance that the internal oscillator signal is aligned with the grid frequency pre-islanding to prevent the BESS from switching at other instances than the rest of the VSCs connected generation. In simplicity, if ignoring the inertia differences, this can be compared to synchronizing to the grid without being in phase at synchronizing.

Further, the results only include one scenario for the intentional islanding. This is considered sufficient as long as the BESS can provide the necessary generation or consumption to ensure that equations (5.1) and (5.2) are fulfilled, i.e. there is no power exchange at PCC. With a lower consumption, that is plausible given the yearly consumption presented in [3], the BESSs power rating could be too low to handle the overproduction in the microgrid. To solve this, three solutions can be considered:

1. Reduce the production according to dispatching scheme.
2. Include a dump load to consume the excess power
3. Increase the BESS power capability

The first possibility could be solved by either the PV system or WT. As the PV system has no inertia, it should be rather simple to implement a control that alters the power point setting away from the MPP. Thus, changing the reference DC voltage such that the generation is reduced. To reduce the WT power generation the yaw control could be implemented to shed power in accordance to equation (3.51) [42], but alterations would be easier and faster if pitch control was available. A recommendation would in this case be to set up a curtailment priority scheme where the PV system is curtailed first. The second option with a dump load could be favorable if the dump load is providing energy storage in some form, either in form of heat or a rotating mass. The drawback of this will naturally be an increase in cost compared to simpler solutions where the excess power is simply wasted. The last solution is to increase the BESS power rating such that it can handle the maximum excess energy available, but the

beneficial gains must be considered against both the probability of such scenarios and the increase in cost.

6.3 Unintentional Islanding

In contrast to the intentional islanding, the unintentional islanding is challenging to foresee. Therefore, a contingency plan should be established to ensure a safe and robust system performance if the grid-connection is lost. Throughout this section, the results from the various unintentional islanding scenarios are further discussed.

6.3.1 Unintentional Islanding with BESS

Through four scenarios the microgrid has been unintentionally disconnected from the main grid at both export and import. In all the scenarios both the frequency and voltage remained within acceptable limits. These results should however be considered as an ideal unintentional islanding. The situation is ideal in form of a perfectly equal disconnection of all the phases simultaneously as the mode command signal is sent to the BESS. This arises the large assumption that the islanding detection has no time delay, whereas in [34] it is stated that detection time delay between 4 ms to 2 s could be anticipated depending on the detection method utilized. This has been implemented for a scenario in section 5.2.3 and is discussed in section 6.3.2.

Even though it can be argued that the results are neglecting an essential part of the process, the results provide some information on the BESS capability. When the islanded mode command signal is received by the BESS it switches from PQ-control to V/f-control. After approximately 100 ms the frequency from both the *High Export* and *High Import* scenarios are reestablished around its nominal value. A small overshoot in the power delivered by the BESS can be observed for the mentioned scenarios, but the settling time is within the millisecond area. This shows that the BESS is operating as expected and that it provides a fast response that rapidly ensures a steady-state operation of the islanded microgrid.

6.3.2 Unintentional with Detection Time Delay

From the results the voltage increased 75 % while the frequency increased to 55 Hz, after 100 ms, in the microgrid. Even though suggestions in IEEE Std. 1547-2018 opens for a cumulative transient overvoltage of up to two times the nominal voltage [75], the duration of the overvoltage for this simulation exceeds the recommendations. For the transition from grid-connected to islanded mode, the severity of the transient condition is highly dependent on the power mismatch. Without the V/f-control provided by the BESS, there is no control measures enabled to regulate the power production, or consumption, during the delay. This leads to a weakened power quality and stability concerns arise. This should be avoided by implementing protection schemes if no further changes are done to the control system.

One of the possible measures is to implement droop control for the WT and BESS when operating in PQ-control. However, low voltage grids often lack the predominantly inductive line impedance which forms the foundation for most droop control methods [13]. To

counteract this effect, a virtual impedance compensation has been implemented in [12] [13]. This effect improves the droop control during islanded mode, but does not consider the transition, and possible time delays from grid-connected mode to islanded mode. Hence the droop control must be enabled in grid-connected operation, which in worst case can lead to either oscillations in power generation or that the generation units operates at the upper- or lower limits due to deviation in the distribution grid steady state conditions. An option to the droop control could be to implement synthetic inertia response for the WT to mimic the response of a synchronous generator [6]. However, the WT ability is dependent on the wind speeds, such that similar solutions for the BESS would be interesting to further consider.

Another solution that is highly interesting, at least when exporting, is the use of a dump load. These are available on the market, where an AC-DC converter is utilized to bypass overproduction, both during transient conditions as this scenario, but also for power peaks from the wind turbine at wind gusts. This is recommended both to reduce stresses on the BESS, that currently absorbs overproduction from wind gusts, and to enhance power quality during islanded operation.

At last, it is mentioned that the modelled controls are based on feedforward loops and compensations that will affect the outputted power during transient condition. These effects are not only positive, as certain aspects of the production units' controls are based on steady-state assumptions which does not hold true during these scenarios. But this highlights the challenges with obtaining the required accuracy when modelling VSC connected generation and storage solutions. Without detailed data provided by manufacturers it is also challenging to verify the behavior without performing laboratory tests or accessing tangible measurements from similar situations in operating microgrids.

6.3.3 Unintentional Islanding during Import without BESS

Without the BESS available at islanding, the capability to perform a stable transition from grid-connected to islanded is challenged. Even though the results showed that a combination of droop control and load shedding could keep the microgrid frequency and voltage around their nominal values, a larger power mismatch would lead to instability. It can also be mentioned that only load shedding was also simulated, but the rapidly decreasing frequency lead to a blackout before load shedding was available. Hence, by only utilizing load shedding, this should be performed much faster than the assumed one second delay implemented in the simulated case. The low inertia in the microgrid system challenges the idea of load shedding as a practical alternative to provide stable frequency and voltage during islanding.

On the other side, the improved WT droop control with an integrator term had a profound effect on the frequency during islanding. By exploiting the inertia from the rotating mass of the WT, an increase of power delivered can be obtained to stabilize the frequency. This will however reduce the rotating speed and is therefore considered to be a limited resource. To reduce the stresses on both the generator and drive train, the maximum torque is restricted. This avoids an electrical torque beyond the maximum rated torque of the generator. Further, the improved WT droop control has been tested on import scenarios for up to 5 kW deficit without causing a frequency deviation more than 1.8 Hz, beyond this the stability is

challenged. After the grid is reconnected, BESS activated, or the diesel generator is ready to operate, the WT droop control is deactivated and the speed control reactivated. This allows for the WT to regain pre-disturbance state.

The option to an enhanced control of the WT and PV system, is to allow the system to be deenergized and perform a black start with the diesel generator. This would obviously reduce the microgrid's capability of providing continuous electrical energy, but on the other side it would reduce the control complexity and possibly costs associated with this. In the IEEE standard for specifications of microgrid controllers [72], both load shedding and black start are options that can be considered at unintentionally islanding to regain steady state operation.

An important assumption in the performed simulations is that the PV system handles the reactive power consumption. This is not an implemented control system in the developed microgrid model, but a simple setting of the reactive power reference in the PV system. This would mainly affect the voltage for a predominantly inductive grid, but in the proposed microgrid it could also affect the frequency. Therefore, both further considerations on the WT frequency droop control, a reactive droop control and implementing a droop controller with virtual impedance, as in [11] [12], would be a very interesting field to perform further research on.

6.4 Black Start Capability

In general, the black start results are highly dependent on the modelled energy resources and their initial response when connected. The initial responses for the WT, PV, BESS and DGR have not been verified by laboratory testing or tangible measurements, which should be kept in mind when assessing the result. In addition, enhanced soft starting procedures for both the PV- and WT-system is anticipated to have a positive effect on the black start transient conditions.

For the existing grid, the loads are connected as presented in Figure 3.5. Two factors should be considered from the existing grid. Firstly, the breakers present are most likely not controllable breakers, meaning that at least one new breaker must be implemented. Secondly, the six loads are supplied from two connections at the PCC busbar. This implies that load shedding can be performed in maximum two steps, unless communication with loads are established. This is not further considered in the simulated cases, where the complete load is connected at once. Hence, potential for reducing the transient condition by a stepwise connection of the loads could have been further considered.

6.4.1 Black Start with BESS

The black start results with the BESS shows that both the nominal frequency and voltage can be obtained with a connected load of $S = (16.5 + j 5.4)kVA$. For the given situation the BESS alone could have supplied the load, but this would eventually lead to a SOC-level below the lower limit of the BESS. Therefore, the PV and WT system are connected to provide electric energy, thus realizing a longer operation in islanded mode without running the diesel generator. It is pointed out that steady state islanded operation is obtained after 100 ms if

only the BESS and loads are considered. This shows that a the microgrid system can restore the nominal frequency and voltage rapidly after a system blackout. Thus, allowing a system blackout followed by a black start might be an alternative to a seamless transition.

When the PV system is connected, a rapid decrease in the BESS power production and a 20 % increase in the PV systems DC-voltage is observed. This is handled by the system, but measures could, and should be taken to reduce this transient. As the PV system is connected it is already close to MPP, which leads to an instantaneous power production of approximately 15 kW. By reducing the reference DC-voltage when the PV system is initially connected, and gradually increasing it after connection, the transient is anticipated to be strongly reduced. This is however not implemented in the current model but can be added by acting on the DC-reference voltage.

The WT's rotor and generator are operating at nominal speed when connected at $t = 1$ s. The power delivered from the WT system is then gradually increased until it reaches the nominal power production, at given wind speed, after approximately $\Delta t = 0.4$ s. With a gradually increasing active power, the transient reaction is also limited, leading to a seamless transition from discharging to charging of the BESS. The reactive power exchange is set to zero for the WT system in the black start scenario, but the contribution could have been altered to provide voltage support during initiation of the WT system. This is however not considered necessary with the BESS capability of a fast response.

6.4.2 Black Start with Diesel Generator

The main differences between the DGR system and the BESS is the lacking capability of consuming active power and a slower response. This impacts the serial restoration strategy with a longer time frame before steady state is achieved, and a limitation on the contribution from the WT and PV system. In the proposed black start procedure only the PV system is connected, even though this has shown to give the largest transients. In practice, as for the BESS black start, the PV system generation should be ramped up to reduce the impact.

To avoid running two parallel diesel generators the load was in this case reduced to $S = (11.9 + j 3.9) \text{ kVA}$. For the proposed microgrid this can still be considered a high loading scenario, as the consumption rarely exceeds these levels [3]. Otherwise, load shedding can be performed to reduce the consumption below the diesel generator rating of 15 kVA. The upside of the loading condition is allowing for one generator to run at close to rated capacity, while the downside is that the load is large compared to the rated capacity of the diesel generator system. However, the diesel generator system obtains nominal speed after 1.75 seconds with the full load connected. It is mentioned here that the generator initially was running at nominal speed at $t = 0$ s.

The lowest frequency was 45.9 Hz as the loads was connected. This is considered a very low frequency that could impact the load behavior. Even though no clear guidelines for frequency deviations in microgrids are established, the Norwegian regulation FOL indicates that areas that are temporarily not connected to the adjoining grid should normally remain within $50 \pm 2\%$ [68]. Here, the term "normally" could open for a larger frequency deviation in specific situations. However, the frequency deviation in the diesel generator black start is severe and

should not be acceptable. To resolve the situation, a gradual addition of loads should be performed in accordance to a dispatching scheme depending on how critical the load is.

The highest frequency and overvoltage are observed after the PV system is connected at $t = 2.5$ s. As mentioned in the previous section 6.4.1, "Black Start with BESS", the PV system connection procedure should be altered to reduce the transient response. In addition, the PV system response is odd, as the DC-voltage increases before the PV system delivers power corresponding to the MPP at $t = 2.9$ s. This reveals some challenges with the model for assessing initial conditions, thus reducing the validity of the results for the black start procedure.

7 Conclusion

The control and stability of a low voltage microgrid has been assessed through a developed model in the Matlab/Simulink environment. The investigated microgrid model consist of a wind turbine, a battery energy storage solution, a photovoltaic system, a diesel generator, loads and a connection to the distribution grid. In this chapter, the main conclusions from this thesis is highlighted.

Through model validation, the system components performance was individually assessed before combining them to form a microgrid system. The existing low voltage grid and connection to the distribution grid was shown to comply with the obtained three-phase short circuit currents, provided from Sunnfjord Energi Nett, except for a 4.5 % error for one of the connection points. This was because of an uncertainty in one of the conductor types. Overall, the results were assumed to be acceptable. For the VSC connected PV- and WT-system, outer control loops enabled an optimized active power production while remaining stable through alterations in solar irradiance and wind speed, respectively. The BESS was considered to perform satisfactorily in both grid-connected mode, islanded mode, and through the transition between modes. Islanded operation of the diesel generator system showed some oscillations in power output during load change, but the overall performance was acceptable.

An overall control strategy was to operate the PV- and WT systems as PQ-controlled units, while the BESS was set to operate with PQ-control when grid-connected and voltage- and frequency control when islanded. To validate the system performance, the microgrids ability to transition from grid-connected operation to islanded operation was thoroughly tested through simulations of intentional- and unintentional islanding. With close to zero power exchange between the distribution grid and the microgrid, the control for intentional islanding retained the nominal frequency, AC- and DC-voltage through the transition. The ability to perform a stable transition was also shown for unintentional islanding with various export- and import scenarios. However, when introducing a time delay representing the islanding detection system, for an export scenario, the microgrid experienced a heightened RMS voltage of 1.7 p.u. times the nominal voltage and a frequency deviation of $\Delta f = 5 \text{ Hz}$ for a delayed mode signal exceeding 50 ms. A controlled dump load, implementation of enhanced droop control or synthetic inertia control was considered a possible solution for this situation, but not included in the model.

Without the BESS enabled, a transition from grid-connected to islanded mode was considered during import of power. By utilizing the inertia stored in the rotating mass of the WT, a droop control was implemented. Simulations showed the ability to cease the frequency decline and restore the nominal frequency. This led to a reduction in the WT rotating speed, which revealed the droop controls dependency on available inertia.

For transitions where the voltage and frequency transients exceed the microgrid specification, a system blackout could occur. To enhance the electric supply reliability within the microgrid, it was shown that a black start is possible, either by use of the BESS or the diesel generator system. A lower frequency of 45.9 Hz during the black start for the diesel generator suggested that a load dispatch scheme should be considered to improve black start performance.

The implementation of a microgrid system for the proposed case area is through both the specialization thesis and this thesis considered to be a feasible solution. Although, technical challenges associated with a seamless transition from grid-connected to islanded mode was highlighted in this thesis.

8 Further Work

With limited time the thesis scope had to be restricted. This implies that further work on both the proposed microgrid, and work related to the increasing penetration of distributed generation with regards to stability and control is highly relevant on the way towards the future smart grid. Some possibilities for further work and shortcomings are:

- With the proposed model, simulations in islanded mode with large load changes, non-linear loads, and unbalanced loading conditions has been performed but not included to restrict the scope and work load. However, the initial attempts suggest that the proposed control system handles this.
- A laboratory setup would be interesting to consider the severity of simplifications and limitations in the model compared to actual component performances.
- Improvements of the existing control to enhance system stability for transitions where a time delay is present because of the islanding detection system.
- Implementing a virtual impedance droop controller as an addition or replacement of the frequency control for islanded operation.
- Short circuit studies and protection of the microgrid would be of great interest, and importance, towards the establishment of the microgrid.
- The realization of a pilot-microgrid for the proposed area to obtain information, experience and to build competence was the main motivation and objective behind this thesis and is therefore highly recommended for future work.

9 References

- [1] O. R. Valmot, "Snart 150 år med strøm i Norge: Her er elektrisitetens historie", *Teknisk Ukeblad*. Accessed: Apr. 13, 2019. [Online]. Available <https://www.tu.no/artikler/snart-150-ar-med-strom-i-norge-her-er-elektrisitetens-historie/429910>
- [2] Ministry of Climate and Environment, "Norway's Climate Strategy for 2030: a transformational approach within a European cooperation framework — Meld. St. 41 (2016–2017) Report to the Storting." [Online]. Available: <https://www.regjeringen.no/en/dokumenter/meld.-st.-41-20162017/id2557401/sec2?q=Paris#KAP2-3>.
- [3] R. Thoresen, "Technical and Economic Evaluation of Microgrids: An Isolated Microgrid Case Study", Specialization Project, Dept. Electric Power Engineering, NTNU, Norway, Des. 2018.
- [4] A. Hariharan, G. G. Karady and P. E. J. Dickinson, "Application of Machine Learning Algorithm to Forecast Load and Development of a Battery Control Algorithm to Optimize PV System Performance in Phoenix, Arizona", *2018 North American Power Symposium (NAPS)*, Fargo, USA, 2018, doi: 10.1109/NAPS.2018.8600594.
- [5] G. Henri and N. Lu, "A Supervised Machine Learning Approach to Control Energy Storage Devices", *IEEE Transactions on Smart Grid*, March 2019, doi: 10.1109/TSG.2019.2892586.
- [6] J. V. de Vyver, J. D. M. De Kooning, B. Meersman, L. Vandeveldel and T. L. Vandoorn, "Droop Control as an Alternative Inertial Response Strategy for the Synthetic Inertia on Wind Turbines", *IEEE Transactions on Power Systems*, vol. 31, no. 2, pp. 1129-1138, May 2015, doi: 10.1109/TPWRS.2015.2417758.
- [7] H. Laaksonen, P. Saari and K. Risto, "Voltage and Frequency Control of Inverter Based Weak LV Network Microgrid", *Int. Conf. on Future Power Systems*, Amsterdam, Nov. 2005, doi: 10.1109/FPS.2005.204293.
- [8] A. Yazdani and R. Iravani, "Controlled-Frequency VSC System", in *Voltage-Sourced Converters in Power Systems*, U.S.: John Wiley & Sons, Inc., 2010, ch.9, pp. 245-244.

- [9] S. Zafar, H. Sadiq, B. Javaid and H. A. Khalid, "On PQ Control of BESS in Grid-Connected Mode and Frequency Control in Islanded-Mode for Micro-Grid Application," *Int. Conf. on Computing, Electronic and Electrical Engineering (ICE Cube)*, Quetta, Pakistan, IEEE, 2018, doi: 10.1109/ICECUBE.2018.8610962.
- [10] J. Zhou and P. Cheng, "A modified Q-V droop control for accurate reactive power sharing in distributed generation microgrid," *Energy Conversion Congress and Exposition (ECCE)*, Cincinnati, USA, 2017, doi: 10.1109/ECCE.2017.8096713.
- [11] Y. Mohamed and E. F. El-Saadany, "Adaptive Decentralized Droop Controller to Preserve Power Sharing Stability of Paralleled Inverters in Distributed Generation Microgrids," *IEEE Transactions on Power Electronics*, vol. 23, no. 6, pp. 2806-2016, Nov. 2008, doi: 10.1109/TPEL.2008.2005100.
- [12] F. Göthner, O. M. Midtgård, R. Torres-Olguin and S. D'Arco, "Effect of Including Transient Virtual Impedance in Droop-Controlled Microgrids," *EEEIC/I&CPS Europe*, Palermo, Italy, June 2018, doi: 10.1109/EEEIC.2018.8493932.
- [13] Y. W. Li and C. N. Kao, "An Accurate Power Control Strategy for Power-Electronics-Interfaced Distribution Generation Units Operating in a Low Voltage Multibus Microgrid," *IEEE Transactions on Power Electronics*, vol. 24, no. 12, pp. 2977-2988, Dec. 2009, doi: 10.1109/TPEL.2009.2022828.
- [14] N. Mohan, T. M. Undeland and W. P. Robbins, *Power Electronics: Converters, Applications, and Design*, US, John Wiley & Sons, Inc., 1995.
- [15] *IEEE Application Guide for IEEE Std 1547TM, IEEE Standard for Interconnecting Distributed Resources with Electric Power Systems*, 1547TM, IEEE, Park Avenue, New York, April 2009, doi: 10.1109/IEEESTD.2008.4816078.
- [16] A. Yazdani and R. Iravani, "Grid-Imposed Frequency VSC System: Control in dq-Frame," in *Voltage-Sourced Converters in Power Systems*, U.S.: John Wiley & Sons, Inc., 2010, ch. 8, pp.204-244.
- [17] C. Bajracharya, M. Molinas, J. A. Suul and T. M. Undeland, "Understanding of tuning techniques of converter controllers for VSC-HVDC," *Nordic Workshop on Power and Industrial Electronics*, Helsinki, Finland, June 2008.
- [18] A. Yazdani and R. Iravani, "Two-Level, Three-Phase Voltage-Sourced Converter," in *Voltage-Sourced Converters in Power Systems*, U.S.: John Wiley & Sons, Inc., 2010, ch.5, pp. 115-125.

- [19] V. Blasko and V. Kaura, "A New Mathematical Model and Control of a Three-Phase AC-DC Voltage Sourced Converter," *IEEE Transactions on Power Electronics*, vol.12, no.1, pp. 116-123, Jan. 1997, doi: 10.1109/63.554176.
- [20] MathWorks, *PI Section Line*. Accessed: Jan. 24, 2019. [Online]. Available: <https://se.mathworks.com/help/physmod/sps/powersys/ref/pisectionline.html>
- [21] MathWorks, *Three Phase PI Section Line*. Accessed: Jan. 24, 2019. [Online]. Available: <https://se.mathworks.com/help/physmod/sps/powersys/ref/threephasepisectionline.html>
- [22] MathWorks, *PV Array*. Accessed: Feb. 12, 2019. [Online]. Available: <https://se.mathworks.com/help/physmod/sps/powersys/ref/pvarray.html>
- [23] M. A. G. de Brito, L. P. Sampaio, G. Luigi, G. A. Melo and C. A. Canesin, "Comparative analysis of MPPT techniques for PV applications," 2011 Int. Conf. on Clean Elect. Power (ICCEP), Ischia, Italy, June 2011, doi: 10.1109/ICCEP.2011.6036361.
- [24] G. M. Masters, "Photovoltaic Materials and Electrical Characteristics," in *Renewable and Efficient Power Systems*, 2nd ed. U.S.: John Wiley & Sons, Inc., 2013, ch. 5, pp. 253-315.
- [25] E. Tedeschi. (2018). Control of Voltage Source Converters: DC Voltage control loop design and tuning procedure [Notes].
- [26] International Renewable Energy Agency, "Electricity Storage and Renewables: Costs and Markets to 2030," IRENA, Abu Dhabi, Oct. 2017. Accessed: Sept. 8, 2018. [Online]. Available: ISBN: 978-92-9260-038-9.
- [27] International Renewable Energy Agency, "Battery Storage for Renewables: Market Status and Technology Outlook," IRENA, Abu Dhabi, Oct. 2017. Accessed: Sept. 8, 2018. [Online]. Available: ISBN: 978-92-95111-54-7.
- [28] MathWorks, *Battery*. Accessed: Feb. 8, 2019. [Online]. Available: <https://se.mathworks.com/help/physmod/sps/powersys/ref/battery.html>.
- [29] L. H. Saw, K. Somasundaram, Y. Ye and A. A. O. Tay, "Electro-thermal analysis of Lithium Iron Phosphate battery for electric vehicles," *Journal of Power Sources*, Elsevier, vol. 249, pp. 231-238, Mar. 2014. doi: 10.1016/j.jpowsour.2013.10.052.
- [30] LG Chem, *Catalog 2018, (2018)*. Accessed: Mar. 5, 2019. [Online]. Available: <https://www.lgchem.com/global/ess/ess/product-detail-PDEC0001>.

- [31] A. Yazdani and R. Iravani, "Variable-Frequency VSC System," in *Voltage-Sourced Converters in Power Systems*, U.S.: John Wiley & Sons, Inc., 2010, ch. 10, pp.270-307.
- [32] A. Yazdani, "Control of an Islanded Distributed Energy Resource Unit with Load Compensating Feed-Forward," *IEEE Power and Energy Soc. General Meeting – Convers. and Del. of Elect. Energy in the 21st Century*, Pittsburg, USA, July 2008, doi: 10.1109/PES.2008.4595978.
- [33] M. B. Delghavi and A. Yazdani, "Islanded-Mode Control of Electronically Coupled Distributed-Resource Units Under Unbalanced and Nonlinear Load Conditions," *IEEE Trans. on Power Del.*, vol. 20, no. 2, pp. 661-673, Apr. 2011, doi: 10.1109/TPWRD.2010.2042081
- [34] C. Li, Y. Cao, C. Cao, Y. Kuang, L. Zeng and B. Fang, "A review of islanding detection methods for microgrid," *Renewable and Sustain. Energy Rev.*, Elsevier, vol. 35, pp. 211-220, July 2014, doi: 10.1016/j.rser.2014.04.026.
- [35] P. Sørensen, B. Andresen, J. Fortmann and P. Pourbeik, "Modular structure of wind turbine models in IEC 61400-27-1," *IEEE Power & Energy Soc. General Meeting*, Vancouver, Canada, July 2013, doi: 10.1109/PESMG.2013.6672279.
- [36] G. M. Masters, "Wind Power Systems," in *Renewable and Efficient Electric Power Systems*, 2nd ed. U.S.: John Wiley & Sons, Inc., 2013, ch. 7, pp. 410-497.
- [37] J. G. Slootweg, S. W. H. Haan, H. Polinder and W. L. King, "General model for representing variable speed wind turbines in power system dynamics simulations," *IEEE Trans. on Power Syst.*, vol. 18, nr. 1, pp. 144-151, Feb. 2003, doi: 10.1109/TPWRS.2002.807113.
- [38] J. G. Slootweg, H. Polinder and W. L. Kling, "Representing wind turbine electrical generating systems in fundamental frequency simulations," *IEEE Trans. on Energy Convers.*, vol. 18, no. 4, pp. 516-524, Dec. 2003, doi: 10.1109/TEC.2003.816593.
- [39] H. Dharmawardena and K. Uhlen, "Modeling variable speed wind turbine for power system dynamic studies," *IEEE Students Conf. on Eng. and Syst. (SCES)*, Allahabad, India, Nov. 2015, doi: 10.1109/SCES.2015.7506448.
- [40] N. Jones and K. Sweeney, *Test Summary Report for the Solid Wind Power SWP 25-14TG20 Small Wind Turbine*. (2015). Accessed: Nov. 8, 2018. [Online]. Available: http://small-wind.org/download/certification_reports/SWP25-14GT20.pdf

- [41] P. D. Clausen and D. H. Wood, "Recent Advances in Small Wind Turbine Technology," *Sage Journals*, vol. 24, no. 3, pp.189-201, May 2000, doi: 10.1260/0309524001495558.
- [42] H. Shariatpanah, R. Fadaeinedjad and M. Rashidinejad, "A New Model for PMSG-Based Wind Turbine With Yaw Control," *IEEE Trans. on Energy Convers.*, vol. 28, no. 4, pp. 929-937, Dec. 2013, doi: 10.1109/TEC.2013.2281814.
- [43] J. G. Slootweg, H. Polinder and W. L. Kling, "Reduced-order Modelling of Wind Turbines," in *Wind Power in Power Systems*, T. Ackermann, West Sussex, U.K.: John Wiley & Sons, Ltd., 2005, ch. 25, pp. 555-586.
- [44] B. Liu, X. Peng and T. Undeland, "Centralized power control strategy of offshore wind farm with permanent magnetic generators," *IEEE 6th Int. Power Electron. and Motion Control Conf.*, Wuhan, China, May 2009, doi: 10.1109/IPEMC.2009.5157544.
- [45] A. G. Rodriguez, A. G. G. Rodriguez and M. B. Payan, "Estimating Wind Turbines Mechanical Constants," *Renewable Energy and Power Quality J.*, vol. 1, no. 5, pp. 697-704, Mar. 2007, doi: 10.24084/repqj05.361.
- [46] S. D. Umans, *Electric Machinery*, 6th ed. New York, U.S.: McGraw-Hill Education, Inc., 2003.
- [47] S. M. Mirbagheri, S. M. H. Mousavi, S. S. S. G. Sefid and H. Safaeipour, "The comparison of single-cage and double cage induction generators at variable frequencies," *IEEE Int. Conf. on Power Electronics, Drives and Energy Syst. (PEDES)*, Bengaluru, India, Dec. 2012, doi: 10.1109/PEDES.2012.6484266.
- [48] S. J. Chapman, *Electric Machinery Fundamentals*, 5th ed. New York, U.S.: McGraw-Hill, Inc., 2012.
- [49] A. Abbaszadeh, S. Lesan and V. Morteza pour, "Transient response of doubly fed induction generator under voltage sag using an accurate model," *IEEE PES/IAS Conf. on Sustain. Alternative Energy (SAE)*, Valencia, Spain, Sept. 2009, doi: 10.1109/SAE.2009.5534834.
- [50] J. Pedra, "On the Determination of Induction Motor Parameters From Manufacturer Data for Electromagnetic Transient Programs," *IEEE Trans. on Power Syst.*, Nov. 2008, vol. 23, no. 4, pp. 1709-1718, Nov. 2008, doi: 10.1109/TPWRS.2008.2002293.
- [51] MathWorks, *Asynchronous Machine*, Accessed: Feb. 13, 2019. [Online]. Available: <https://www.mathworks.com/help/phymod/sps/powersys/ref/asynchronousmachine.html>

- [52] MathWorks, *power_AynchronousMachineParams*, Accessed: Mar. 7, 2019. [Online]. Available: https://se.mathworks.com/help/physmod/sps/powersys/ref/power_asynchronousmachineparams.html
- [53] X. Ran, S. Miao and Y. Wu, "Improved Adaptive Droop Control Design for Optimal Power Sharing in VSC-MTDC Integrating Wind Farms," *Energies*, vol. 8, no. 7, pp. 7100-7121, Jul. 2015, doi: 10.3390/en8077100.
- [54] B. K. Bose, "Control and Estimations of Induction Motor Drives," *Modern Power Electronics and AC Drives*, New Jersey, U.S.: Prentice Hall PTR, 2002, ch.8, pp. 333-437.
- [55] D. J. Hogan, F. Gonzalez-Espin, J. G. Hayes, G. Lightbody, L. Albiol-Tendillo and R. Foley, "Virtual synchronous-machine control of voltage-source converters in a low-voltage microgrid," *18th European Conf. on Power Electron. and Appl.*, Karlsruhe, Germany, Oct. 2016, doi: 10.1109/EPE.2016.7695503.
- [56] R. Hunter and G. Elliot, "Wind-diesel system options", in *Wind-Diesel Systems: A Guide to the Technology and its Implementation*, Cambridge: Cambridge University Press, 1994, ch. 1, pp. 5-26.
- [57] L. Luo, L. Gao and H. Fu, "The Control and Modeling of Diesel Generator Set in Electric Propulsion Ship," *Int. J. of Inf. Technol and Comput. Sci.*, vol. 3, no. 2, pp. 31-37, Mar. 2011, doi: 10.5815/ijitcs.2011.02.05.
- [58] S. Roy, O. P. Malik and G. S. Hope, "An Adaptive Control Scheme for Speed Control of Diesel Driven Power-Plants," *IEEE Trans. on Energy Convers.*, vol. 6, no. 4, pp. 605-611, Dec. 1991, doi: 10.1109/60.103632.
- [59] B. Kuang, Y. Wang and Y. L. Tan, "An H ∞ Controller Design for Diesel Engine Systems", *Int. Conf. on Power Syst. Technol.*, Perth, Australia, Dec 2000, doi: 10.1109/ICPST.2000.900032.
- [60] D. Yubing, G. Yulei, L. Qingmin and W. Hui, "Modelling and simulation of the microsources within a microgrid," *Int. Conf. on Electrical Machines and Syst.*, Wuhan, China, Oct. 2008, available: <https://ieeexplore.ieee.org/document/4771204>
- [61] MathWorks, *Synchronous Machine*, Accessed: Feb. 15, 2019. [Online]. Available: <https://se.mathworks.com/help/physmod/sps/powersys/ref/synchronousmachine.html>

- [62] *IEEE Recommended Practice for Excitation System Models for Power System Stability Studies*, Std 421.5-2016, IEEE, New York, USA, May 2016, doi: 10.1109/IEEESTD.2016.7553421.
- [63] MathWorks, *AC5A Excitation System*, Accessed: Feb. 26, 2019. [Online]. Available: <https://se.mathworks.com/help/physmod/sps/powersys/ref/ac5aexcitationsystem.html>
- [64] *IEEE Recommended Practice for Excitation System Models for Power System Stability Studies*, Std 421.5-2005, IEEE, New York, USA, Apr. 2005, doi: 10.1109/IEEESTD.2006.99499.
- [65] *Short-circuit currents in three-phase a.c. systems – Part 0: Calculation of Currents*, NEK IEC 60909-0, 2016.
- [66] A. Samadi, M. Ghandhari and L. Söder, "Reactive Power Assessment of a PV System in a Distribution Grid", *Energy Procedia*, vol. 20, pp. 98-107, 2012, doi: 10.1016/j.egypro.2012.03.012.
- [67] G. M. Masters, "Photovoltaic Systems," in *Renewable and Efficient Electric Power Systems*, 2nd ed. U.S.: John Wiley & Sons, Inc., 2013, ch. 6, pp. 316-409.
- [68] *Forskrift om leveringskvalitet i kraftsystemet*, Olje- og energidepartementet, 2004.
- [69] F. Katiraei, M. R. Iravani and P. W. Lehn, "Micro-Grid Autonomous Operation During and Subsequent to Islanding Process," *IEEE Trans. on Power Delivery*, vol. 20, no. 1, pp. 248-257, Jan. 2005, doi: 10.1109/TPWRD.2004.835051.
- [70] R. Majumder, "Some Aspects of Stability in Microgrids," *IEEE Trans. on Power Syst.*, vol. 28, no. 3, pp. 3243-3252, Aug. 2013, doi: 10.1109/TPWRS.2012.2234146.
- [71] ABB R&D, *Technical Specification AMG0180AA04*, (2012). Accessed: Mar. 10, 2019. [Online]. Available: <https://library.e.abb.com/public/0e8088eccc4a13f548257a1b00310ff3/5862120-B-AMG%200180AA04%20Technical%20specification.pdf>
- [72] *IEEE Standard for the Specification of Microgrid Controllers*, Std. 2030.7-2017, IEEE, New York, USA, Apr. 2018, electronic ISBN: 978-1-5044-4515-3.
- [73] Z. Xu, P. Yang, Q. Zheng and Z. Zeng, "Study on black start strategy of microgrid with PV and multiple energy storage systems," *18th Int. Conf. on Elect. Mach. and Syst.*, Pattaya, Thailand, Oct. 2015, doi: 10.1109/ICEMS.2015.7385067.

- [74] *IEEE Standard for the Testing of Microgrid Controllers*, Std. 2030.8-2018, IEEE, New York, USA, Aug. 2018, electronic ISBN: 978-1-5044-5050-8.
- [75] *IEEE Standard for Interconnection and Interoperability of Distributed Energy Resources with Associated Electric Power Systems Interfaces*, Std. 1547-2018, IEEE, New York, USA, Apr. 2018, doi: 10.1109/IEEESTD.2018.8332112.
- [76] S. Henschel, "Analysis of Electromagnetic and Electromechanical Power," Ph.D. dissertation, Dept of Elect. & Computer Eng., The Univ. of British Columbia, Vancouver, Canada, 1999. [Online]. Available: <https://open.library.ubc.ca/cIRcle/collections/ubctheses/831/items/1.0065161>
- [77] J. C. G. de Siqueira, B. D. Bonatto, J. R. Marti, J. A. Hollman and H. W. Dommel, "Optimum time step size and maximum simulation time in EMTP-based programs," *Power Syst. Computation Conf.*, Wroclaw, Poland, Aug. 2014, doi: 10.1109/PSCC.2014.7038485.
- [78] A. Rygg, email correspondence, Apr. 11, 2019.
- [79] VEM, *Low voltage asynchronous motors: IEC motors with squirrel-cage rotor*, (2012). Accessed: Apr. 4, 2019. [Online]. Available: <https://www.vem-group.com/en/products-services/low-voltage/iec-standard-motors/downloads.html>
- [80] VEM, *Three-phase asynchronous generators*. Accessed: Apr. 4, 2019. [Online]. <https://www.vem-group.com/en/products-services/low-voltage/asynchronous-generators/downloads.html>
- [81] V. Akhmatov, H. Knudsen and A. H. Nielsen, "Advanced simulation of windmills in the electric power supply," *Int. J. of Elect. Power and Energy Syst.*, vol. 22, no. 6, pp. 421-434, Aug. 2000, doi: 10.1016/S0142-0615(00)00007-7.
- [82] F. González-Longatt, P. Regulski, H. Novanda and V. Terzija, "Effect of the shaft stiffness on the inertial response of the fixed speed wind turbines and its contribution to the system inertia," *Int. Conf. on Adv. Power Syst. Automation and Protection*, Beijing, China, Oct. 2011, doi: 10.1109/APAP.2011.6180555.
- [83] S. M. Mueen, J. Tamura and T. Murata, "Wind Turbine Modelling", in *Stability Augmentation of a Grid-connected Wind Farm*, London, U.K.: Springer, 2009, ch. 2, pp. 23-65.
- [84] S. K. Chaudhary, "Control and Protection of Wind Power Plants with VSC-HVDC Connection," Ph.D. dissertation, Dept of Energy Technol., Aalborg Univ., Aalborg, Denmark, 2011.

- [85] S. Preitl and R. E. Precup, "An extension of tuning relations after symmetrical optimum method for PI and PID controllers," *Automatica*, vol. 35, no. 10, pp. 1731-1736, Oct. 1999, doi: 10.1016/S0005-1098(99)00091-6.
- [86] M. O. L. Hansen, "1-D Momentum Theory for an Ideal Wind Turbine" in *Aerodynamics of Wind Turbines*, 2nd ed., London, UK: Earthscan, 2009, ch. 4, pp. 27-40.

10 Appendices

Description of the attached appendices:

- A. System Parameters** – gives parameters for each of the subsystems
- B. Load Distribution for Scenarios** – shows the dispersed load used in scenarios
- C. Per Unit Systems** – gives the per unit systems for each subsystem
- D. The Park Transformation** – presents the theory behind the dq-reference frame
- E. Tuning Techniques** – introduction to modulus optimum and symmetrical optimum
- F. Tuning of Microgrid Controllers** – gives the open loop transfer function and tuning of PI controllers in the system
- G. Simulink Model** – presents the main parts of the microgrid modelled in Simulink

A. System Parameters

A.1 Sampling Time & Switching Frequency

The sampling time is dependent at which frequencies the phenomena assessed occurs. In the system presented in this thesis the maximum frequency of the operating components is the VSC switching at 4.95 kHz. As the frequency of interest is unknown, the switching frequency is used as a starting point for the frequency of interest. The analysis is performed in the time domain, where the sampling time is set to ten times the switching frequency. This is based on the “rule” of performing sampling five times the Nyquist theorem [76] [77].

For the PI controllers, they can in practice be set to sample at two times the highest switching frequency, where a common practice is to perform switching at 2 kHz and sampling at 4 kHz [78].

Sampling Parameters

Parameter	Symbol	Definition	Value
Nominal Frequency	f_{nom}		50 Hz
Switching Frequency	f_{sw}	$99 \cdot f_{nom}$	4950 Hz
Simulation Time Step	$T_{s,Power}$	$\frac{f_{sw}}{10}$	20 μ s
Sampling Time Controllers	$T_{s,Control}$	$2 \cdot f_{sw}$	0.1 ms

A.2 Existing grid

Conductors in the Existing Low Voltage Grid

Connection Point	Line/Cable	Length
House 1	EX 1x3x25 Al	78 m
	EX 1x3x50 Al	27 m
House 2	EX 1x3x25 Al	23 m
	EX 1x3x50 Al	76 m
House 3	EX 1x3x25 Al	17 m
	EX 1x3x50 Al	76 m
Cabin 1	EX 1x3x25 Al	39 m
	1x10 Cu	294 m
	EX 1x3x50 Al	27 m
Cabin 2	EX 1x3x25 Al	47 m
	EX 1x3x50 Al	76 m
Cabin 3	TFLP 1x3x50 Al	65 m
	EX 1x3x50 Al	461 m

Conductor Specification

Conductor	Positive Resistance r1 [ohm/km]	Zero Resistance r0 [ohm/km]	Positive Inductive Reactance l1 [ohm/km]	Zero Inductive Reactance l0 [ohm/km]	Positive Capacitance c1 [nF/km]	Zero Capacitance c0 [nF/km]
X 1x3x25 Al	1.2	1.35	0.083	2.5	0.55	0.28
EX 1x3x50 Al	0.641	0.79	0.079	2.45	0.8	0.41
1x10 Cu	1.784	0.8*	0.396	3*	9.25	4.05
TFLP 1x3x50 Al	0.641	0.6*	0.075	2.5*	1.08	0.53

Values obtained from Sunnfjord Energi Nett AS

*Estimated values

The parameters given in Figure 3.6, can be calculated from the given conductor specifications by using the provided equations in [21]:

$$R_s = \frac{2r_1 + r_0}{3} \quad (1)$$

$$L_s = \frac{2l_1 + l_0}{3} \quad (2)$$

$$R_m = \frac{r_0 - r_1}{3} \quad (3)$$

$$L_m = \frac{l_0 - l_1}{3} \quad (4)$$

$$C_p = c_1 \quad (5)$$

$$C_g = \frac{3c_1c_0}{c_1 - c_0} \quad (6)$$

Distribution Grid Parameters

Parameter	Symbol	Value
Short Circuit Power Maximum	S_k	0.322 MVA
Resistance	R_{th}	81 mΩ
Inductive Reactance	X_{th}	152 mΩ
Voltage factor Maximum	c_{min}	0.90
Voltage Factor Minimum	c_{max}	1.05

A.3 PV System

Main parameters for the PV system and PV modules are given in Table A.3.1. I-V characteristics for the system is given in Figure A.3.1, with an open circuit voltage of 760 V and a short circuit current of 54 A during STC. The I-V characteristics of Figure A.3.2 shows how solar irradiance and temperature affect the PV array output.

Table A.3.1 PV System Parameters

Parameter	Symbol	Value
Rated power	P_{nom}	31 kW
Number of modules	N_{mod}	120
Strings	N_{string}	6
Open Circuit Voltage (module)	V_{OC}	37.8 V
MPP Voltage (module)	V_{MPP}	30.7 V
Short Circuit Current (module)	I_{SC}	9.01 A
MPP Current (module)	I_{MPP}	8.5 A
DC-Capacitance	C_{dc}	1.36 pu
Filter Resistance	R_f	0.05 pu
Filter Inductance	L_f	0.92 pu
MPPT Upper DC-Voltage	$V_{MPPT,max}$	680 V
MPPT Lower DC-Voltage	$V_{MPP,min}$	300 V

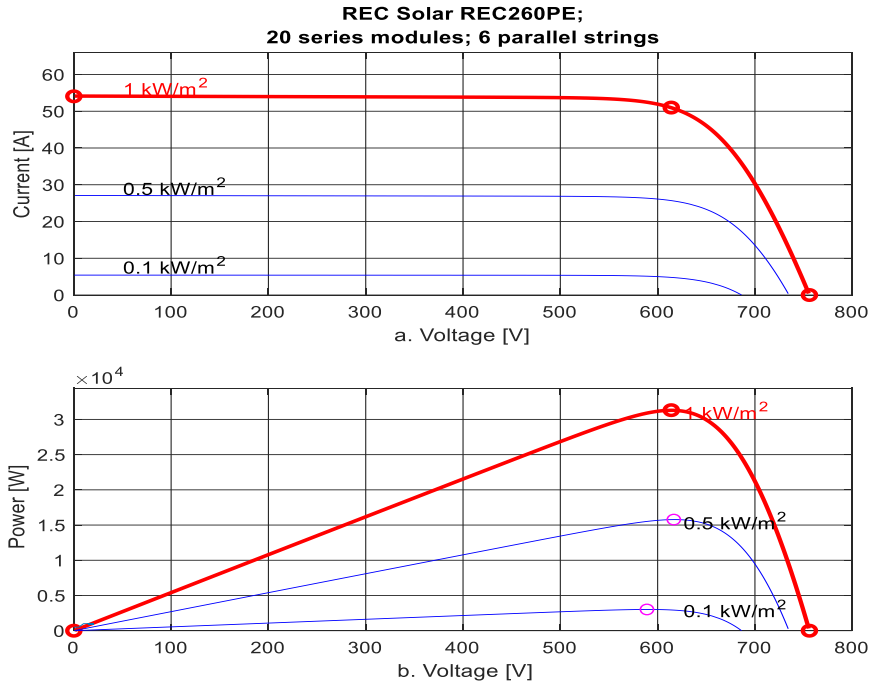


Figure A.3.1 PV system output ratings at STC. a) Current-voltage (I-V), b) Power-voltage (P-V)

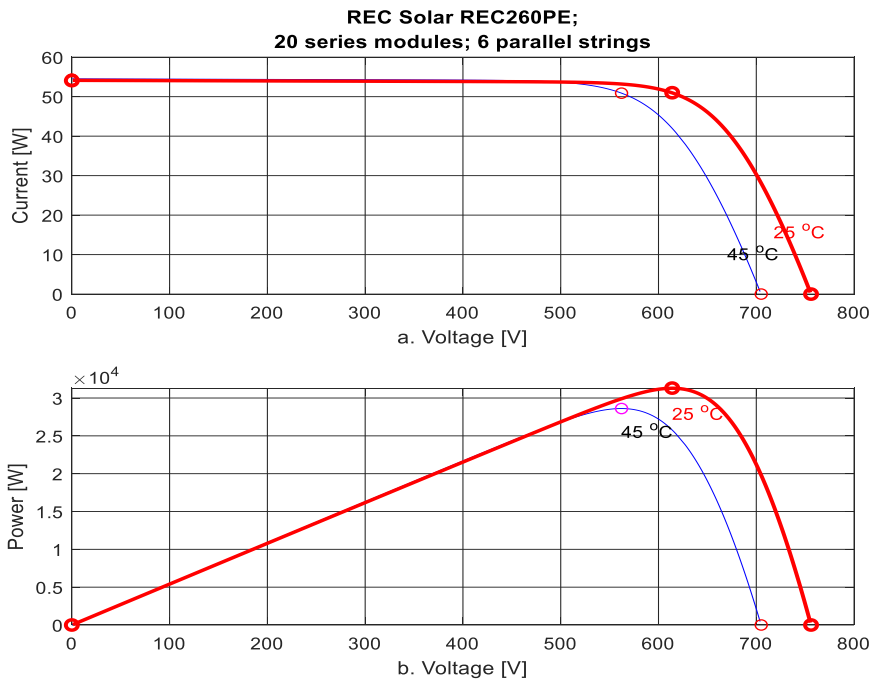
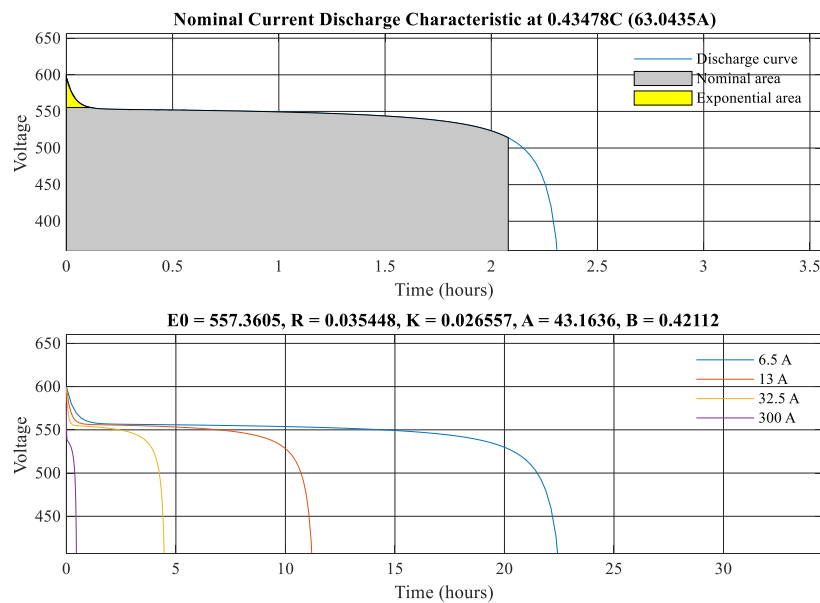


Figure A.3.2 PV system output ratings at varying cell temperature. a) Current-voltage (I-V), b) Power-voltage (P-V)

A.4 BESS

Parameters BESS

Parameter	Symbol	Value
Rated Power	P_{nom}	32 kW
Number of Modules	N_{mod}	10
Capacity	A_{nom}	145 Ah
Rated Energy	E_{nom}	74 kWh
Nominal Voltage	$V_{dc,nom}$	514 V
Cut-off Voltage	$V_{dc,min}$	385.5 V
Fully Charged Voltage	$V_{dc,FC}$	598.3 V
Nominal Discharge Current	$I_{dc,nom}$	63.0 A
Battery Response Time	t_{res}	1 s
DC Capacitance	C_{dc}	1.88 pu
Filter Inductance	L_f	0.95 pu
Filter Resistance	R_f	0.026 pu
Filter Capacitance	C_f	0.19 pu



Current Discharge Characteristics at: a. Nominal Current, b. 6.5 A, 13 A, 32.5 A, 300 A [28].

A.5 WTS

Parameters WT System

Parameter	Symbol	Value
Rated power	P_{nom}	30 kW
Nominal Voltage	V_{nom}	400 V
Tower Height	h_t	18 m
Nominal Wind Speed	$V_{W,0}$	11 m/s
Cut-in wind speed	$V_{W,in}$	3 m/s
Cut-out wind speed	$V_{W,out}$	25 m/s
Pitch		Fixed
Yaw		Active Yaw
Total Inertia Constant	H_{tot}	1.91 s
Pole Pairs	p	3
Stator [Resistance, Inductance]	L_f	[0.099 Ω 0.0011 H]
Cage 1 [Resistance, Inductance]	L_f	[0.1578 Ω 0.0033 H]
Cage 2 [Resistance, Inductance]	L_f	[0.3943 Ω 0.0011 H]
Mutual Inductance	L_m	0.03458 H
DC Capacitance	C_{dc}	0.73 pu
Filter Inductance	L_f	0.88 pu
Filter Resistance	R_f	0.016 pu
Speed Control PI Time Constant	$T_{i, speed}$	0.75 s
Speed Control PI Proportional Gain	P_{speed}	100
Aerodynamic Constants	$[c_1 c_2 c_3 c_4 c_5 c_6 c_7 c_8 c_9]$	[0.345 210 0 0 0 32 11.5 0 – 0.075]

Parameters obtained from [52], based on data sheet for 30 kW 6-pole machines [79] [80]

Parameter	Symbol	Specified	Obtained
Nominal Full Load Current	I_{nom}	54 A	53.86 A
Nominal Voltage	V_{nom}	400 V	400 V
Nominal Frequency	f_{nom}	50 Hz	50 Hz
Starting Current	I_{max}	$6.5 \cdot I_{nom}$	$6.14 \cdot I_{nom}$
Nominal Torque	T_{nom}	294.5 Nm	294.14 Nm
Starting Torque	T_{start}	$2.2 \cdot T_{nom}$	$2.21 \cdot T_{nom}$
Breakdown Torque	T_{break}	$2.5 \cdot T_{nom}$	$2.6 \cdot T_{nom}$
Slip in rpm	s	25 rpm	
Poles	p	3	3
Nominal Power Factor	PF	0.85	0.845

A.6 Diesel Generator System

Diesel Generator System Parameters

Parameter	Abbreviation	Value
Power	S_n	15 kVA
Voltage	V_n	400 V
Frequency	f_n	50 Hz
Proportional Gain (PI reg.)	k_p	8.0
Time Integral (PI reg.)	T_i	0.55
Actuator Time Constant	T_a	0.05 s
d-axis Synchronous Reactance	X_d	2.249 pu
d-axis Transient Reactance	X'_d	0.350 pu
d-axis Subtransient Reactance	X''_d	0.236 pu
q-axis Synchronous Reactance	X_q	1.095 pu
q-axis Transient Reactance	X''_q	0.182 pu
Leakage Reactance	X_l	0.07 pu
Time constants	T'_d	0.050 s
	T''_d	0.0042 s
	T''_q	0.0045 s
Stator resistance*	R_s	0.0645 pu
Inertia	J_{SM}	0.19 kgm ²
Friction factor*	B_f	0.02 pu
Pole Pairs	p	2
Engine Time Delay	t_D	0.05 s

* Approximated values from preset model in Simulink [61]

Based on ABB generator data [71]

A.7 Two-Mass Model Drivetrain for Directly Coupled WT and DGR

The drivetrain is represented as a two-mass described based on equations provided in [43], with alteration to include mutual damping and pole pairs, and neglecting friction factors:

$$\frac{d\omega_{wr}}{dt} = \frac{T_{wr} - (K_s\theta + MD(\omega_{wr} - \omega_m))}{2H_{wr}} \quad (7)$$

$$\frac{d\omega_m}{dt} = \frac{(K_s\theta + MD(\omega_{wr} - \omega_m)) - T_e}{2H_m} \quad (8)$$

$$\frac{d\theta}{dt} = \frac{2\pi f_n(\omega_{wr} - \omega_m)}{p} \quad (9)$$

Where ω is the rotating speed [pu], the shaft stiffness is given by K_s [pu/el.rad], θ is the angular displacement of the shaft [°], H is the inertia constant [pu], T is the torque [pu], MD is the mutual damping [pu], p is number of pole pairs and f_n is the nominal grid frequency in hertz. Subscripts m , e and wr stands for the generator mechanical, generator electrical and wind turbine rotor respectively.

The generator inertia constant is calculated on basis of the given moment of inertia in manufacturer data sheet. The shaft stiffness can be converted to the per unitized system by considering the shafts eigenfrequencies, where some literature suggests that the shaft stiffness should be set between 0.3-0.5 p.u. [45] [81]. With active stall-controlled wind turbines in the upper range and pitch controlled in the lower range [82]. Results provided in [83] suggest that self-damping have a low impact on stability compared to the effect of mutual damping. This is supported by [45] for fixed speed wind turbines, hence the mutual damping is implemented, and self-damping neglected.

Shaft Stiffness	K_{tot}	0.5 pu [82]
Mutual Damping	D_M	25 pu [45]
Self-Damping	D_s	Not implemented

Scenario 6 Unintentional Islanding without BESS	Total Load: 28.2 kW + j 6 kVAr	
	Cabin 1: P= 0.855 kW Q = 0.185 kVAr	House 1: P= 13 kW Q = 2.80 kVAr
	Cabin 2: P= 1.54 kW Q = 0.33 kVAr	House 2: P= 1.71 kW Q = 0.37 kVAr
	Cabin 3: P= 6.84 kW Q = 1.48 kVAr	House 3: P= 4.28 kW Q = 0.922 kVAr

Black Start with BESS	Equal to Scenario 2-5	
-----------------------	-----------------------	--

Black Start with Diesel Generator (Modelled with parallel RLC loads to avoid inductances in series with the synchronous generator, which is modelled as a current source)	Total Load: 11.9 kW + j 3.9 kVAr	
	Cabin 1: P= 0.35 kW Q = 0.12 kVAr	House 1: P= 5.39 kW Q = 1.77 kVAr
	Cabin 2: P= 0.64 kW Q = 0.21 kVAr	House 2: P= 0.70 kW Q = 0.23 kVAr
	Cabin 3: P= 2.8 kW Q = 0.93 kVAr	House 3: P= 1.77 kW Q = 0.58 kVAr

* at 230 V reference

C. Per Unit Systems

The overall microgrids distributed generation units are divided into four subsections for modelling purposes, each with its own per unit system. This is done to provide a clear understanding of the subsystem parameters, i.e. 1 p.u. represents the subsystem's nominal value. Figure C.1 shows the defined and separated per unit systems. Per unitizations performed on equations, and presented results, are based on the definitions presented in the following sections.

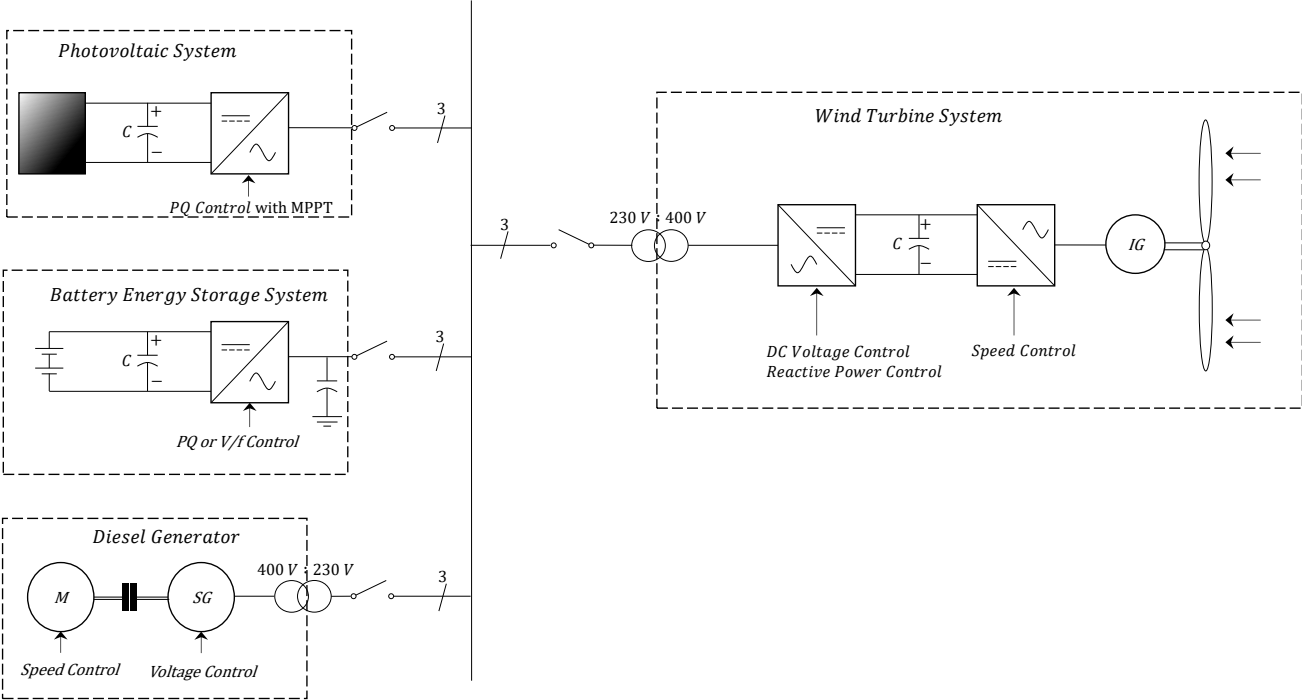


Figure C.1. Per Unit Systems in the Microgrid

C.1 PV System

Base Values for PV System

Parameter	Symbol	Definition	Value
Base Apparent Power	S_b	S_b	31 <i>kVAr</i>
Base Active Power	P_b	P_b	31 <i>kW</i>
Base Frequency	f_b	$f_b = \frac{\omega_b}{2\pi}$	50 <i>Hz</i>
Base Voltage	V_b	$V_{abc,LL} \cdot \sqrt{\left(\frac{2}{3}\right)}$	187.8 <i>V</i>
Base Current	I_b	$\frac{2 P_b}{3 V_b}$	110 <i>A</i>
Base DC-Voltage	$V_{b,DC}$	$2 * V_b$	375.6 <i>V</i>
Base Impedance	Z_b	$\frac{V_b}{I_b}$	1.71 Ω
Base Capacitance	C_b	$\frac{1}{Z_b \omega_b}$	1.9 <i>mF</i>
Base Inductance	L_b	$\frac{Z_b}{\omega_b}$	5.4 <i>mH</i>

C.2 Battery Energy Storage System

Base Values for BESS

Parameter	Symbol	Definition	Value
Base Apparent Power	S_b	S_b	32 kVAr
Base Active Power	P_b	P_b	32 kW
Base Frequency	f_b	$f_b = \frac{\omega_b}{2\pi}$	50 Hz
Base Voltage	V_b	$V_{abc,LL} \cdot \sqrt{\left(\frac{2}{3}\right)}$	187.8 V
Base Current	I_b	$\frac{2 P_b}{3 V_b}$	114 A
Base DC-Voltage	$V_{b,DC}$	$2 * V_b$	375.6 V
Base Impedance	Z_b	$\frac{V_b}{I_b}$	1.65 Ω
Base Capacitance	C_b	$\frac{1}{Z_b \omega_b}$	1.9 mF
Base Inductance	L_b	$\frac{Z_b}{\omega_b}$	5.3 mH

C.3 Wind Turbine System

Base Values for WT System

Parameter	Symbol	Definition	Value
Base Apparent Power	S_b	S_b	30 <i>kVAr</i>
Base Active Power	P_b	P_b	30 <i>kW</i>
Base Frequency	f_b	$f_b = \frac{\omega_b}{2\pi}$	50 <i>Hz</i>
Base Voltage	V_b	$V_{abc,LL} \cdot \sqrt{\left(\frac{2}{3}\right)}$	326.6 <i>V</i>
Base Current	I_b	$\frac{2 P_b}{3 V_b}$	61.2 <i>A</i>
Base DC-Voltage	$V_{b,DC}$	$2 * V_b$	653 <i>V</i>
Base Impedance	Z_b	$\frac{V_b}{I_b}$	5.3 Ω
Base Capacitance	C_b	$\frac{1}{Z_b \omega_b}$	0.6 <i>mF</i>
Base Inductance	L_b	$\frac{Z_b}{\omega_b}$	17 <i>mH</i>

C.4 Diesel Generator System

Base Values for DGR System

Parameter	Symbol	Definition	Value
Base Apparent Power	S_b	S_b	15 <i>kVAr</i>
Base Active Power	P_b	P_b	15 <i>kW</i>
Base Frequency	f_b	$f_b = \frac{\omega_b}{2\pi}$	50 <i>Hz</i>
Base Voltage	V_b	$V_{abc,LL} \cdot \sqrt{\left(\frac{2}{3}\right)}$	326.6 <i>V</i>
Base Current	I_b	$\frac{2 P_b}{3 V_b}$	30.6 <i>A</i>
Base Impedance	Z_b	$\frac{V_b}{I_b}$	10.7 Ω

D. The Park Transformation

To reduce the complexity for solving control- and power system problems the three-phase rotating abc -reference frame can be represented by a rotating two-axis reference frame dq [19]⁷. Provided with Figure D.4 the transformation of variables to the dq -reference is found by (10) and the inverse transformation as (11) [46].

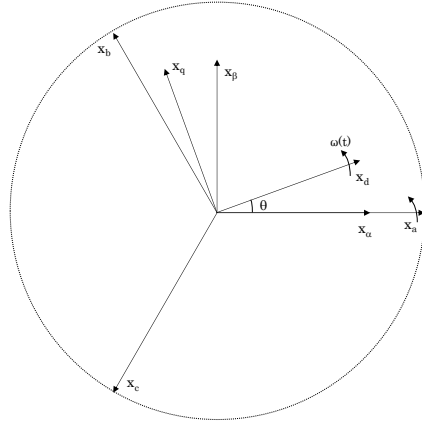


Figure D.4 Three phases in stationary and rotating reference frames

$$\begin{bmatrix} x_d \\ x_q \\ x_0 \end{bmatrix} = \frac{2}{3} \cdot \begin{bmatrix} \cos(\theta) & \cos(\theta - 120^\circ) & \cos(\theta + 120^\circ) \\ -\sin(\theta) & -\sin(\theta - 120^\circ) & -\sin(\theta + 120^\circ) \\ \frac{1}{2} & \frac{1}{2} & \frac{1}{2} \end{bmatrix} \cdot \begin{bmatrix} x_a \\ x_b \\ x_c \end{bmatrix} \quad (10)$$

$$\begin{bmatrix} x_a \\ x_b \\ x_c \end{bmatrix} = \begin{bmatrix} \cos(\theta) & -\sin(\theta) & 1 \\ \cos(\theta - 120^\circ) & -\sin(\theta - 120^\circ) & 1 \\ \cos(\theta + 120^\circ) & -\sin(\theta + 120^\circ) & 1 \end{bmatrix} \cdot \begin{bmatrix} x_d \\ x_q \\ x_0 \end{bmatrix} \quad (11)$$

Provided a balanced system, such that $x_a + x_b + x_c = 0$ it is observed that the $x_0 = 0$. This is utilized to further simplify control of the system and is an assumption used for the controllers presented in this thesis. Further, the term $\frac{2}{3}$ ensures that the magnitude of $x_d = x_a$ [84], which is utilized for both voltages and currents represented in the dq -reference frame.

⁷ A possibility is also to represent the system by a two-axis stationary reference frame through a Clark transformation, known as the $a\beta$ -frame before introducing the dq -reference frame. Relationship $(x_d + jx_q) = (x_a + jx_\beta)e^{-j\theta}$

E. Tuning Techniques

In this thesis mainly two tuning techniques are utilized for tuning of the various PI controllers implemented. Their principle is presented in this section as an introduction to the specific tuning procedures on the microgrid system controllers. Mainly PI controllers are implemented in this thesis, with transfer function:

$$H_{PI} = \frac{K_{PI}(1 + T_i s)}{T_i} \quad (12)$$

With K_{PI} is the proportional gain while T_i represents the integral time. For the VSC it is utilized cascade control which requires that the response speed increases from outer to inner control loop [17]. Therefore, the inner loops are tuned according to the modulus optimum where a fast response is provided, while the outer loops are tuned according to the symmetrical optimum to handle disturbances [17].

E.1 Modulus Optimum

The modulus optimum, also referred to as the absolute value optimum criterion, is widely used because of the simplicity and fast response. For systems with one dominant and one minor time constant modulus optimum can be achieved by cancelling out the largest time constant while still providing unity gain for high frequencies [17]. Given the open loop transfer function of example (13), with one dominant time constant T_D and one minor T_m the PI controller parameters can be found by (14) and (15). The presented open loop transfer function of eq has the same order as the implemented current controllers in this thesis and hence the same principle is applied.

$$H_{OL} = \frac{K_{PI}(1 + T_i s)}{T_i} \cdot \frac{1}{1 + T_D s} \cdot \frac{1}{1 + T_m s} \cdot K \quad (13)$$

$$T_i = T_D \quad (14)$$

$$K_{p,vu} = \frac{T_D}{2T_m K} \quad (15)$$

Provided with the tuning technique the closed loop transfer function is presented as (16) with natural oscillation and damping factor according to (17) and (18) respectively.

$$H_{CL}(s) = \frac{1}{2T_m^2 s^2 + 2T_m s + 1} \quad (16)$$

$$\omega_n = \frac{1}{T_m \sqrt{2}} \quad (17)$$

$$\zeta = \frac{1}{\sqrt{2}} \quad (18)$$

E.2 Symmetrical Optimum

For the outer control loop, in a cascade control, the symmetrical optimum can be applied to maximize the phase margin and thus increasing stability. Provided with open loop transfer function (19) there are two poles at origin. With the Nyquist criteria for stability (20) the phase margin ϕ_M is maximized at a crossover frequency ω_c (21) (34) between the time constants T_a and T_b [17]. From evaluating the maximum phase angle ϕ_M a symmetric distance "a" can be found [17]. This leads to the tuning criteria as shown in (22) and (23).

$$G_{OL}(s) = \frac{K_{PI}(1 + T_i s)}{T_i} \cdot \frac{1}{1 + T_a s} \cdot \frac{1}{T_b s} \cdot K \quad (19)$$

$$|H_{OL}(j\omega)| = 1 ; \angle G_{OL} = -180^\circ + \phi_M \quad (20)$$

$$\omega_c = \frac{1}{\sqrt{T_a T_i}} \quad (21)$$

$$T_i = a^2 \cdot T_a \quad (22)$$

$$K_{PI} = \frac{T_b}{a \cdot K \cdot T_a} \quad (23)$$

From the closed loop transfer function "a" defines the roots of the system (24) and thereby the transient response [17]. In [17] it is stated that the factor a is normally constrained within the range of 2 to 4.

$$\begin{aligned} a < 3 &\rightarrow \text{Complex conjugated roots} \\ a = 3 &\rightarrow \text{real and equal roots} \\ a > 3 &\rightarrow \text{real and distinct roots} \end{aligned} \quad (24)$$

F. Tuning of Microgrid Controllers

In the following sections the deduction of the open loop transfer functions and tuning of system controllers are presented. This includes a step response of the controllers closed loop transfer functions and a Nichols plot of the open loop transfer functions. To give an overview, the PI-controllers proportional gain and time constants, along with the gain margin ΔK and the phase margin ψ , and the tuning methods are collected in Table F. 1. Detailed information is provided for the tuning of each controller in the following sections.

Table F. 1. Summarized Main Parameters from Tuning of System Controllers

Control	PI-Setting and Stability Margins	Tuning Method
PV Current Control	$T_i = 0.0588 \text{ s}$ $K_p = 9.67$ $\Delta K = \infty$ $\psi = 65.5^\circ$	Modulus Optimum
PV DC Voltage Control	$T_i = 0.0027 \text{ s}$ $K_p = 2.57$ $\Delta K = \infty$ $\psi = 53.1^\circ$	Symmetrical Optimum
BESS Current Control	$T_i = 0.118 \text{ s}$ $K_p = 9.98$ $\Delta K = \infty$ $\psi = 65.5^\circ$	Modulus Optimum
BESS Voltage Control	$T_i = 0.0027 \text{ s}$ $K_p = 9.36$ $\Delta K = \infty$ $\psi = 53.1^\circ$	Symmetrical Optimum
DGR Speed Control	$T_i = 0.55 \text{ s}$ $K_p = 14.55$ $\Delta K = \infty$ $\psi = 87.6^\circ$	Trial and Error

WT SSC Current Control	$T_i = 0.0588 \text{ s}$ $K_p = 9.67$ $\Delta K = \infty$ $\psi = 51.8^\circ$	Modulus Optimum
WT SSC DC Voltage Control	$T_i = 0.0027 \text{ s}$ $K_p = 2.56$ $\Delta K = \infty$ $\psi = 53.1^\circ$	Symmetrical Optimum
WT SSC Reactive Power Control	$T_i = 0.0011 \text{ s}$ $K_p = 3.1$ $\Delta K = \infty$ $\psi = 53.4^\circ$	Symmetrical Optimum
WT MSC Current Control	$T_i = 0.0278 \text{ s}$ $K_p = 18.2$ $\Delta K = \infty$ $\psi = 51.8^\circ$	Modulus Optimum
WT MSC Speed Control	$T_i = 0.75 \text{ s}$ $K_p = 100$	Trial and Error

F.1 PV Current Controller

The open loop transfer function for the PV current controller is given as [17]:

$$G_{OL}(s) = G_{PI}(s)G_{PWM}(s)G_{RL}(s) = K_{p,pu} \cdot \frac{1 + T_i s}{T_i s} \cdot \frac{1}{1 + T_a s} \cdot \frac{1}{R_{pu}(1 + T_{pu} s)} \quad (25)$$

With G_{PI} representing the PI controller, G_{RL} the RL-filter dynamics and G_{PWM} the sample- and hold and switching operation. T_a and T_{pu} is defined according to (26) and (27), respectively [17] [19]. With one dominant time constant, and another minor time constant, modulus optimum was used to cancel out the dominant one. Hence providing unity gain up to high frequencies [17].

$$T_{pu} = \frac{L_{f,pu}}{R_{f,pu} * \omega_B} \quad (26)$$

$$T_a = \frac{1.5}{2 * f_{sw}} \quad (27)$$

Where R_f is the filter resistance, L_f is the filter inductance, and ω_B is the base angular frequency. The PWM is represented with a first order transfer function which includes the hold- and sample, and switching delays. PI controller parameters are given by (28) and (29).

$$T_i = T_{pu} = 0.0588 \text{ s} \quad (28)$$

$$K_p = \frac{\tau_{pu} * R_{pu}}{2 * T_a} = 9.67 \quad (29)$$

A step response of the closed loop transfer function is shown in Figure F. 1. This shows that the regulated signal has a 4 % overshoot and settles below 2 % after 1.34 ms. In the frequency domain the open loop transfer function is plotted in a Nichols plot. Figure F. 2 shows the Nichols plot with stability margins $\Delta K = \infty$ and $\psi = 65.5^\circ$.

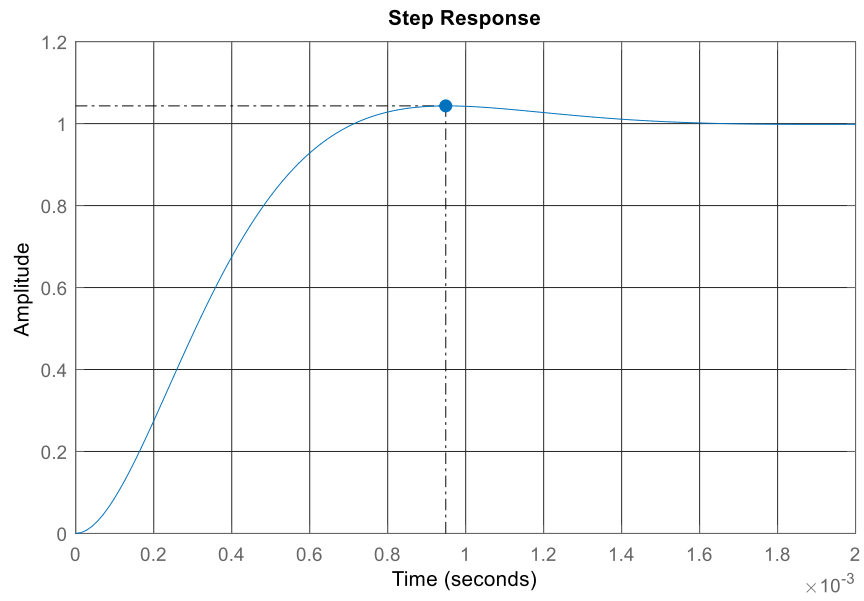


Figure F. 1 Step Response PV Current Controller

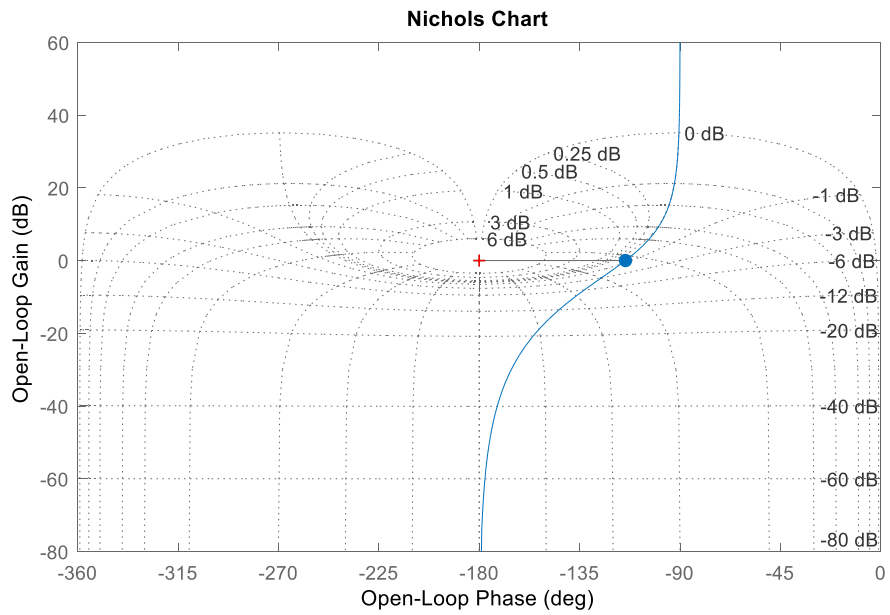


Figure F. 2. Nichols Chart PV Current Controller

F.2 PV DC-Voltage Controller

The DC voltage controller open loop transfer function is given by [17]:

$$G_{OL}(s) = G_{PI}(s)G_{eq}(s)G_{DC}(s) = K_{p,pu} \cdot \frac{1 + T_i s}{T_i s} \cdot \frac{1}{1 + T_{eq} s} \cdot \frac{v_{d,pu}}{V_{DC,pu}} \cdot \frac{1}{T_c s} \quad (30)$$

With G_{PI} representing the PI controller, G_c the capacitor dynamics with time constant according to (31), and G_{eq} represents the current controller. The current controller can be shown to suit a first order transfer function estimated by (32), with T_a representing the sample-and-hold and PWM generation [19]. Using modulus optimum pole cancellation by setting $T_i = T_{eq}$ would lead to two poles at origin and hence an unstable system [17]. Therefore, symmetrical optimum was implemented for PI controller tuning.

$$T_c = \frac{1}{\omega_B * C_{pu}} \quad (31)$$

$$T_{eq} = 2 * T_a \quad (32)$$

Utilizing the Nyquist criteria for stability, the PI controller parameters was estimated by (33) and (34) to achieve a satisfactory response and phase margin. For the PV DC-voltage controller, $a = 3$ was chosen, which gives real and equal roots while being within the recommended range of 2-4 [17] [85].

$$T_i = a^2 * T_{eq} \quad (33)$$

$$K_p = \frac{T_c}{a * T_{eq}} \quad (34)$$

Inserted with parameter values the gain and time constant of the PI-controller yields:

$$T_i = 0.0027 \text{ s} \quad (35)$$

$$K_p = 2.57 \quad (36)$$

A step response of the closed loop transfer function is shown in Figure F. 3. This shows that the regulated signal has a 25 % overshoot and settles below 2 % after 7.4 ms. Figure F. 4 shows the Nichols plot with stability margins $\Delta K = \infty$ and $\psi = 53.1^\circ$.

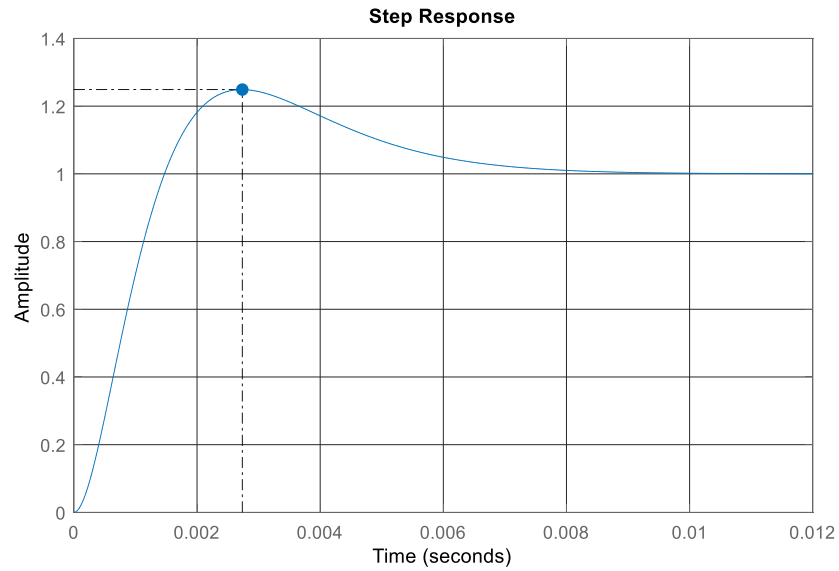


Figure F. 3. Step Response PV Voltage Controller

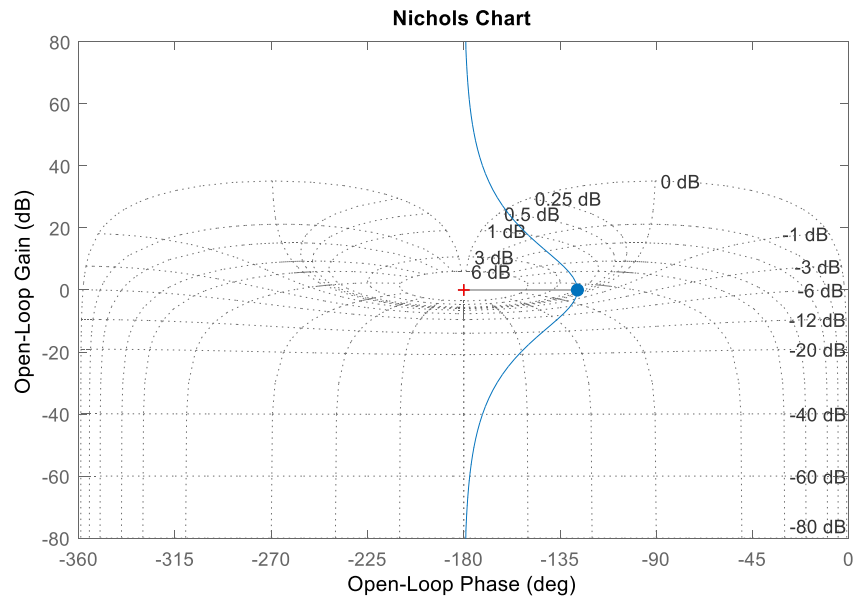


Figure F. 4. Nichols Chart PV Voltage Controller

F.3 BESS Current Controller

The open loop transfer function for the BESS current controller is given by (37) [17].

$$G_{OL}(s) = G_{PI}(s)G_{PWM}(s)G_{RL}(s) = K_{p,pu} \cdot \frac{1 + T_i s}{T_i s} \cdot \frac{1}{1 + T_a s} \cdot \frac{1}{R_{pu}(1 + T_{pu} s)} \quad (37)$$

As for the PV current controller, modulus optimum is used to cancel out the dominant pole and provides a unity gain up to high frequencies [17]. PI controller parameters are given by (38) and (39):

$$T_i = T_{pu} = 0.118 \text{ s} \quad (38)$$

$$K_p = \frac{T_{pu} \cdot R_{pu}}{2 T_a} = 9.98 \quad (39)$$

A step response of the closed loop transfer function is shown in Figure F. 5. This shows that the regulated signal has a 4 % overshoot and settles below 2 % after 1.3 ms. Figure F. 6 shows the Nichols plot with stability margins $\Delta K = \infty$ and $\psi = 65.5^\circ$.

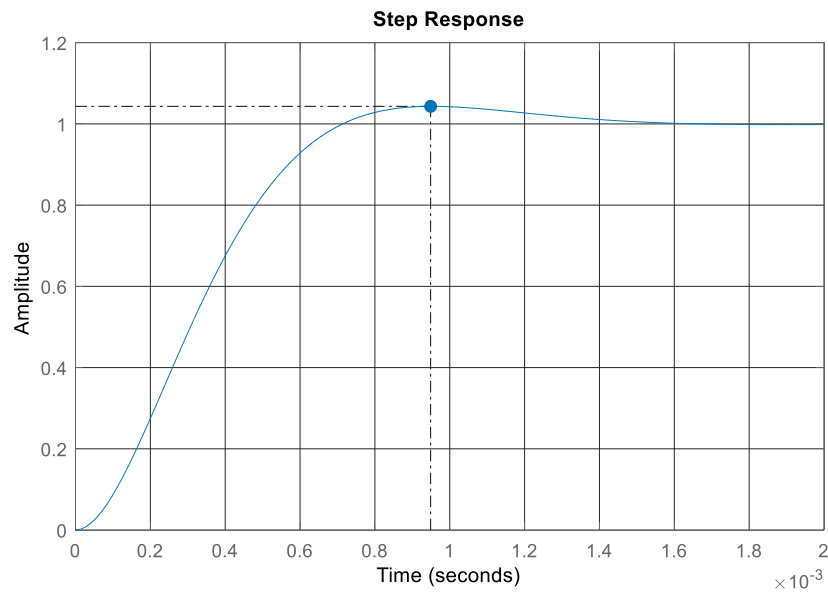


Figure F. 5. Step Response BESS Current Controller

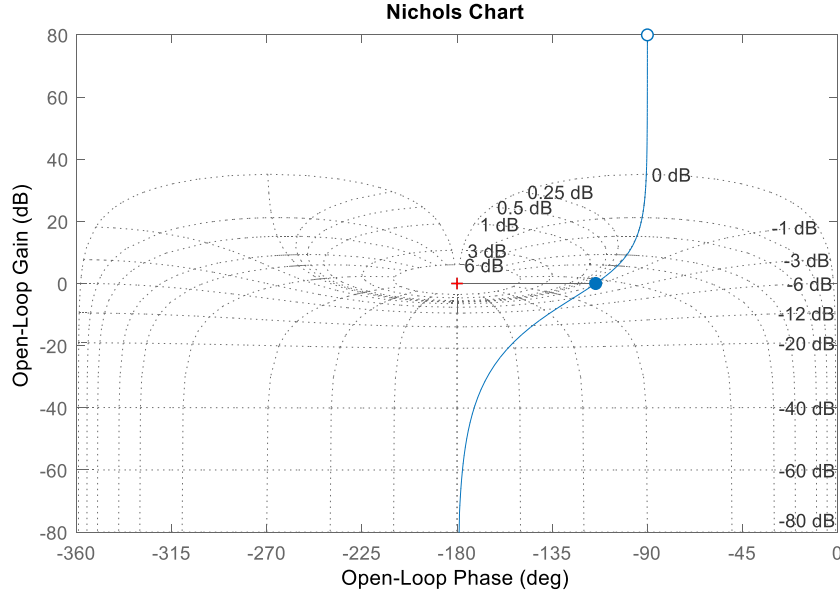


Figure F. 6. Nichols Chart BESS Current Controller

F.4 BESS Voltage Controller

The BESS voltage controller open loop transfer function is given by (40) [8].

$$G_{OL}(s) = G_{PI}(s)G_{eq}(s)G_C(s) = K_{p,pu} \cdot \frac{1 + T_{iv}s}{T_{iv}s} \cdot \frac{1}{1 + T_{eq}s} \cdot \frac{1}{T_C s} \quad (40)$$

With G_{PI} representing the PI controller, G_C the capacitor filter dynamics (41) and G_{eq} represents the current controller. The current controller can be shown to suit a first order transfer function estimated by (42). Using modulus optimum with pole cancellation by setting $T_{iv} = T_{eq}$ would lead to two poles at origin and hence an unstable system [17]. Therefore, symmetrical optimum was implemented for PI controller tuning.

$$T_C = \frac{C_{f,pu}}{\omega_B} \quad (41)$$

$$T_{eq} = 2 * T_a \quad (42)$$

The PI controller parameters are estimated by (43) and (44) to achieve a satisfactory response and phase margin. For the BESS voltage controller, $a = 3$ was chosen, which gives real and equal roots [17].

$$T_i = a^2 * T_{eq} \quad (43)$$

$$K_p = \frac{T_c}{a * T_{eq}} \quad (44)$$

Inserted with parameter values the gain and time constant of the PI-controller yields:

$$T_i = 0.0027 \text{ s} \quad (45)$$

$$K_p = 9.36 \quad (46)$$

A step response of the closed loop transfer function is shown in Figure F. 7. This shows that the regulated signal has a 25 % overshoot and settles below 2 % after 7.5 ms. Figure F. 8 shows the Nichols plot with stability margins $\Delta K = \infty$ and $\psi = 53.1^\circ$.

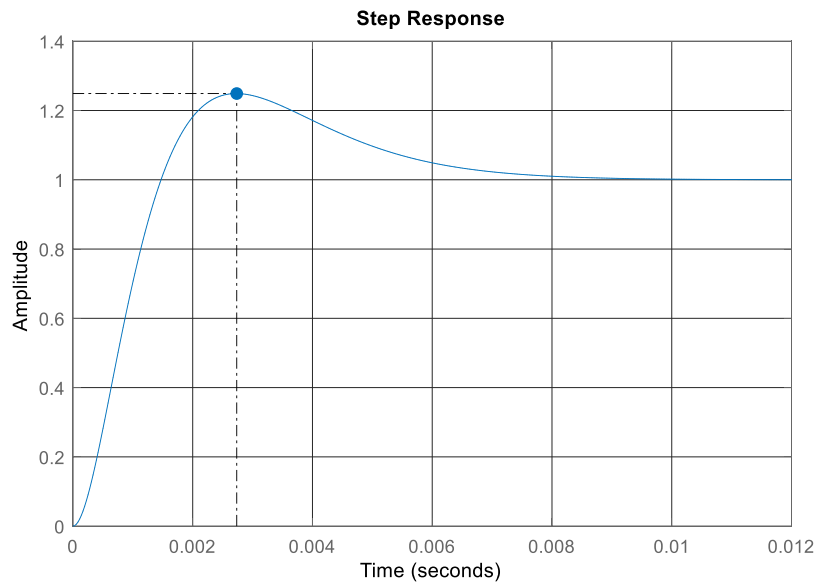


Figure F. 7. Step Response BESS Voltage Controller

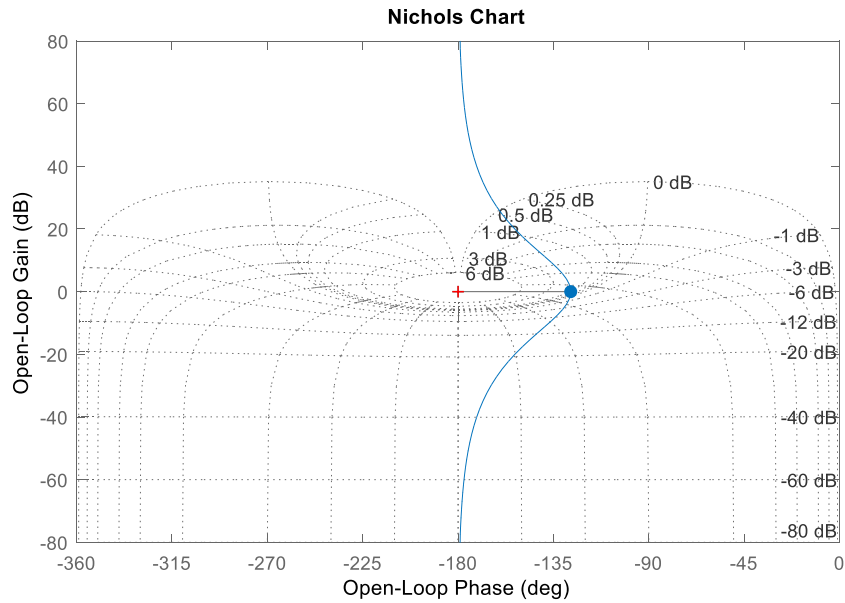


Figure F. 8. Nichols Chart BESS Voltage Controller

F.5 DGR Speed Governor

The diesel generator systems open loop transfer function is given in (47). Here, the time delay associated with the combustion engine is neglected for linearization. However, it could have been included by performing a first- or second order Padé approximation.

$$G_{OL}(s) = G_{PI}(s) * G_{Act}(s) * G_H(s) = K_p \cdot \frac{1 + T_i s}{T_i s} \cdot \frac{1}{1 + T_{act} s} \cdot \frac{1}{2H_{DGR} s} \quad (47)$$

For the diesel speed controller, a practical approach is used for tuning of the response by considering the response to a change in reference speed. The resulting PI-controller settings are tuned to:

$$T_i = 0.55 \quad (48)$$

$$K_p = 14.55 \quad (49)$$

A step response of the closed loop transfer function is shown in Figure F. 9. This shows that the regulated signal has a 28 % overshoot and settles below 2 % after 0.93 s. Figure F. 10 shows the Nichols plot with stability margins $\Delta K = \infty$ and $\psi = 87.6^\circ$.

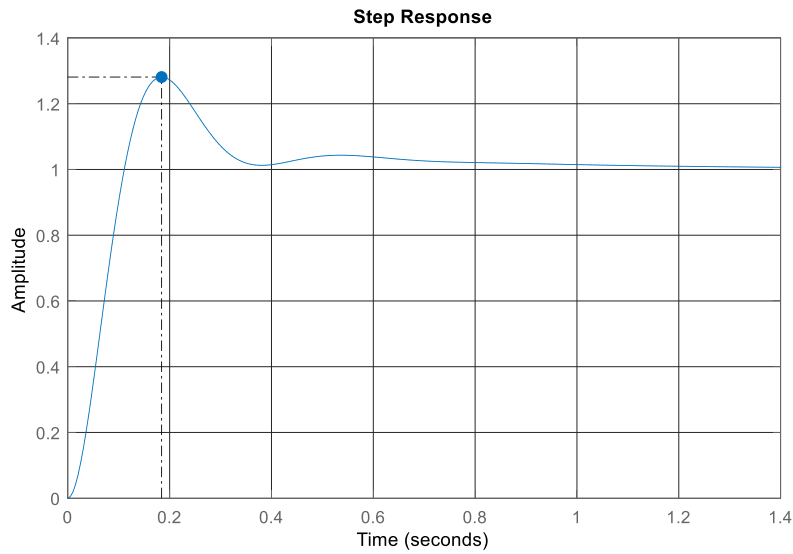


Figure F. 9. Step Response DGR Speed Controller

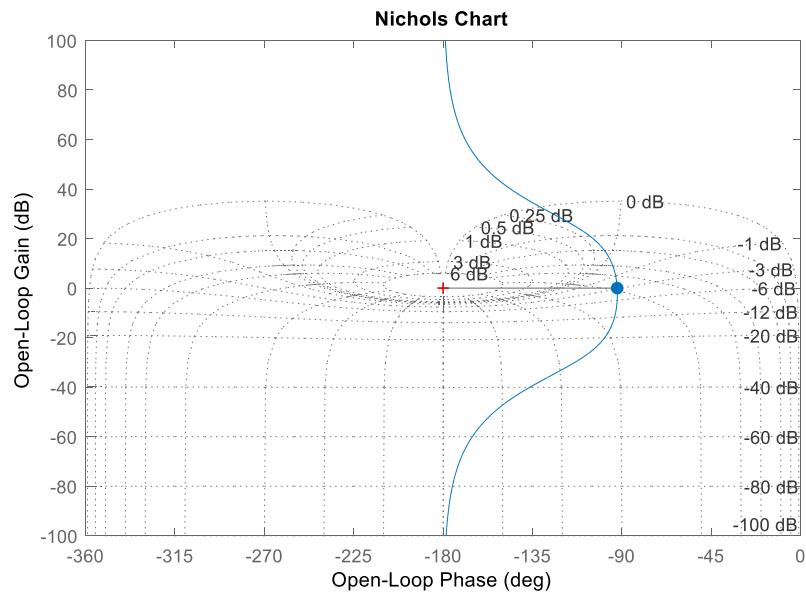


Figure F. 10. Nichols Chart DGR Speed Controller

F.6 WT SSC Current Controller

Like the PV current controller, the WT SSC current controller open loop transfer function can be described by:

$$G_{OL}(s) = G_{PI}(s)G_{PWM}(s)G_{RL}(s) = K_{p,pu} \cdot \frac{1 + T_i s}{T_i s} \cdot \frac{1}{1 + T_a s} \cdot \frac{1}{R_{pu}(1 + T_{pu} s)} \quad (50)$$

For further information on the parameters and estimation, see tuning of PV Current Controller. PI controller parameters are given by (51) and (52).

$$T_i = T_{pu} = 0.0588 \text{ s} \quad (51)$$

$$K_p = \frac{T_{pu} * R_{pu}}{2 * T_a} = 9.67 \quad (52)$$

A step response of the closed loop transfer function is shown in Figure F. 11. This shows that the regulated signal has a 16 % overshoot and settles below 2 % after 1.23 ms. Figure F. 12 shows the Nichols plot with stability margins $\Delta K = \infty$ and $\psi = 51.8^\circ$.

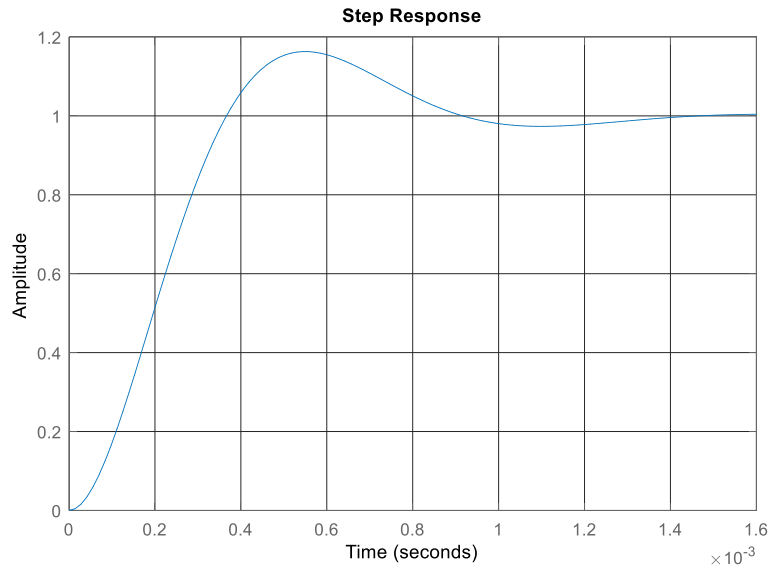


Figure F. 11. Step Response WT SSC Current Controller

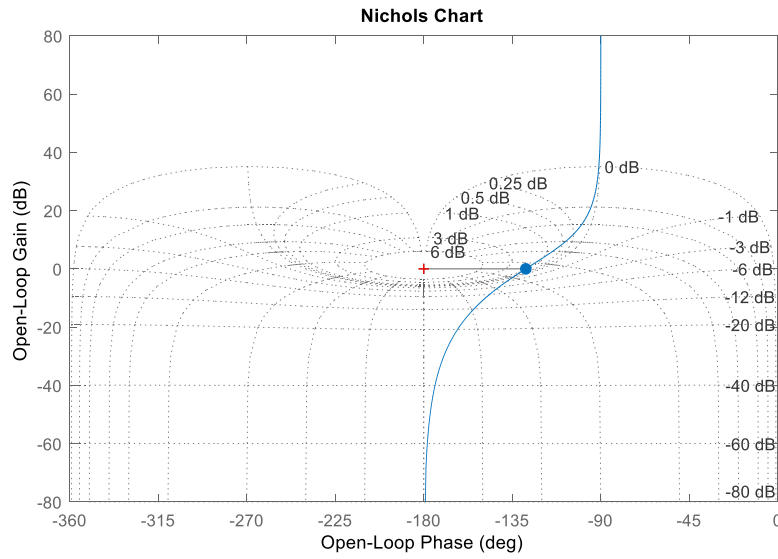


Figure F. 12. Nichols Chart WT SSC Current Controller

F.7 WT SSC DC-Voltage Controller

Similar as for the PV DC-voltage controller with the open loop transfer function including the PI-regulator, first order transfer function estimation of the current controller, and the DC capacitor dynamics:

$$G_{OL}(s) = G_{PI}(s)G_{eq}(s)G_{DC}(s) = K_{p,pu} \cdot \frac{1 + T_i s}{T_i s} \cdot \frac{1}{1 + T_{eq} s} \cdot \frac{v_{d,pu}}{V_{DC,pu}} \cdot \frac{1}{T_c s} \quad (53)$$

Like the PV DC-controller, the $a = 3$ was chosen. See sections on PV DC-controller or Symmetrical Optimum for further information. Inserted with parameter values the gain and time constant of the PI-controller yields:

$$T_i = 0.0027 \text{ s} \quad (54)$$

$$K_p = 2.56 \quad (55)$$

A step response of the closed loop transfer function is shown in Figure F. 13. This shows that the regulated signal has a 25 % overshoot and settles below 2 % after 7.5 ms. Figure F. 14 shows the Nichols plot with stability margins $\Delta K = \infty$ and $\psi = 53.1^\circ$.

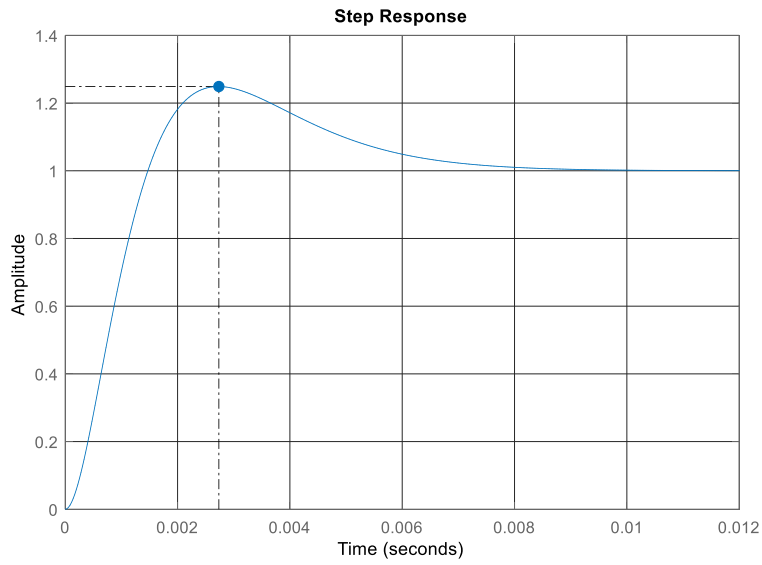


Figure F. 13. Step Response WT SSC DC-Voltage Controller

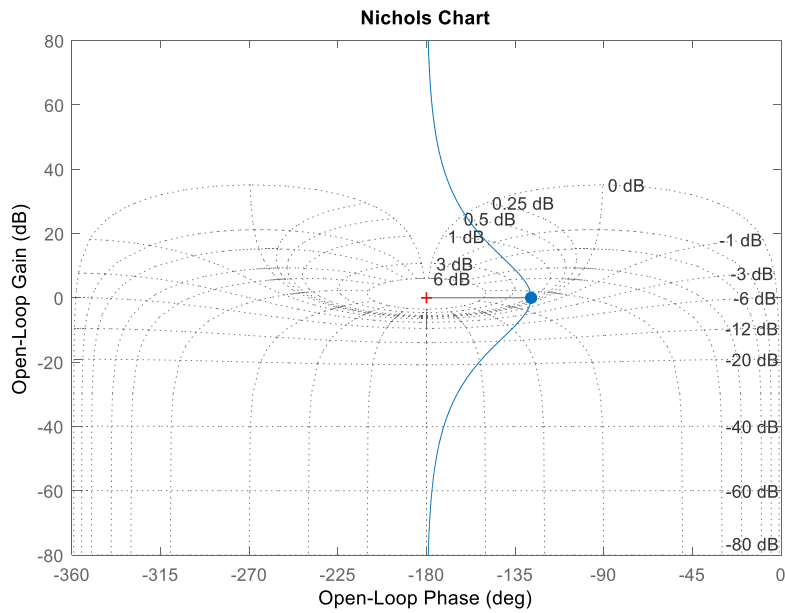


Figure F. 14. Nichols Chart WT SSC DC-Voltage Controller

F.8 WT SSC Reactive Power Controller

The open loop transfer function for the WT SCC reactive power controller is similar to the DC-voltage controller but includes the RL-filter dynamics instead of the DC-capacitance dynamics. Open loop transfer function can be given by:

$$G_{OL}(s) = G_{PI}(s)G_{eq}(s)G_{RL}(s) = K_{p,pu} \cdot \frac{1 + T_i s}{T_i s} \cdot \frac{1}{1 + T_{eq} s} \cdot \frac{1}{R_{pu}(1 + T_{pu} s)} \quad (56)$$

To ensure a sufficient phase margin for the outer loop is tuned according to the symmetrical optimum criteria given by (57) and (58), with $a = 3$.

$$T_v = a^2 * T_{eq} \quad (57)$$

$$K_p = \frac{T_{pu} * R_{f,pu}}{a * T_{eq}} \quad (58)$$

Inserted with parameter values the gain and time constant of the PI-controller yields:

$$T_i = 0.0011 \text{ s} \quad (59)$$

$$K_p = 3.1 \quad (60)$$

A step response of the closed loop transfer function is shown in Figure F. 15. This shows that the regulated signal has a 24 % overshoot and settles below 2 % after 7.5 ms. Figure F. 16 shows the Nichols plot with stability margins $\Delta K = \infty$ and $\psi = 53.4^\circ$.

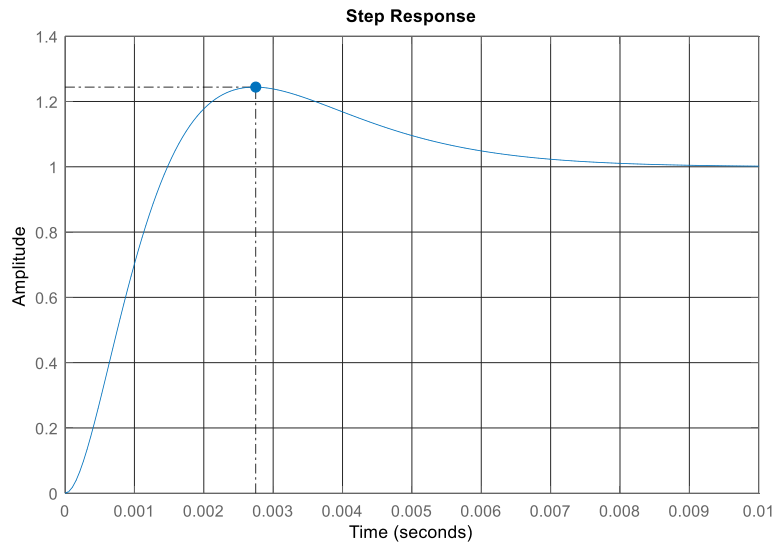


Figure F. 15. Step Response WT SSC Reactive Power Controller

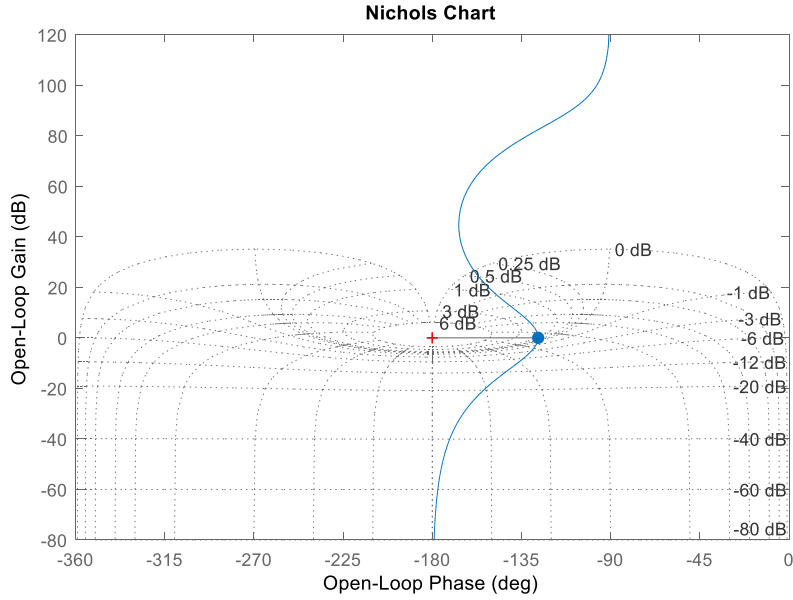


Figure F. 16. Nichols Chart WT SSC Reactive Power Controller

F.9 WT MSC Current Controller

The open loop transfer function for the inner current controller of the MSC includes a PI-controller, the VSC and induction machine dynamics [31], which yields:

$$G_{OL}(s) = G_{PI}(s)G_{PWM}(s)G_{DYN}(s) = K_p \cdot \frac{1 + T_i s}{T_i s} \cdot \frac{1}{1 + T_a s} \cdot \frac{1/R_s}{(1 + \sigma T_s s)} \quad (61)$$

Where σ is the machines total leakage factor and σ_s is the stator leakage factor [31]. T_s is given by (62), while T_a is given by (63).

$$T_s = \frac{(1 + \sigma_s)}{R_s} L_m \quad (62)$$

$$T_a = \frac{1.5}{2 * f_{sw}} \quad (63)$$

With the modulus optimum tuning criteria, the PI-parameters can be found as:

$$T_{pu} = \sigma * T_s \quad (64)$$

$$K_p = \frac{T_{pu} * R_s}{T_a} \quad (65)$$

$$T_i = T_{pu} \quad (66)$$

Inserted with parameter values the proportional gain and time constant of the PI-controller yields:

$$T_i = 0.0278s \quad (67)$$

$$K_p = 18.2 \quad (68)$$

A step response of the closed loop transfer function is shown in Figure F. 17. This shows that the regulated signal has a 16 % overshoot and settles below 2 % after 1.2 ms. Figure F. 18 shows the Nichols plot with stability margins $\Delta K = \infty$ and $\psi = 51.8^\circ$.

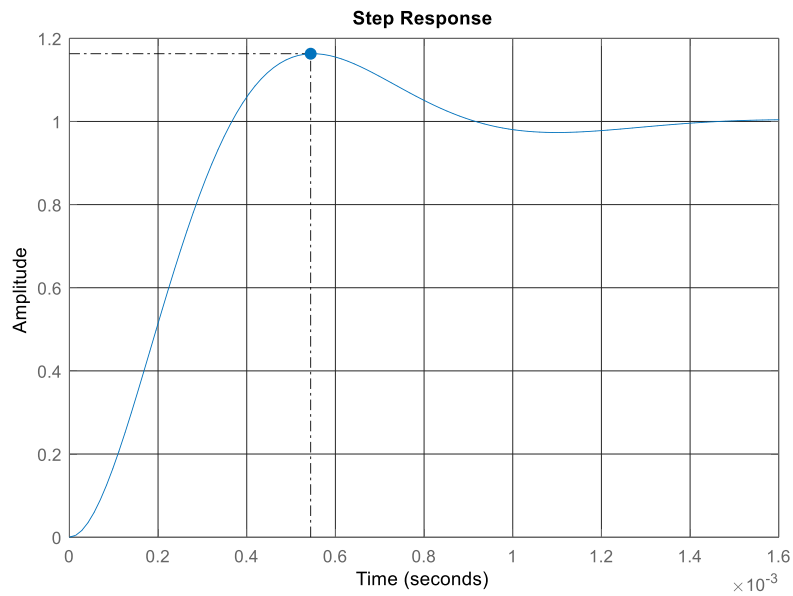


Figure F. 17. Step Response WT MSC Current Controller

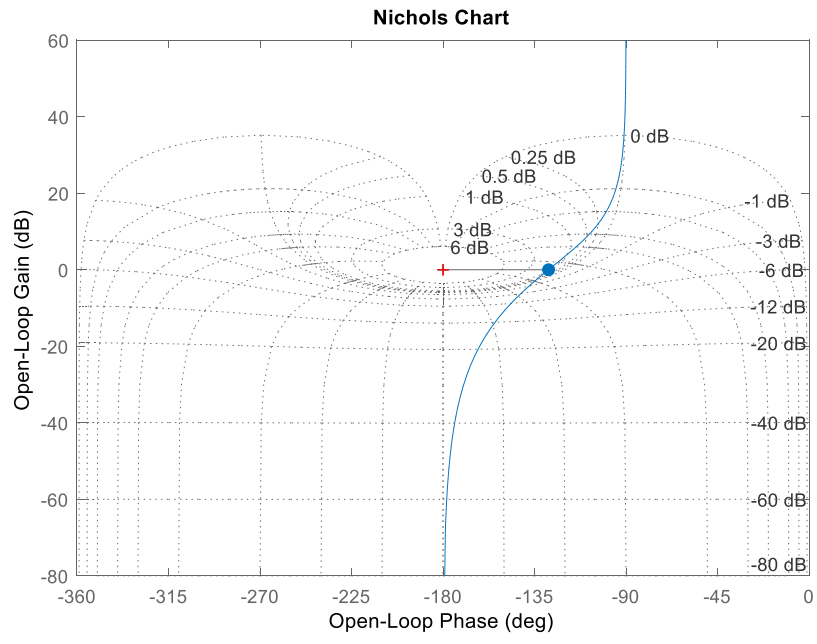
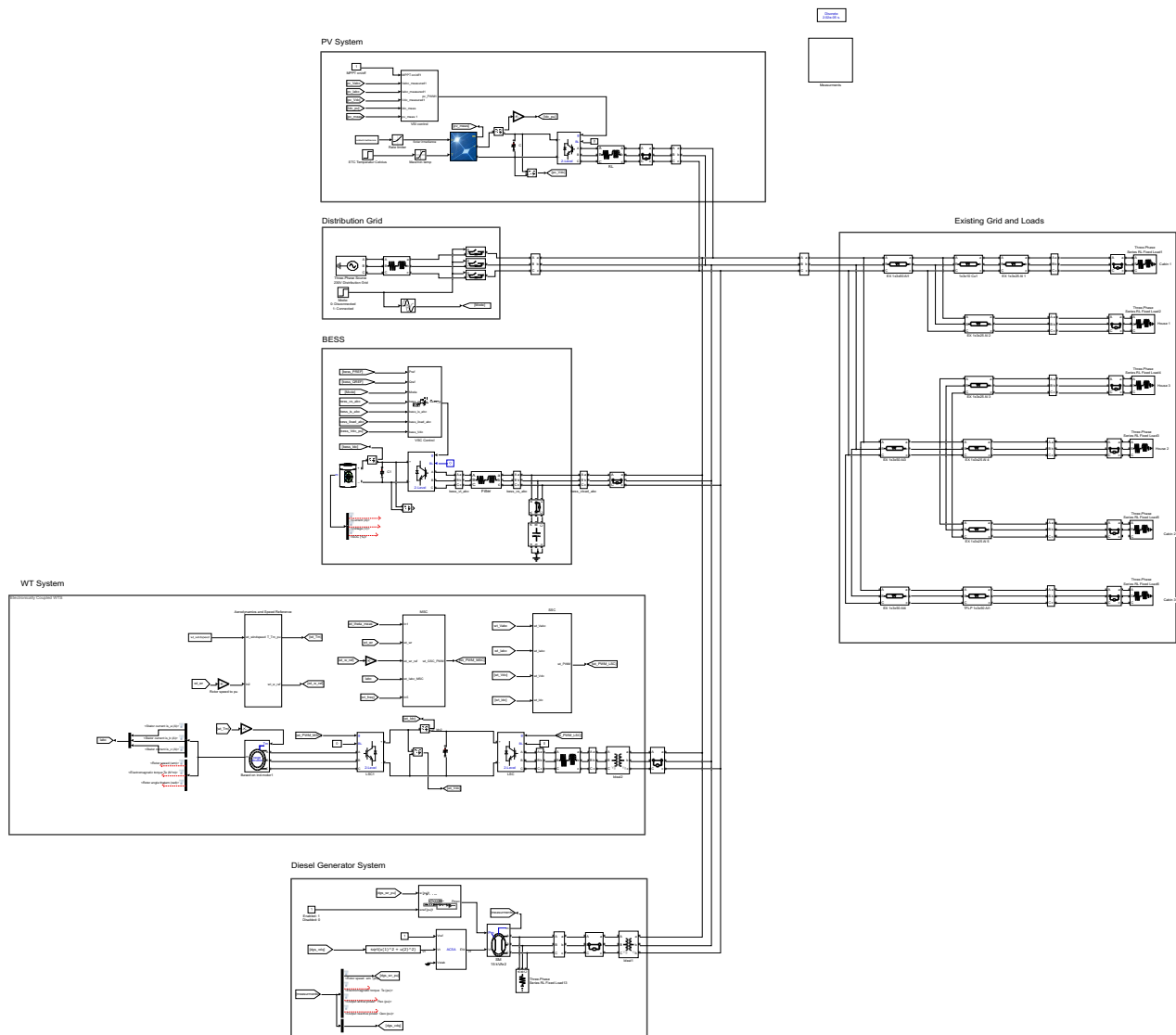


Figure F. 18. Nichols Chart WT MSC Current Controller

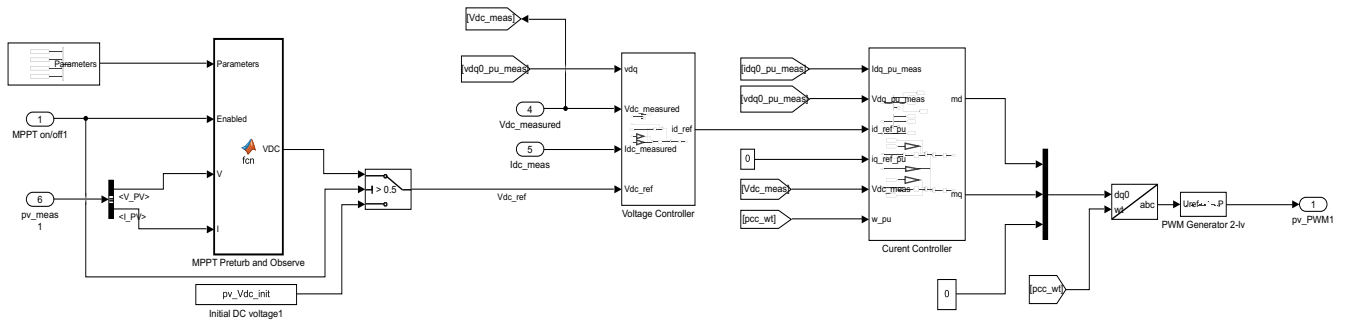
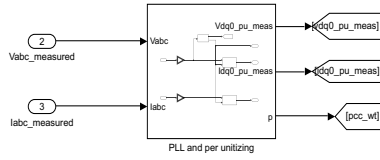
G. Simulink Model

G.1 Overall Microgrid

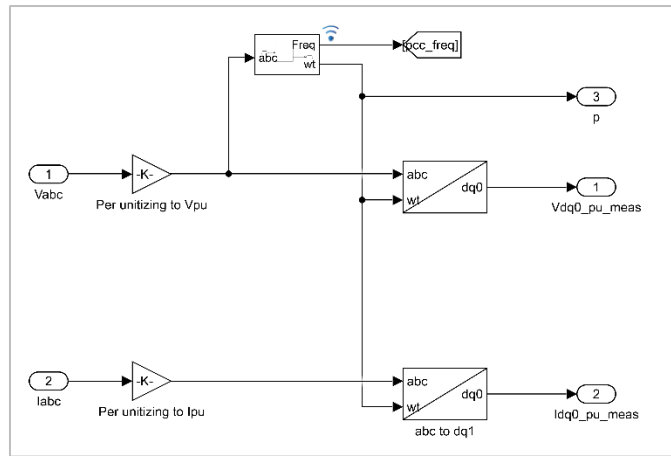


Overview of Microgrid

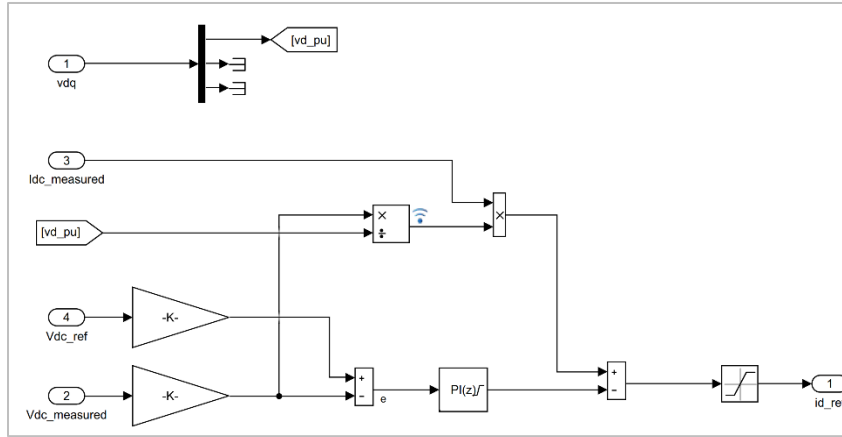
G.2 PV System



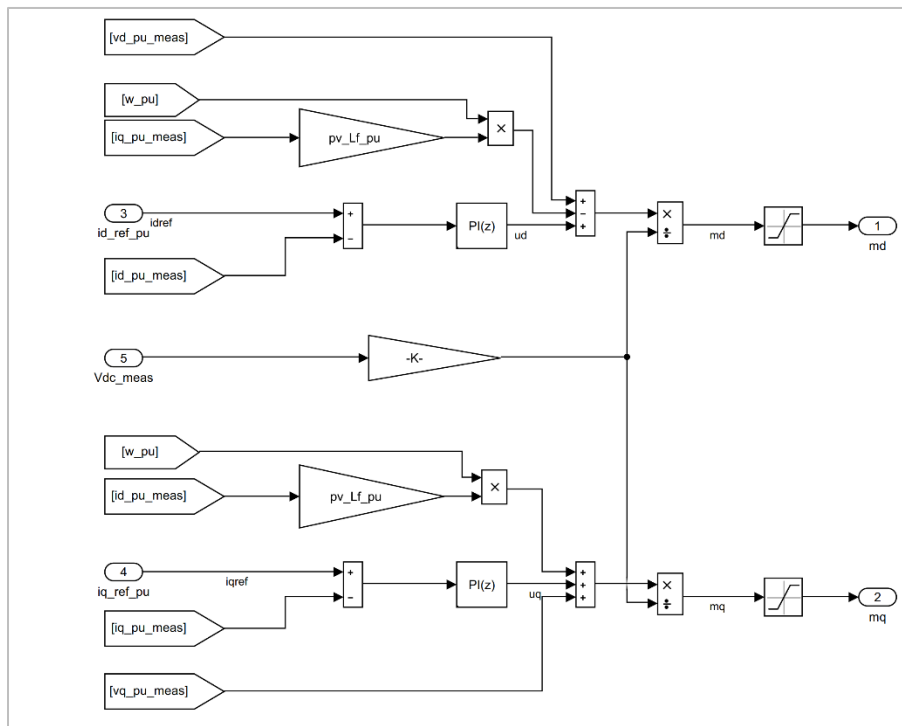
Overall View



PLL and Park Transformation

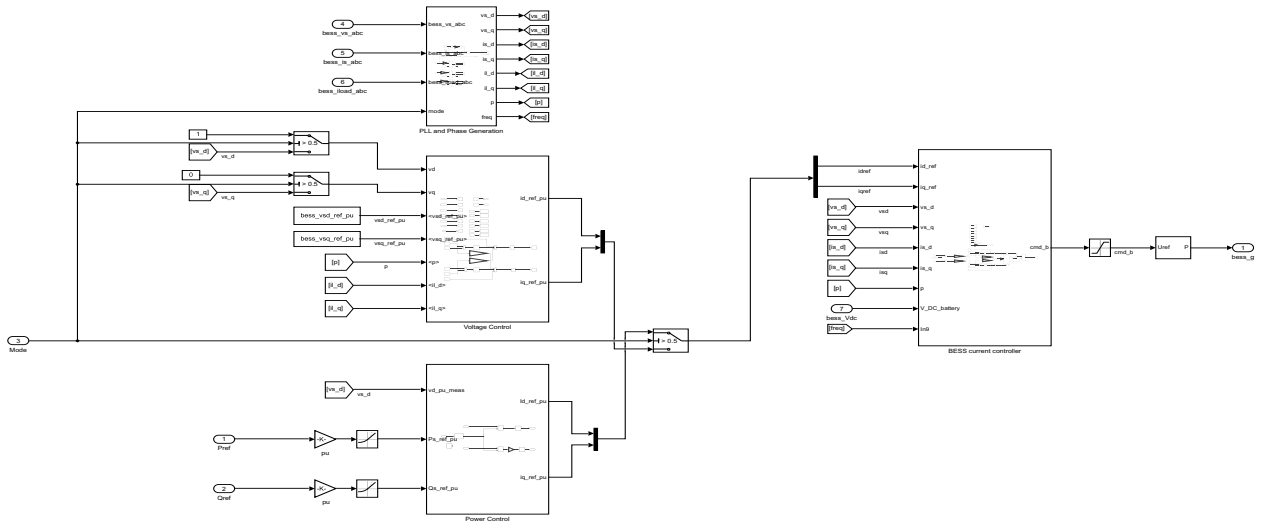


PV DC-Voltage Controller

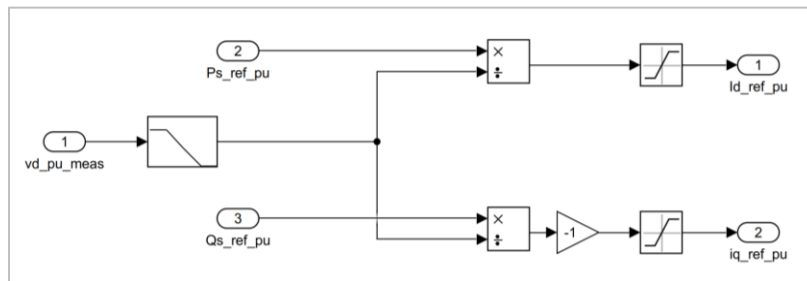


PV Current Controller

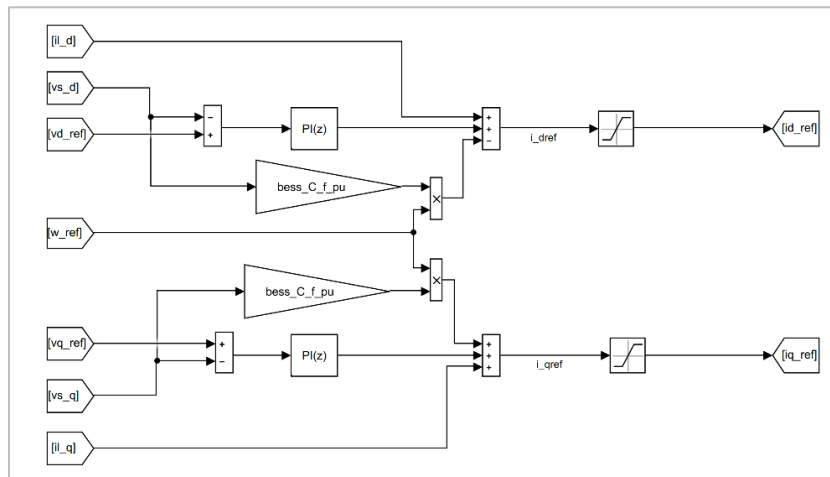
G.3 BESS



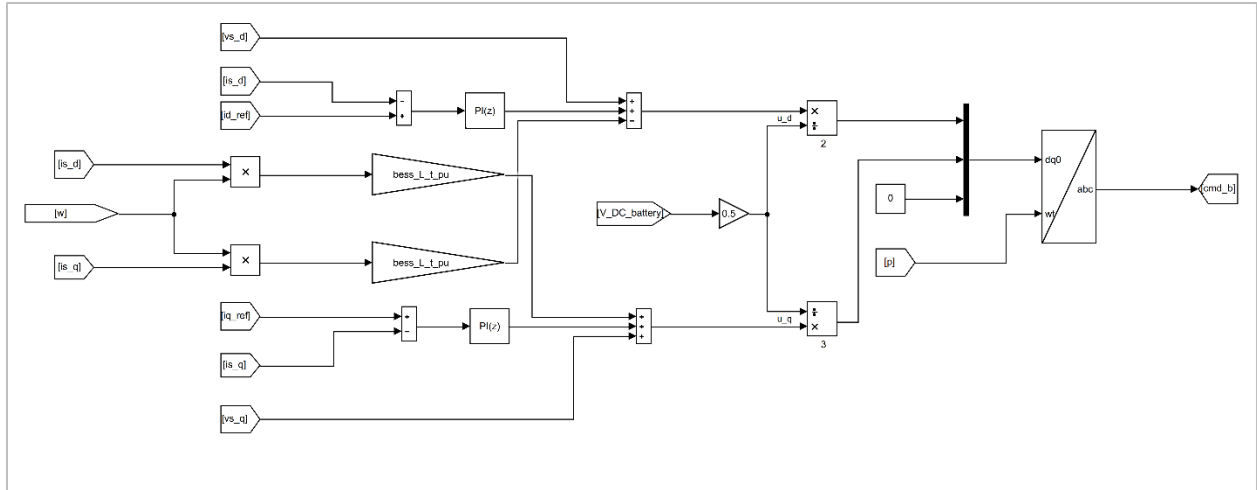
Overall View



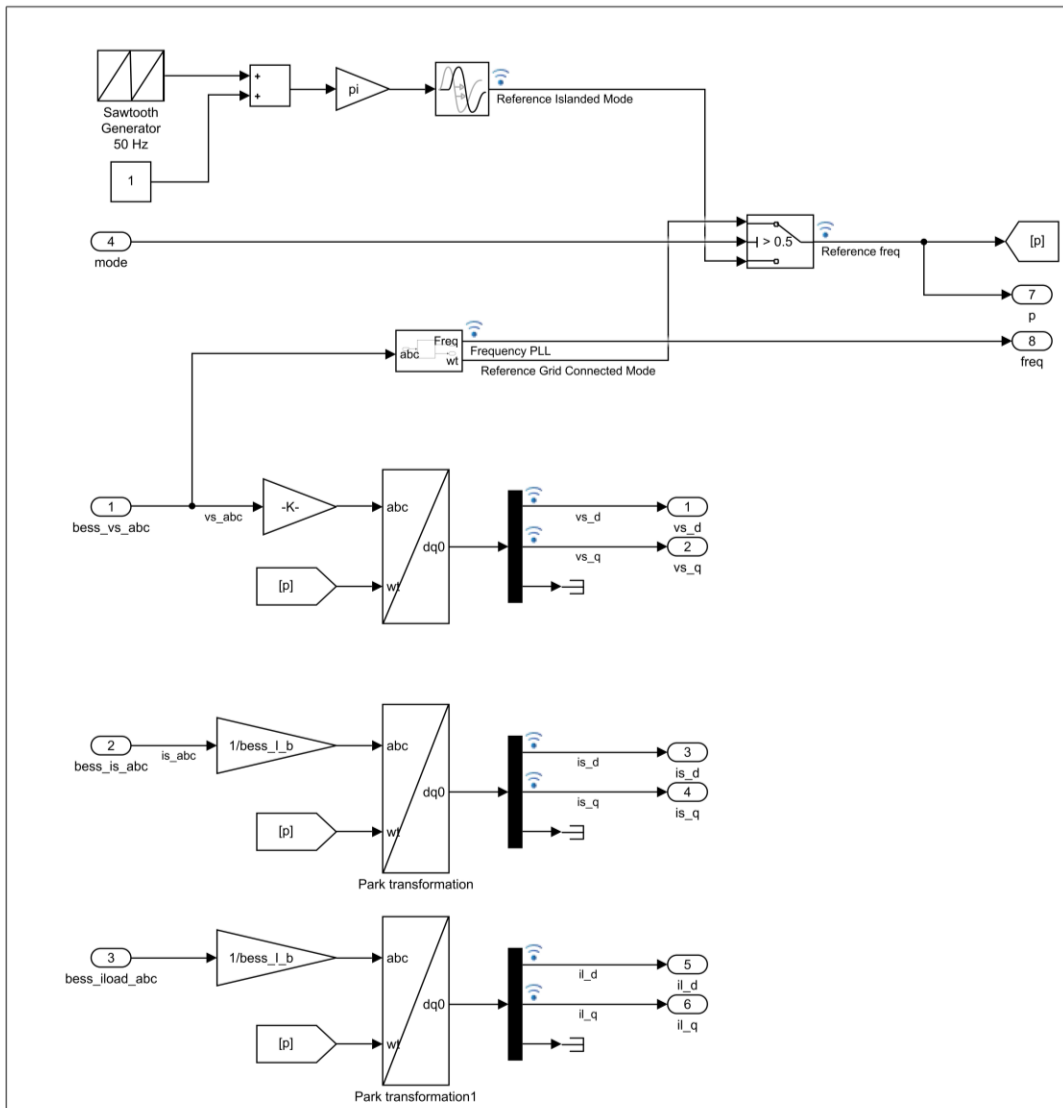
BESS Power Controller



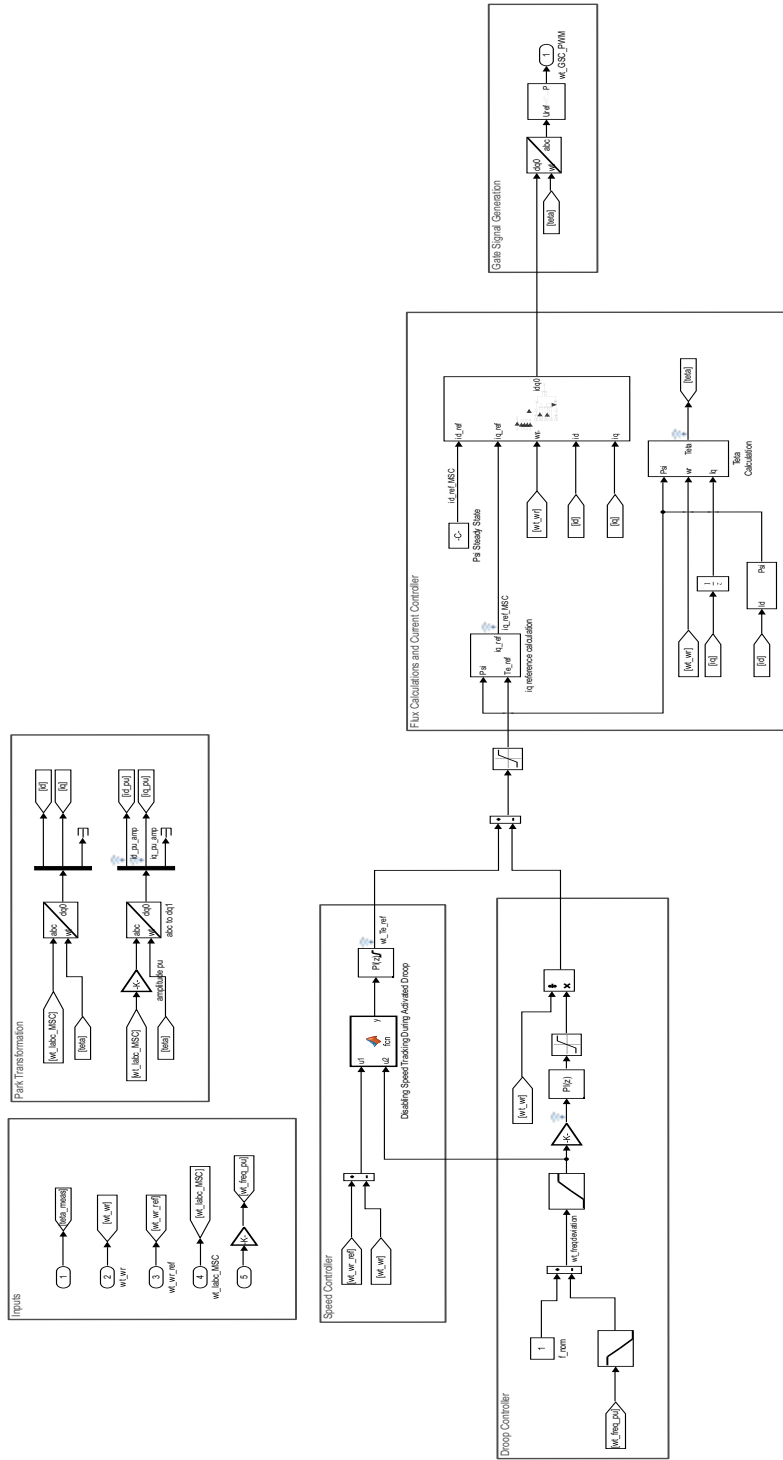
BESS Voltage Controller



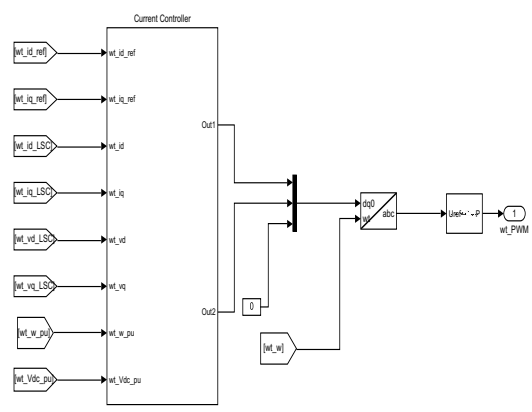
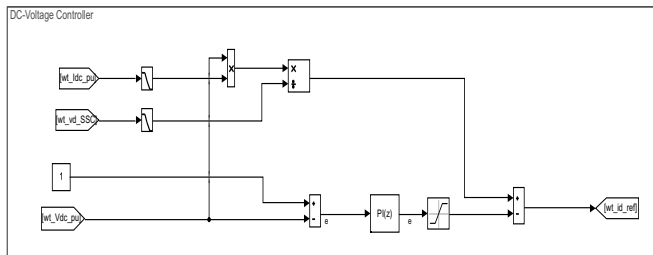
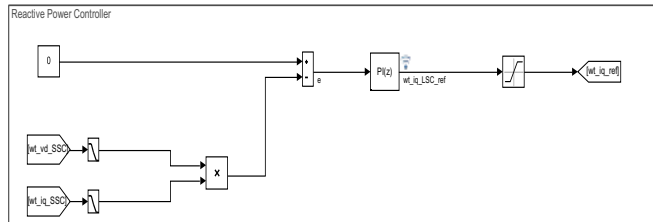
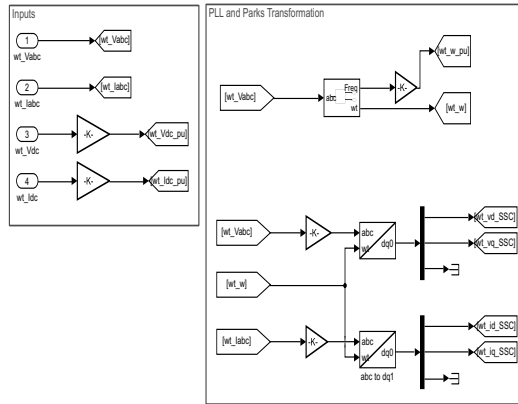
BESS Current Controller



BESS Reference Signal Generator for Park Transformation and Island Mode Switch

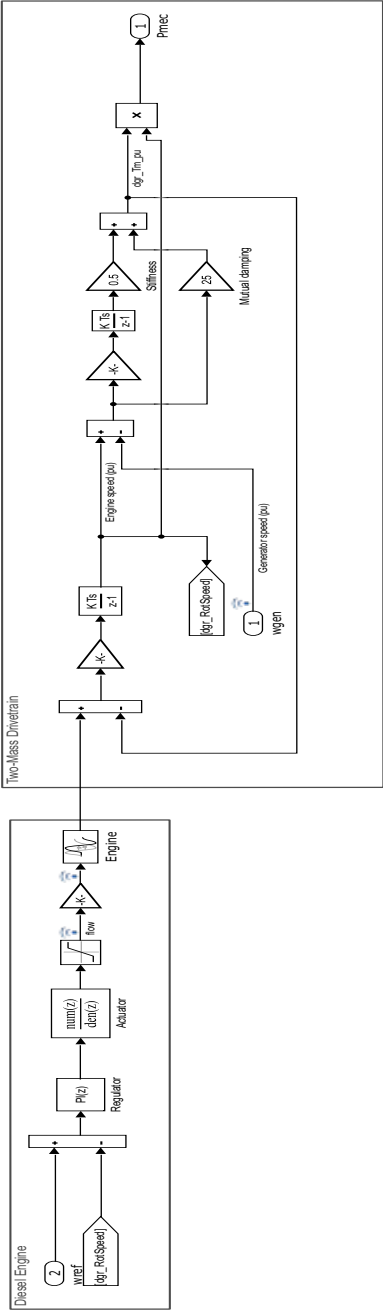


WT MSC



WT SSC

G.5 Diesel Generator System



Engine and Drivetrain Model

